EUROPEAN COMMISSION
6th EURATOM FRAMEWORK PROGRAMME

Final Interpretation Report of the PHEBUS test FPT0 (Bundle Aspects)

K. Mueller[1)], B. Toth[1)], M.S. Veshunov[2)], K. Trambauer[3)], C. Jamond[4)], R. Dubourg[4)], H. Manenc[4)], N. Girault[4)], M. Kissane[4)], G. Repetto[4)], W. Plumecocq[4)], P. Taylor[4)], T. Haste[5)], J. Birchley[5)], D. Bottomley[6)], G. Schanz[7)], J. Stuckert[7)] F. Lemoine[8)], N. Davidovich[9)], P. Mason[10)]

JRC/IE	Joint Research Centre, Institute for Energy, Petten, The Netherlands
IBRAE	Russian Academy of Sciences, Nuclear Safety Institute, Moscow, Russia
GRS	Gesellschaft für Reaktorsicherheit, Munich, Germany
IRSN	Institut de Radioprotection et de Sûreté Nucléaire, Cadarache, France
PSI	Paul Scherrer Institut, Villingen, Switzerland
JRC/ITU	Joint Research Centre, Institute for Transuranium Elements, Karlsruhe, Germany
FZK	Forschungszentrum Karlsruhe, Karlsruhe, Germany
CEA	Commissariat à l'Energie Atomique/DTP, Cadarache, France
ENEA	Ente per le Nuove Technologie, l'Energia e l'Ambiente, Bologna, Italy

DG JRC

Institute for Energy

October 2007

EUR 23222 EN

Mission of the Institute for Energy

The Institute for Energy provides scientific and technical support for the conception, development, implementation and monitoring of the community policies related to energy.

European Commission
Directorate-General Joint Research Centre
Institute for Energy

Contact information
Address: L. Ammirabile
E-mail: luca.ammirabile@ec.europa.eu
Tel.: +31 (0) 224 56 5064
http://ie.jrc.www.jrc.nl/
http://www.jrc.cec.eu.int/

EUR 23222 EN

ISSN 1018-5593

Luxembourg: Office for Official Publications of the European Communities

Printed in Netherlands, DG JRC, Institute for Energy, PR & Communication

Contents

Figures

Tables

1 Introduction

The objective of the bundle part of the Phebus test FPT0 was, according to the final test protocol calculated by Mailliat and Jones [1], to maximise the fission product release and the fuel rod degradation. The fission product release was to take place in an oxidising gas at low pressure and the large degradation was to be achieved by fuel melting.

Before the publication of the test results, one assumed that core degradation processes had already been studied sufficiently in other test facilities so that understanding how well computer codes were able to predict the core degradation was only a secondary objective of the test. Consequently, one thought that the study of the degradation phenomena was not an end in itself but a means to obtain the required fission product release [2]. The results of the code calculations summarised in the intermediate report [2] clearly showed, that these statement were too optimistic. Therefore, in the last years the work on code and model development continued at the national levels – especially in France and Germany - as well as in the frame of European projects. These efforts should be going on and be concentrating to specific problems. Therefore, the objective of this report is not only to achieve a profound interpretation of the experimental data of the FPT0 test, but also to show the most uncertainties in the code prediction as well as in the modelling, respectively. To reach this objective, both the present knowledge and the latest calculation results obtained with mechanistic codes were taken into account.

Therefore, in this final interpretation report specific tests results of the intermediate interpretation report [2] are re-discussed taken into account the progress made in the interpretation as well as in the modelling. Furthermore, new results concerning the bundle degradation and fission product release are presented. These calculations were performed by GRS and IRSN using the mechanistic codes ICARE2 ([3], [4]) and ATHLET-CD [5]. IRSN performed also stand-alone calculations using ELSA [6] MFPR [7] to examine the fission product release. At JRC a new dissolution/oxidation model ([8] to [13]) was developed and applied to the Phebus tests FPT0 [2] and FPT1 [14] to study melt formation during the degradation phase.

Shortly after carrying out the FPT0 test, the main experimental results were briefly summarised by Hanniet et al. [15]. The detailed description of measurements as well as their interpretation was published later in the FPT0 Final Report written by Hanniet and Repetto [16]. Consequently, the interpretation of the test results given in [16] is summarized in this paper. It should be noted, that there also exist various summaries in the open literature ([17], [18]). Specific results presented at the Bundle Interpretation Circles ([19] through [42]) are re-discussed. In this circle, the computational analyses are coordinated; they are performed by the partners from organisations that support the Phebus-FP project. These meetings provided a forum for code analysts to discuss the results of their calculations, which are summarized in the minutes and proceedings, respectively.

Overview of the Test Scenario

The main components (test assembly, circuit and containment) of the PHEBUS test facility are shown in Figure 1. The test assembly is inserted in the centre of the 40 MW driver core covered by water in an open pool. It refers to 6 m long cylindrical device with an outer diameter between 0.121 m and 0.25 m loaded in the experimental cell. The lower part contains test fuel and the instrumentation and the upper part services lines, instrument lead-outs as well as shielding.

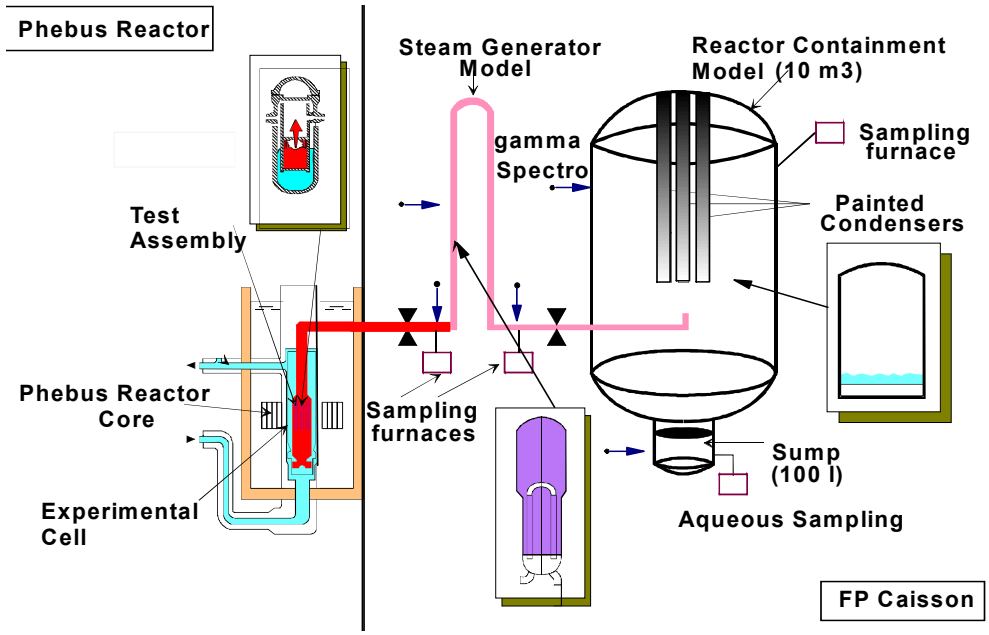

Figure 1: Phebus Test Facility

The bundle itself consists of twenty fuel rods in a 0.0126 m pitch matrix with an active length of 1.0 m and a total 4.5 % enriched UO2 mass of about 10.5 kg. For the fuel cladding, the stiffeners and for the two spacer grids Zircaloy-4 was used. In the FPT0 test the fuel was in situ irradiated for 9 days to a burn-up of 0.23 GWd/tU, i.e. only trace-irradiated fresh fuel was used. An Ag-In-Cd absorber rod surrounded by a Zircaloy guide tube was inserted in the centre of the bundle. The bundle is insulated by a multi-layered thoria and porous zirconia shroud. The outer shroud is surrounded by a pressure tube, which is cooled by an external water flow. Thermocouples are installed in the bundle and in the shroud region [18].

The stainless steel containment vessel has a volume of 10 m^3, which enables that the fission product concentrations be representative for reactor conditions are likely to be preserved. The heat transfer and condensation on the reactor containment surfaces are taken into account by the installation of three vertical condensers centrally located in the upper plenum of the containment. Each condenser is subdivided in a ~1.7 m long wet part and a ~0.8 m long dry part. The temperature of the upper wet part is controlled by an organic liquid loop. This enables that the injected steam condenses at those surfaces. The temperature of the dry part is regulated with electrical heaters. The condenser surfaces are covered with epoxy paint as a source of organic iodine. The outer containment walls are slightly overheated to prevent any steam condensation and to minimize the aerosol deposition. The wall temperatures are also controlled by an organic liquid loop. The lower containment vessel structure consists of an elliptical bottom and a 0.1 m^3 sump with a diameter of 0.58 m in order to produce a correctly scaled atmosphere water-surface. The sump water is circulated by an auxiliary loop and water can be injected to wash the settled aerosols into the sump.

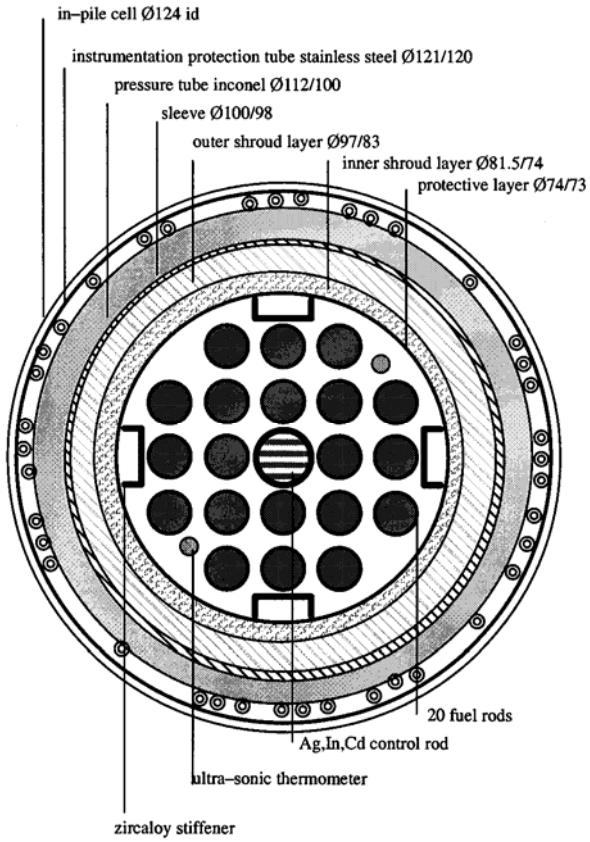

Figure 2: Cross Section of the FPT0 Bundle

According to the intermediate interpretation report [2], the bundle phase of test scenario is subdivided in the following phases:

Period, seconds	Phase
0 to10000	calibration phase
10000 to11000	control rod failure
11000 to12500	oxidation escalation
12000 to15500	collapsing phase or degradation phase
15500 to18000	molten pool phase until power shutdown
18000 to 18200	final event

The observed phenomena strongly depend on the bundle temperatures, which are controlled by the bundle power nearly during the whole transient. Therefore, the power history reflects these phases except during the oxidation escalation.

In reference [18], except the calibration phase, the whole test scenario between 10000 s and 18000 s is characterized as *degradation phase*. In some analyses, the period from the start of the oxidation escalation at 11000 s until 14000 s is regarded as oxidation *phase* because during this period a relatively small fraction of total mass relocates downwards. The last and most powerful heat-up phase starts at 14000 s and leads to massive melting and materials relocation at shutdown time, therefore this period is frequently referred as the *degradation phase*.

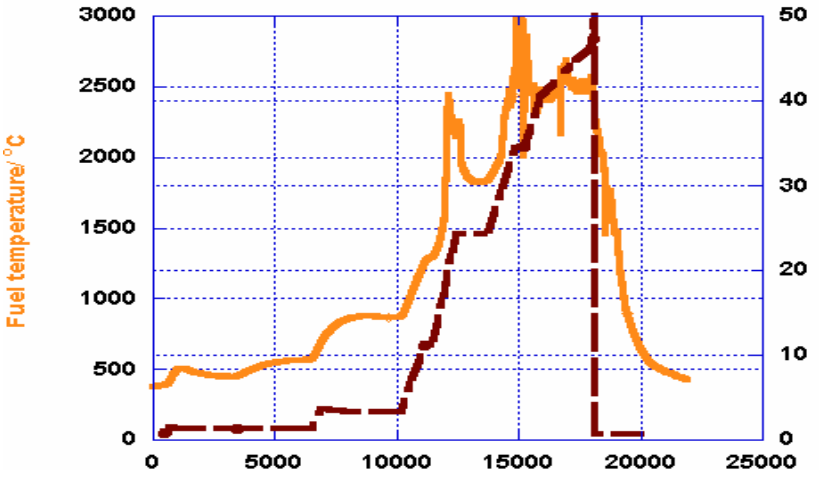

Figure 3: Nominal bundle power and the thermal bundle behaviour illustrated by the temperature measured at bundle elevation of 0.7 m.

In the present work, we keep the characterization given in reference [2], however, for the collapsing phase, mainly the expression “degradation phase” is used and the oxidation escalation is regarded as “oxidation phase”, because around 90% of the total hydrogen mass is produced in this period. According to this subdivision (see above), one can recognize that the there exist an overlapping between the oxidation phase and the degradation phase, because the first fuel movement occurred already during the temperature escalation in the bundle.

2 Interpretation of the experimental Results

2.1 Calibration Phase

The aim of the calibration period was to test the proper functioning of the instrumentation as well as to check the heat losses. The latter are largely governed by the thermal conductivities of the porous zirconia layers of the shroud and by the thermal gap resistances between the layers. As reported in [2] in the several years following the test the code analysts discussed intensively on the shroud material properties and on the influence of the thermal expansion of the shroud. Meanwhile, material properties similar to the ones published in FFT0 data book [43] are used in the analyses and the shroud behaviour is adequately treated as demonstrated by the latest post-tests calculations (see Chapter 2.1).

2.2 Control Rod Failure

2.2.1 Experimental Findings

At 10800 s, the control rod temperature reached about 1400 K and a release of ^{116m}In was detected. Already after the melting of the Ag-In-Cd alloy at 1100 K, the internal gas pressure in the rod will increase due to evaporation mainly of cadmium (Cd). The induced mechanical stresses and the thermal stresses as well lead to an expansion of the control rod. Therefore local solid-solid contacts occur between the inner surface of the Zry guide tube and the outer surface of the stainless steel cladding of the absorber. Mainly the material interaction between the Fe and Zry in the temperature range of 1220 K to 1570 K leads to a local control failure or early rupture, respectively, and small amounts of absorber material are released.

During the oxidation phase (see next Chapter 1.3), i.e. shortly after the onset of the oxidation run-away at 12000 s, the stainless steel melting point of 1730 K is rapidly reached. During the melting, a larger contact area will be established and the diffusion of Fe-component in the melt increases as well. After complete melting of the stainless steel cladding Ag also can diffuse to the Zircaloy of the guide tube and could enhance the dissolution due to the Ag/Zry material interaction. In any case, the dissolution of the Zry-guide tube and of the protective ZrO_2-layer after stainless steel melting occurs very rapidly and the control rod material is completely relocated from the upper bundle part to a lower temporary re-solidification zone. This zone is probably at the lower grid at 0.25 m above the bottom of the fissile column. Then the control rod material relocates further to the bottom of the bundle where it was found by post-test gamma scan and by PIE. No Ag-In-Cd interaction products were found by PIE in the upper half of the bundle confirming the rapid meltdown.

The first release was not detected with the aerosol monitor OLAM because of the low (Cd, In) and very low (Ag, Cr, Fe, Ni, Zr) concentrations at 1400 K. These components were not nucleated to aerosols or the aerosols had only attained concentrations below detection limits [16].

2.2.2 Status of the Control Rod Models

In the ICARE2/ELSA model, it is assumed that, at early control rupture, cadmium exists in vapour form and it is instantaneously released but the amount is very small, because the access of the gas flow to the liquid surface is limited. Therefore, in the code, a very low surface to volume ratio is used, which reflects the geometry. This value was fitted to FPT1 data and checked on FPT0. The same values in the range of 0.003-0.005 are used for Ag applying the same evaporation correlations, which are used during the candling of the Ag-In-Cd melt. As soon as the melting temperature of stainless steel cladding is reached, the actual release factions of three melt components are calculated using pressure- and the temperature-dependent correlations. For the evaporation from free surfaces, the same correlations are used [44].

In ATHLET-CD (also in ICARE2), the empirical CORSOR correlations can be applied to determine the release rates. The failure of the guide tube in ATHLET-CD can be calculated by taking into account the solid-solid/solid-liquid material interactions between the Zircaloy and stainless steel by means of empirical correlations ([45], [46]). As an alternative a temperature criteria can be used. As outlined in [39] the evaporation of the three control rod components based on the analogy between the heat and mass transfer taking into account their local saturation pressures. The resistance with respect to the mass transfer through the Ag-In-Cd melt to the liquid/vapour interface is neglected, i.e. it is assumed that the melt is being stirred due to the axial temperature gradient resulting in a significantly higher mass transfer rate to the surface compared the evaporation rate at the free surface. The evaporation rate is limited due to the mass transfer of the species into the gas bulk (over-heated steam and/or hydrogen). The saturation pressures of species at the surface are calculated as a function of the temperature by using the phenomenological three-parameter Antoine-equations. This concerns only the evaporation of relocated material (free surfaces), i.e. the evaporation during the down-flow of the low viscous absorber melt was neglected, because the relocation time is in the range of a few seconds.

For the calculation of absorber rod materials release in MELCOR, the CORSOR correlation can be also selected; and for the temperature of early control rod failure, the eutectic temperature of a Zry/stainless steel mixture (1473 K) is assumed as a criterion. However, MELCOR versions available at that time did not incorporate the CORSOR correlations into any release model, although if one knew the release fractions it was possible to "force" the code to reproduce them by suitable adaptation of the CORSOR correlations. The most recent version, the MELCOR 1.8.6, contains a model for Ag release, but it has not been used to analyse FPT0 at that time.

In all commonly used severe accident codes, the build-up of the rod inner pressure or the partial pressure of the most volatile element Cd is not taken into account in the burst release. The chemical reactions with steam/hydrogen mixture are not considered despite the fact that especially the formation of indium oxides seems to be most important [47].

2.3 Oxidation Phase

2.3.1 Experimental Findings

The escalation of the steam-Zircaloy reaction started (with hydrogen production) in the upper part of the bundle and propagated downward as the bundle temperatures increased [16]. The satisfactory operation of the thermocouples allowed measuring the high temperatures up to 2760 K (level 0.7 m) with heat-up rates of about 5 to 9 K/s [16]. The stabilisation of the power at 24 kW after the escalation led to a stabilisation of the maximum fuel temperature at about 2300 K.

The total amount of hydrogen generated during this phase was based on the analysis of gas samples taken from an atmosphere tank. About 70 % of the maximum possible H_2 amount, coming from the total consumption of the Zircaloy inventory in the bundle, was generated after the escalation.

The increase in the total bundle power was triggered by autocatalytic Zircaloy oxidation near 12000 occurring at bundle elevations between 0.9 m and 0.4 m see symbol 1 in Figure 4. The oxidation front started from level 0.9 m and moved rapidly downward to level 0.6 m. Then, 400 s later, the front reached level 0.4 m (mark 3, see Figure 4). The rapid oxidation started at a fuel temperature of about 1823 K (1550°C). The first sequence of the oxidation phase lasted about 3 minutes with an average heating rate evaluated at 9 K/s (between 1970 K – 2760 K).

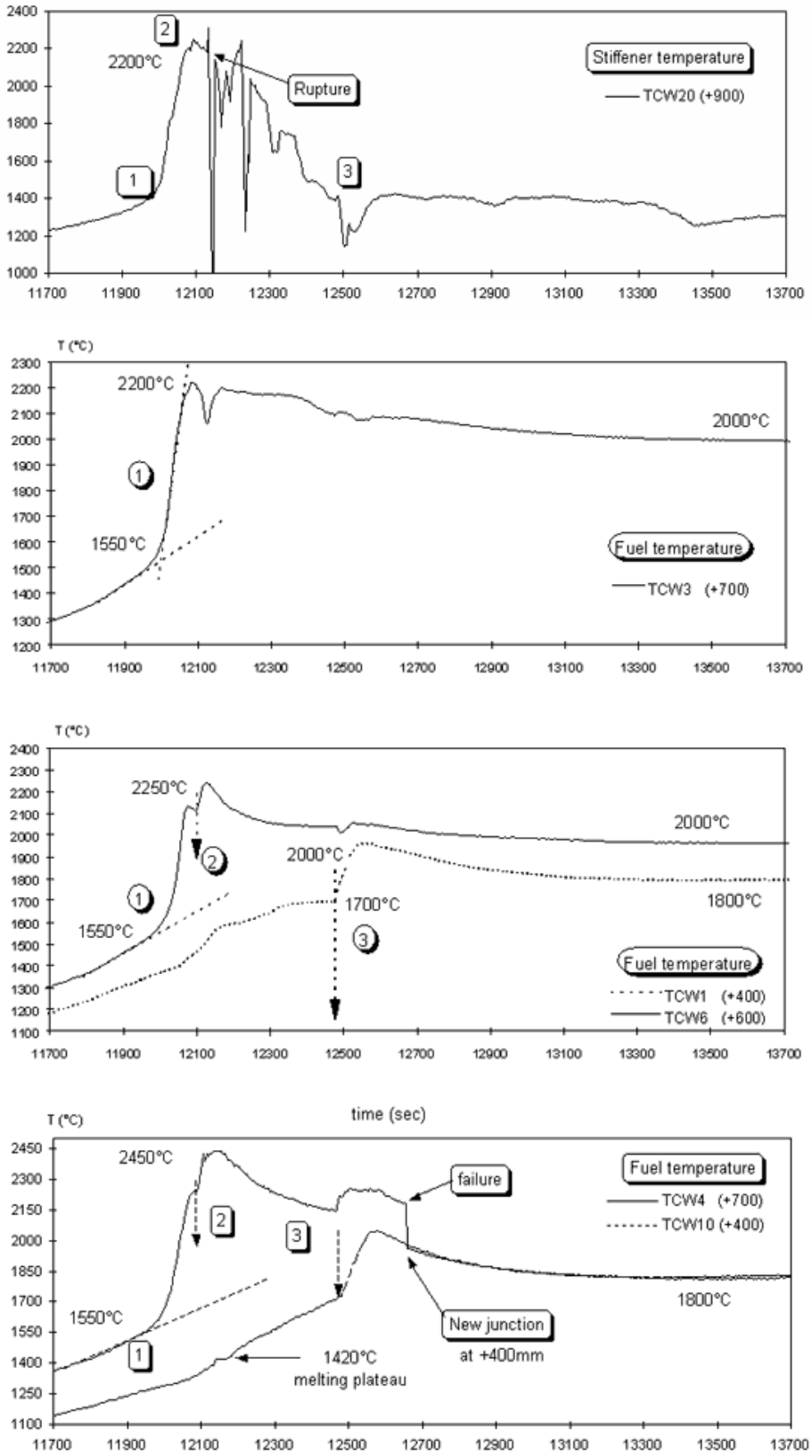

Figure 4: Temperature evolution at various bundle elevations during the oxidation phase in the test FPT0

2.3.2 Status of Oxidation Models and Clad Failure Criteria

The high temperature oxidation of solid Zircaloy in steam atmosphere is modelled in MELCOR and ICARE2 by assuming parabolic kinetics for oxide layer growth with parameters derived by Urbanic and Heidrick. These parameter values appear to the code users to be adequate as long as the Zircaloy is solid, though the users are aware of the conclusions of the COLOSS project [48] according to which below 1550°C the Cathcart and above 1550°C the Prater-Courtright correlations are recommended. In the ATHLET-CD code, this recommendation was adopted, i.e. the Cathcart – Prater – Courtright correlation was used and this resulted in the improvement of the code predictions for the timing of temperature escalation in comparison with the Urbanic-Heidrick correlation option. Likewise, the RELAP/SCDAP code combines two correlations to calculate the oxidation kinetics, namely the Cathcart correlation below 1580 at temperatures below or equal to 1580 °C and the Urbanic-Heidrick correlation above this value.

Some concerns arise on the oxidation rates in steam once the Zircaloy has become molten (see Section 3.4.4?). It is usually assumed in the codes that molten zirconium will be held in place between fuel pellet and the oxide shell until a temperature and/or a oxide thickness criterion is reached. Currently, the temperature criterion for oxide shell failure is a user-defined parameter. In MELCOR, the temperature criterion T_{clad} = 2400 K is recommended. In ICARE2 combined criteria are used such as T_{clad} = 2700 K, if oxide shell thickness $E_{ZrO2} > 250$ μm and $T_{clad} = 2600$K, if $E_{ZrO2} < 250$ μm. In ATHLET-CD – as T_{clad} = 2450 K, if oxide shell thickness $E_{ZrO2} > 300$ μm and $T_{clad} = 2250$K, if $E_{ZrO2} < 300$ μm.

SCDAP uses an approach similarly to MELCOR, except that the shell does not fail if more than some fraction cladding (default=0.6) is oxidised.

It can be seen that various defaults and recommendations for the temperature criterion have been used between 2300 and 2600 K and that the temperature criterion is generally well above the melting point (2250K) of the Zircaloy cladding. Consequently, there is then some time for hydrogen production by steam reaction with this molten zirconium. This hydrogen production proved important in the accurate prediction of the hydrogen production during the FPT0 test.

Once retention of the molten zirconium is no longer possible, a complex alloy of Zr-U-O will flow downward along on fuel rods and be susceptible to steam oxidation.

The main problem with the empirical temperature criterion applied to the temperature scenario presented in Figure 4 for high elevations above 0.6 m, is connected with very strong (or even complete) oxidation of the Zircaloy cladding before oxide shell rupture, that excludes melt relocation from these elevations during subsequent stages of the FPT0 test. However, this is in an apparent contradiction with the test observations (presented in the following Section 3.4), which gave a clear evidence to local molten pools formation at high elevations and melt downward relocation in later stages of the experiment.

This problem can be resolved by application of a more advanced mechanistic criterion for the clad rupture. Analyses of the available experimental data on the oxide scale failure at high temperatures obtained in FZK [48] and modelling of this phenomenon with the help of the SVECHA/QUENCH (S/Q) code developed in IBRAE [49] revealed the following two modes of oxide scale failure:

The outer oxide scale formed during the initial stage of an accident continues to grow after melting of Zircaloy metal phases. Owing to the volumetric expansion of oxide, the free volume unoccupied by the melt (gap volume between pellet and cladding) decreases and finally disappears, leading to the oxide scale failure induced by the pressure built-up in the

confined incompressible Zircaloy melt. This mechanism is characteristic mainly for the low heat up rate (<5 K/s) scenario.

The outer oxide scale is partially dissolved by molten Zircaloy and the hydrostatic pressure of non-confined molten Zircaloy destroys the thinned oxide layer. This mechanism is characteristic for the high heat up rate (>5 K/s) scenario.

SVECHA code simulations show that evolution of the oxide scale under interaction with molten Zircaloy depends on the oxide scale and metal phase thickness, oxygen content in molten Zircaloy and the oxygen flux at the cladding surface. The oxygen flux should strongly influence the oxidation kinetics: the decrease of the steam flow in the gas mixture can lead to the shift of the oxidation kinetics from "corrosion" (oxidation) to "erosion" (dissolution) and vice versa. Hence, timing of the oxide scale failure depends on erosion/corrosion kinetics and the mechanical strains in the oxide scale accumulated in the previous stages of an accident.

Despite the fact that the calculated failure mechanism is the result of the mutual interaction of oxidation/dissolution and deformation models implemented in SVECHA, as a first order approximation a simplified approach can be accepted. As revealed in the SVECHA analyses [49] the breaching of the oxide shell in the first case (volumetric expansion mechanism) occurs very soon after closure of the pellet-cladding gap, whereas breaching in the second case (dissolution mechanism) occurs when the oxide shell becomes very thin (in comparison with its initial thickness). This allows significant simplification of the failure criterion by the following assumptions: the outer oxide scale fails if either the free gap equals to zero (in the first case), or the oxide scale thickness equals to zero (in the second case). Therefore, only the simulation of the erosion/corrosion kinetics can be used to predict the oxide failure taking into account the interaction of the molten Zircaloy within the simplified approach of the system codes. It is important to emphasize that the predicted by SVECHA flowering temperature varies within ≈ 400 K depending on test conditions, this in agreement with FZK observations.

As shown in [11] using the presented above simplified high-temperature criteria for oxide shell failure (e.g., $T \geq 2600$ K), one should make a conclusion that the fuel rod geometry in the upper zone of the bundle will mostly remain intact after melting of the metal cladding. In this case, the S/Q code predicts (similarly to the other codes) rather quick (within 150 s) complete oxidation of the molten cladding and a moderate dissolution of UO_2 pellets (up to 8 %).

The application of the advanced criterion allows concluding that the oxide shell failure at high elevations has occurred already during temperature escalation just after the melting of metal α-Zr(O) at ≈12050 s, which leads to the formation of local molten pools above the upper space grid of the FPT0 bundle.

Furthermore, on the one hand, the local molten pool formation prevents metallic melt from complete oxidation owing to a high value of the volume–to–surface ratio in this melt configuration; on the other hand, it provides an enhanced fuel pellets dissolution by the melt (up to 40%, in correspondence with the test observations) during the subsequent degradation phase.

2.4 Core Degradation Phase

2.4.1 Experimental Findings

2.4.1.1 Temperature Evolution

The relocation of hot material from higher bundle positions to lower ones and the combined processes (oxidation, release of fission products and control rod material, blockage formation etc.) significantly influences the temperature evaluation within the bundle. Because the relocation processes occurred instantaneously, abrupt changes in the thermocouple readings were detected. The changes in the temperature behaviour at various bundle positions are defined as "events" indicating the occurrence of processes mentioned above. An overview of these events is reported in [2] and [16] and the most important ones are summarized below.

12500 seconds:
Temperature increase at bundle height of 0.4 m was detected

14350 seconds:
Increase of the shroud temperatures in the West zone at elevations of 0.3 m, 0.4 m, 0.5 m, 0.6 m and 0.7 m. Strong increase of the fuel temperature in the West zone between at 0.7 m and 0.8 m.

The crust located between 0.3 m and 0.7 m in the West zone – as determined from PIE post-test analysis - was probably formed during this period [16].

14730 seconds:
Increase of shroud temperatures in the Southeast zone at 0.3 m, 0.4 m and 0.5 m;
Strong increase of the fuel temperatures in the East zone at 0.3 m, 0.4 m, 0.5 m and 0.7 m.

14930 seconds:
Strong increase of the shroud temperature at 0.2 m (rate up to 1.6 K/s);
Failure of the thermocouple at 700 mm (fuel rod).

15180 seconds:
Failure of the thermocouples at 0.3 m and 0.4 m (fuel rod);
Decrease of the shroud temperatures at 0.6 m;
Strong increase of the shroud temperatures at 0.2 m, 0.3 m and 0.4 m;
Strong increase of the shroud temperature at –0.14 m (below the bundle support plate).

At 12500 s, just after the oxidation escalation, the first material relocation took place. In accordance with the results of the code calculations ([2], see Chapter 3.1.1.4) it is confirmed that in this time period metallic U-Zr-O melt was formed and relocates to lower bundle zones. The melt heats up the rods at those positions as detected by the thermocouples (see Figure 4).

After this event during 2000 s the bundle temperatures follow the given heat-up heat scenario until the temperature increases in the West zone at 14350 s and 380 s later in the South or South-East zone indicating relocation processes. During these events, a temperature decrease was detected in the opposite zone, which can be caused by a blockage formation leading to higher fluid velocity or to an increase of the heat transfer coefficient between the rods and the gas, respectively.

It should be mentioned, that such asymmetrical events could not be simulated by the present state of the codes based on 1-D approach. Nevertheless, efforts are already underway since many years to simulate such 2-D effects by using a porous medium approach. If such a code will be applied to simulate this degradation phase, the initial event, i.e. the failure of the cladding, will still underlay certain statistics. This is caused by local mechanical weaknesses of the cladding or asymmetrical growth of the zirconia oxide layer or maybe perturbations in the bundle power distribution.

Nevertheless, ATHLET-CD could predict material relocations during this period of the degradation phase between 15000 s and 15500 s. It is obvious, that none code can match without manual modifications the detected times.

The failure of thermocouples is probably caused by material relocation, which destroyed the W-Re-HfO_2 contact and its protective coating. Due to this relocation, the amount of fuel and the heat source, respectively, are reduced at the position of the melt release. Therefore, the shroud temperatures decrease due to the reduction of the radial heat fluxes from the bundle to the shroud. Below this position, the shroud temperatures increase, because the radial heat flux from the bundle to the shroud increases due to higher temperatures in the bundle. On the one hand, this temperature increase is caused by the heat exchange between the relocated material and the partly intact rods, whose temperatures are lower at these bundle elevations. On the other hand, this temperature increase can enhance the oxidation of the Zry cladding. However, the decrease of the free surface area accessible for the gas flow and the increase of the oxygen diffusion length respectively, act against this temperature effect. Finally, taking into account the heat losses to the shroud, the temperatures first increase and then decrease reaching a higher temperature level as before the event, i.e. a quasi steady-state heat flux conditions are reached again. This temperature behaviour is already confirmed by code calculations in which the processes are simulated.

Because the temperature increase occurs at levels near and above the lower grid, which could significantly affect the downward movement of the material, it is justified that the material accumulation mainly took place above the grid. This leads finally to the formation of the molten pool.

The strong increase at – 0.14 m could only explained by the failure of thermocouple induced by relocated material detected in PIE at the bundle support plate.

2.4.1.2 Material distribution

A series of the non-destructive and destructive post-test examinations were performed on the bundle after the FPT0 experiment. The results confirm that a significant part of the fuel bundle liquefied and that the relative extent of fuel damage is comparable to that of TMI-2 with a molten plug under a cavity surrounded by a uranium-rich crust [50]. In the lower and upper areas, fuel rods are less damaged.

On the lower levels, there is a heavy degradation gradient, with many previously liquefied materials and debris. The guide tube does not remain above 0.11 m, and has more or less melted below.

Channel blockage can be seen from cuts taken between 0.149 m and 0.25 m; the blockage shows the top of the previously liquefied agglomerate. A type of chimney exists near the Western stiffener. Circumferential cracks and porosity are presents in the solidified mass.

Above the pool, two cuts (0.268 m and 0. 287 m) show a central hole surrounded by a thick crust, which attacks the first inner shroud wall, with the chimney in the Southwest. In the cuts taken from the 0.398 m to 0.792 m elevation range, it is seen there is a ring of external rods around a central void; these rods have been attacked from the bundle centre. The upper grid remnants can be seen on levels 0.773 / 0.775 m.

On cuts taken at 0.921 to 0. 940 m, the central part is partially filled with a porous structure, and the claddings of the external rods are largely opened. On top cuts, nearly all the pellets can be seen, with the same clad openings, and a better initial geometry.

Heavy oxidation can be observed on several levels along the bundle, e.g. in Figure 5 and Figure 6. Figure 5 shows a PIE examination of a slice at the level 0.787 m and the erosion of the outer fuel rod pins.

Figure 5: Post Irradiation Examination: Visual Observation of level 0.787 m

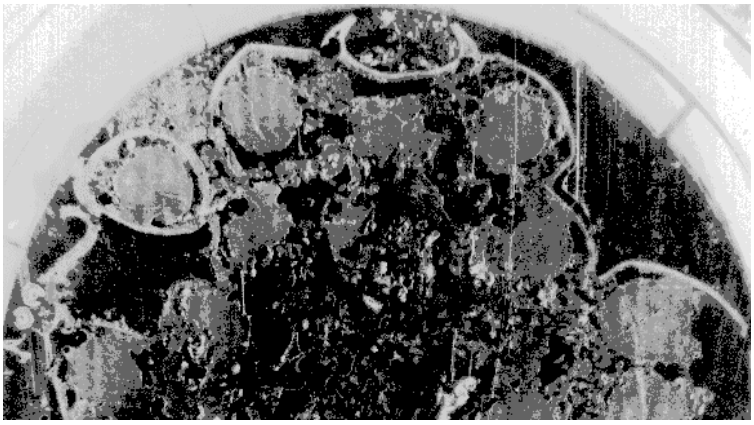

Figure 6: Post Irradiation Examination: Macrograph at level 942 mm, where most fuel pellets were reduced from an original diameter of 0.0082 m to 0.006 – 0.007 m

In Figure 7 a micrograph of corium at level 940 mm is shown; and in Figure 8, the EPMA linescan No. 9 at the same level is plotted. The corium in Figure 6 and Figure 7 appears as a rather homogeneous porous structure of a purely ceramic $(U,Zr)O_{2+x}$ phase, surrounded by the oxide layer along the bundle periphery. The maximum O-content of the ceramic phase in the equilibrium phase diagram is close to 0.666 that is slightly below the measured one, but surely in the range of uncertainty of the measurement.

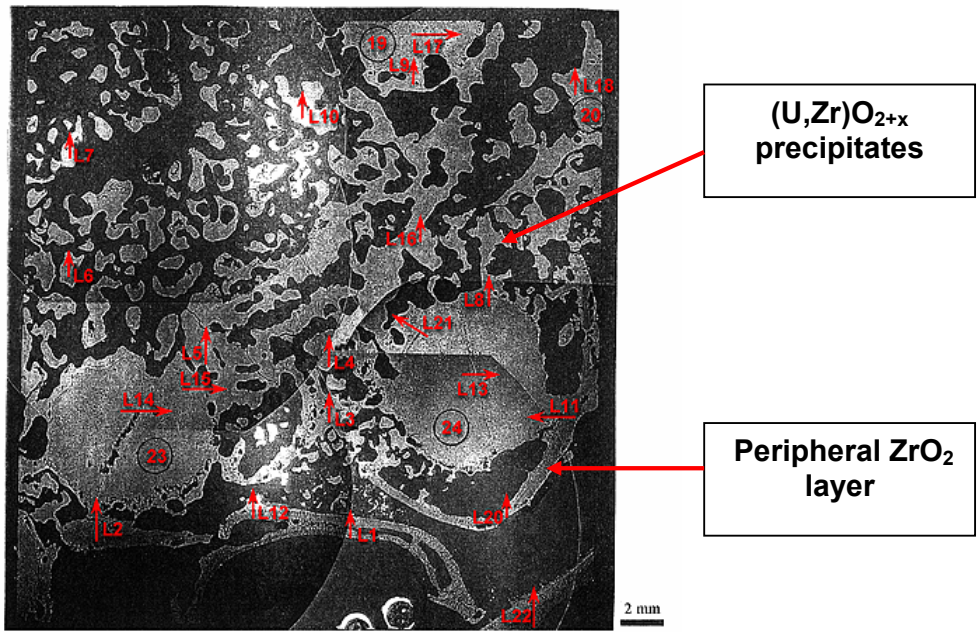

Figure 7: Macrograph at level 0.94 m.

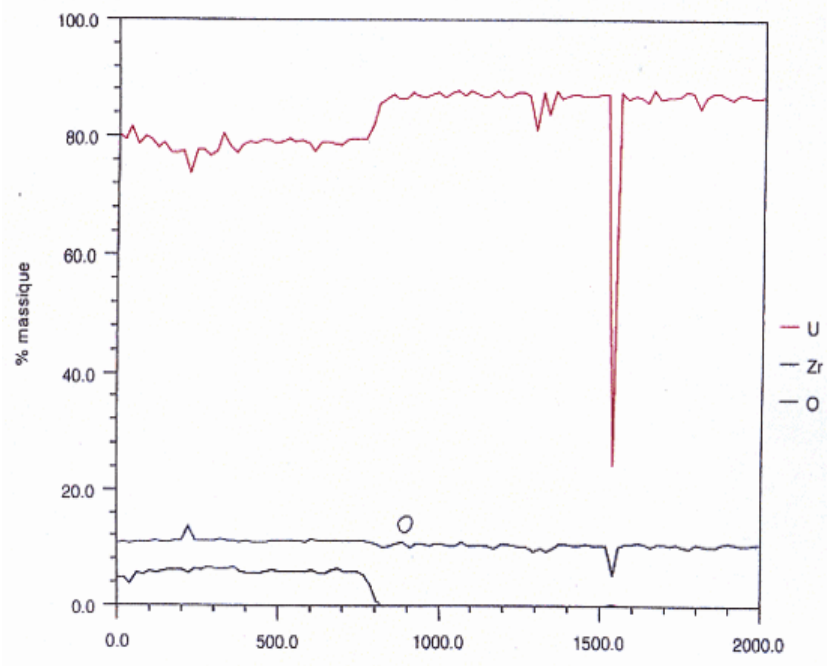

Figure 8: EPMA linescan No. 9 at level 0.94 m.

Table 1:
Composition at level 0.94 m

Isotope	wt%	Atoms
^{238}U	80	0.336
^{91}Zr	5	0.055
^{16}O	11	0.688

In [2] it was concluded that the melt exists as mixture containing 86 mole percents (mol-%) of $(U,Zr)O_{2-x}$ and 14 mol-% of α-Zr(O); this implies 23 mol-% of O in Zr(O). This is almost the maximum (30 mol- %) oxygen content in Zr(O) according to the Zr-O phase diagram. On the pseudo-binary phase diagram, this gives a monotectic composition (see Fig. Figure 9) with a melting temperature of 2673 K [16].

However, during the oxidation and degradation phase no steam starvation exists in the upper part of the bundle and therefore it is unlikely that metallic α-Zr(O) remains un-oxidised.

At this level, an analysis was performed along a different line indicated UO_2-α-Zr mixture - but in different concentrations [2]. Two separate liquids are found, the first with 82 mol % content and the second with a UO_2 content of 28 mol %. This implied a temperature above 2670 K - the temperature at which, according to the pseudo-binary phase diagram (Figure 9) the two liquids begin to coexist.

Another interpretation of the corium appearance is based on comparison with the observations in the separate-effect tests:

The temperature history in the upper zone of the FPT0 bundle can be evaluated from the stiffener thermocouple TCW20 installed at elevation 0.9 m (see Figure 4). These data show that temperature at this elevation attained its maximum during the oxidation stage and apparently did not exceed 2500 K. For this reason, the microstructure observed at these elevations can be directly compared with observations of the crucible tests [51] performed at 2200°C. Indeed, in these tests the UO_2 crucible was partially dissolved by molten Zry up to complete melt saturation. The saturated U-Zr-O melt at 2200°C decomposed in two phases (metal + ceramic precipitates) on cool down, Figure 10, and both volume fraction and composition of the ceramic phase were measured. The measured percent phase-area of ceramic phase ≈ 60% (that determines the volume fraction of precipitates) is rather close to the percent phase-area of ceramic phase in Figure 7. The composition of ceramic precipitates in Figure 10 corresponded to $(U_yZr_{1-y})O_{2\pm x}$, with y ≈ 0.86–0.9, also in a satisfactory agreement with ceramic particles composition measured in FPT0 test at elevation 0.94 m, (see Table 1),

i.e. U (80–82 wt.%), O (~ 11 wt.%) and Zr (~ 5 wt.%), which roughly corresponds to $(U_{0.84}Zr_{0.16})O_{2\pm x}$.

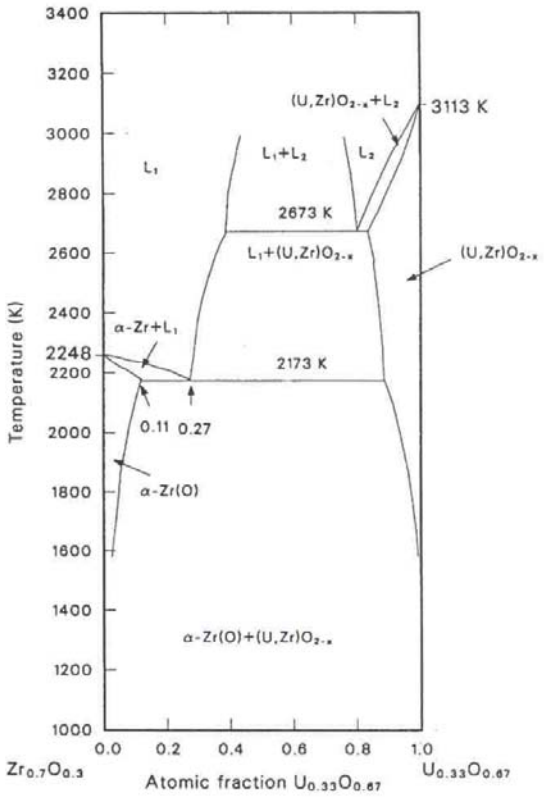

Figure 9: Quasi-binary U-Zr-O Phase diagram

Therefore, it can be concluded [11] that microstructure observations in the upper zone of the FPT0 bundle are in a good agreement with that of the crucible tests if one assumes that (i) in the upper zone, just after the oxidation phase, a metallic fraction formed a solid two-phase mixture on cool-down, (ii) then during the bundle heat-up phase the solidified melt relocated downward leaving voids in the remaining ceramic structure at 0.94 m (Figure 7).

In this case, the main difference between two microstructures (in Figure 7 and Figure 10, respectively) is connected with the size of the ceramic precipitates: in FPT0 were observed relatively large (500-2000 μm) particles in comparison with smaller particles in the crucible tests (50-100 μm). However, such a difference can be apparently explained by various cooling rates in the two tests. Indeed, the cooling rate in FPT0 at elevation 0.9 m was essentially lower (≈2 K/s: from 2473 C to 2273 C during 100 s) compared to the crucible tests). In the recent FZK crucible tests ([52], [10]) with high cooling rate ≈ 10 K/s, ceramic precipitates had intermediate sizes, 400-600 μm.

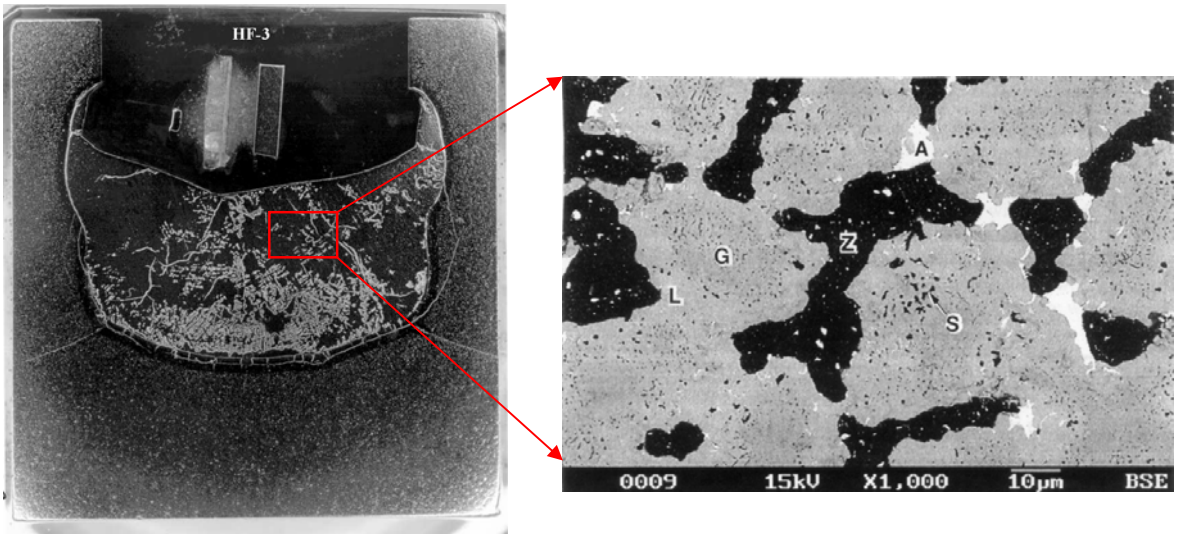

Figure 10: Micrograph of the Central Melt Region (2200°C, 428 s) in the tests on UO_2 crucible dissolution by molten Zry [51], G = Zr-rich Inner Ceramic Zone; L = Outer Ceramic Zone; Z = Zr(O) Alloy; A = U(O) Alloy; S = Inclusions of Zr(O) in the Ceramic Phase

2.4.2 Status of the Dissolution Models

Based on the short description in [2] an update of the dissolution models implemented in the different codes is given below, whereby some detailed features of the models are discussed. Additionally, a short description of the relocation models is given.

The different codes have different options for calculating the dissolution of UO_2 and ZrO_2:

- ICARE2 [4] allows the user to choose different models. Dependent on the Rayleigh Number the convective or diffusion model of Kim-Olander [53] can be applied. The dissolution stops when the liquidus limit is reached determined by the actual cladding temperature. Another option is to use the diffusion model of Hofmann [54], which considers an incubation period until a defined mass fraction limit of UO_2 in the mixture is reached. Above this limit, the kinetics changes to a parabolic one. This observation contradicted to the measurements performed later by Hayward [55], who observed cessation of the dissolution process after melt saturation. In order to resolve this contradiction, a new test series on UO_2 crucible dissolution by molten Zry at 2100 and 2200°C was performed by Hayward in co-operation with Hofmann [51] in the framework of the CIT Project of the 4th framework programme [56]. In these tests it was shown that the major part of dissolution occurred until saturation limit of melt was attained. The dissolution process also continued beyond the saturation limit, however, with a much slower rate. Later it was shown experimentally and analytically that continuation of the dissolution beyond the saturation limit may occur owing to non-equilibrium conditions of the crucible tests with temperature difference between crucible walls and melt (see section 3.5.2 below). For the dissolution of ZrO_2, a parabolic kinetics correlation is applied [57]. This contradicts to the measurements performed by Hayward [55], where non-parabolic dissolution behaviour was observed, however, during a relatively short initial period of the crucible tests. After this period, dissolution (erosion) turned to the reverse process of oxide growth (corrosion) with the expected parabolic behaviour, in accordance with analytical predictions [58].

  The coupling of UO_2 and ZrO_2 dissolution is performed in the end of a time step by verification that in the resultant mixture, to which the dissolved UO_2 and ZrO_2 (considered as separate processes during the time step) were added, the saturation limit is not exceed. The dissolutions are stopped when the saturation is attained during the time step.

  There is no coupling with Zry oxidation by H_2O; this chemical reaction is treated after dissolution processes during a time step. The temperature of mixture U-Zr-O is constant during the chemical interaction.

  In order to consider simultaneous processes of UO_2 and ZrO_2 dissolution and Zry oxidation in a self-consistent manner, a more general model developed by IBRAE [58] was implemented in the ICARE2 code as an additional option. This model has been validated using the data measured by Hofmann, Olander and Hayward and it was further developed in co-operation with JRC on the basis of new RIAR tests in the framework of COLOSS Project (see Section 3.4.4).

- In ATHLET-CD [5] and in KESS [59] the combined diffusion-/convective model of Kim-Olander [53] or a modified correlation based on Hofmann's data [60] can be used. The dissolution of zirconia was not considered, because theoretical estimations

based on Hofmann's correlation showed, that in typical reactor cases the time constant is too short to obtain significant dissolution of ZrO_2.

- In SCDAP/RELAP5 [60], the rate of fuel dissolution by molten Zircaloy is calculated by the correlation based on Hofmann's data, similarly to the corresponding option in the ICARE2 code. The calculated amount of fuel dissolution is limited to the amount at which equilibrium occurs as determined by the liquidus line in the ternary phase diagram.

- In MELCOR, the transport parameter for fuel dissolution by molten Zircaloy is a user input. In the benchmark study in [2] KAERI set this parameter to 0.57% UO_2 in the inner ring and to 0.33% in the outer one, respectively.

In all codes, the dissolution process is ceased if a breach occurs in the cladding oxide shell. The downward movement of the melt is simulated by the relocation models; it is briefly described as follows.

2.4.3 Status of the Relocation Models

2.4.3.1 MELCOR code materials relocation model

In the MELCOR relocation model the momentum equation for the melt velocity is not solved. The steady generation of molten materials is assumed "with all materials generated within the time step reaching its final destination within that step". Practically, the melt velocity is assumed infinitely high. The distribution of relocated mass along the rod surface is completely determined by the refreezing process. Different regimes of melt relocation (films or rivulets) are accounted for only by appropriate adjustment of refreezing coefficients. The regime of flowing down (film, rivulet, and drop) on the characteristic melt velocity is not accounted for. The influence of temperature and solid fraction value on the melt viscosity (and thus, on the melt velocity) is not described.

Thus, the description of melt relocation is presented by the heat exchange considerations (see below) and there is no specific model for regimes of melt downward flow.

There is no specific model for melt relocation in the fuel rod gap.

The model for the flow blockages formation is based on obvious geometrical considerations.

The model for the heat transfer between relocating materials and fuel rods is based on the heat balance principles. The heat exchange rate is determined by user-specified heat transfer coefficients defined for each material. The amount of heat transferred to the rod structure is calculated at the end of the global time step with accounting for the variation of the melt temperature during the time step.

The melt solidification model is based on the heat balance consideration. If the material interaction (eutectic) model is activated, the solid fraction has the same composition as the remaining liquid. If the eutectic model is not active, materials flow independently whenever their melting point is reached. The effects of melt oxidation and rod materials dissolution on the solid fraction formation are not accounted for within the time step, or, in other words, there is no model for oxidation of relocating or relocated melt.

2.4.3.2 SCDAP/RELAP5 code materials relocation model

The molten materials are assumed to flow down in the form of drops. The other regimes of flowing down (films, rivulets) are not considered. The drops are presented as hemispheres with radius r_d = 3.5 mm. The momentum equation for the melt velocity is not solved. The velocity of drop motion is constant and equal to 0.5 m/s. The relocated mass distribution along the rod surface is completely determined by the refreezing process. The influence of temperature and solid fraction value on the melt viscosity (and thus, on the melt velocity) is not accounted for.

In the case of liquefied fuel and cladding, in a ballooned region the melt "is expected to flow downward inside the fuel rod and collect at the elevation at which the fuel rod cladding gap is small enough to block the flow". However, no details on the gap candling are presented in the code description and this phenomenon is not modelled in the code.

The model for the heat transfer from the relocating drop to the fuel rod accounts for the rod multi-layered structure and the drop motion. The amount of heat transferred to the rod structure is calculated at the end of the global time step.

The conductive heat flux from the drop to the fuel rod, convection and radiation heat fluxes and heat generated by drop surface oxidation are accounted for in the thermal balance equation. The change of drop temperature is determined by the end of the global time step. Supposedly, refreezing takes place if the melt temperature becomes smaller than the solidification temperature. Within the framework of the alternative method, a drop is modelled to stop (and refreeze) when it appears at the surface with a temperature smaller than some user-defined value. The effect of the current chemical composition of the drop on the solidification process is not mentioned.

2.4.3.3 ICARE2 code material relocation models

In the ICARE2 code (V3mode1), two alternative models are being used for the early degradation phase: simplified CAND model and mechanistic DROP/DROG model. To generalize the relocation in all possible media the 2-D corium movement model was developed.

- CAND model

A mixture can flow down if its liquid mass fraction exceeds a threshold value given by the code user. The velocity of flowing down is assumed constant (corrected by the solid fraction in case of solid/liquid mixture). The candling process is supposed to have a short duration ("like a thermal shock"). Thus, the momentum balance equation is not used.

There are no specific models for different regimes of melt downward flow and for the melt relocation in the fuel rod gap.

The grid effect (trapping) is accounted for by user-defined "mixture velocity in a mesh containing grid" ($V_{grid}^{m} = 0$ by default). Without changing the zero value of V_{grid}^{m} in the input data set, all the flowing materials are trapped in meshes where grids are located.

The heat exchange with relocated material is considered much faster than all other heat exchange modes (convective, radiative, etc.) and it is described in terms of thermal shock front.

When describing solidification, the thermal resistance of the liquid film and solid crust are being neglected. Solidification occurs when mixture temperature is below T_s^m (its solidus temperature). The solidus temperature, latent heat of solidification and liquid fraction of the mixture do not depend on mixture composition.

- DROP/DROG model

The mixture is assumed to emerge from the breach on the surface of the rod instantaneously. Then, it is divided into several elementary parts (drops, rivulets) or it starts to move down as a whole in accordance with the viscous-gravitational drop/rivulet formation mechanism.

The model considers various types of downward flow such as droplet, rivulet of different length and film flow and it describes droplet-rivulet transitions.

The motion of mixture is described by the system of differential equations obtained by the integration of the hydro-dynamical Navier-Stokes equations (mass, momentum and energy balance) over the volume of the moving liquid element with taking into account boundary conditions on the liquid-solid and liquid-gas interfaces.

The model takes into account capillary effects (contact angle hysteresis, contact line resistance to displacement, wetting of the fuel rod surface) and viscous effects (viscous drag force, laminar/turbulent flow regimes).

The model describes non-stationary heat exchange of the liquid mixture with arbitrary temperature distribution along the fuel rod and accounts for the heat exchange influence on the mixture properties (melting/solidification, temperature dependence of viscosity and surface tension). Solidification occurs when the mixture temperature is below its solidus temperature.

The model also describes the gap candling process that is the flowing down inside the gap formed between two cylindrical structures (cladding and fuel pellet).

- 2-D corium movement model

The general model for the 2-D corium movement describes the accident development from the very beginning up to the late phase (massive debris formation) within the framework of the same formalism. All core or bundle configurations are considered as a porous medium with specific characteristics (porosity, permeability, passability). The basic equations have the same form and the same nodalization is used throughout the whole accident.

Mass, momentum and heat balance equations are solved. Both downward and radial melt relocation are described. Momentum balance equation is represented by generalised Darcy equation with inertial term.

The coefficients of absolute and relative permeability (describing flow at relatively low Reynolds numbers) in the case of downward relocation are determined in terms of axially symmetrical laminar film flow. Capillary effects on the flow regime are not accounted for and drop/rivulet flow is not considered.

Absolute and relative passability for the rod configuration (important at high Reynolds numbers) are determined in terms of turbulent flow in a pipe.

Gap candling is not modelled.

2.4.3.4 ATHLET-CD code material relocation models

The 1-D model describes the down-flow of low viscous melt rivulets on well-wetted surfaces combined with simultaneous crust formation by assuming laterally a uniform thickness of the rivulet. For the liquid film the mass, momentum and energy conservation equations are solved. The presumption of a constant mass flow rate of the melt rivulet is made with respect to the momentum equation. During each time step, in the total power balance of melt the following power components are accounted for: (1) the convective heat transfer rate between the melt and the fuel, (2) the heat transfer rate between the surface of the melt rivulet and the fluid, (3) the radiation heat transfer rate to the neighbouring rods, (4) the heat release due to oxidation of the melt and crust, (5) and the decay heat power. Instead of using the momentum equation for the moving melt, the melt relocation velocity can also be given. The blockage formation is limited to the rod-related flow area, i.e. 2-D effects are not considered.

For the crust, additionally, a mass conservation equation and the energy balance is taking into account by considering the heat fluxes on the crust surface. The re-freezing temperature is assumed as constant and the solidification of the melt starts, if the cladding temperature is below the refreezing temperature or the conductive heat flux heat in the cladding is greater than the convective heat flux from the melt to the crust. After complete solidification of the melt the conductive heat flux between the crust and the fuel rod, the radiation heat transfer to the neighbouring rods, the heat release due to the crust oxidation and the decay heat are calculated.

As reported by GRS [33] the 2-D porous medium code MESOCO developed at IKE was implemented in ATHLET-CD. The model calculates the time-dependent evolution of the temperatures of the solid material, the melting processes as the melt relocation during the phase of severe core damage leading to the formation of a molten pool. Hereby, the formation of large connected crust regions and the melt pool above is modelled. The complex interactions between the solid, the melt and overheated steam/hydrogen mixture or non-condensable gases are based on a quasi-continuum approach. Three non-stationary energy conservation equations for the solid, the melt and the flowing gas as well as mass conservation equations for each phase are solved. In solid and gas phases, for each material component separate mass balance equations are available. In the momentum equations written for the melt and the gas, the Darcy-law [61] is used. During the melt relocation the gravitation, the hydrostatic pressure differences in the melt as well as the capillarity are simulated.

2.4.4 Discussion on the Dissolution and Relocation Processes

As reported in [16] the event at 12500 s (see above) during the oxidation phase may be caused by the relocation of metallic U-Zr-O melt. The earlier code analyses predict that the fuel remains intact, only SCDAP/RELAP predicted substantial dissolution. However, as mentioned in [2], the significant material relocation (events at 14350 s and 14750 s), which finally leads to a molten pool, could not be predicted by any pre-test calculation of the first Phebus FP experiments. In post-test calculations, IRSN used a special set of input data that forced material relocation at a user specified time in order to reproduce the thermal behaviour.

At that time, on one hand, developers were still working on simulation of the relocation process of the metallic melt. On the other hand, the code users do not strongly request an estimation of the amount of melt, which could be formed if very high temperatures could be maintained during a significantly long time. Such conditions exist during the TMI accident and based on the post-accident analyses a more profound estimation could be made [50].

Due to the fact that in most of the codes the melting of ceramic material was assumed to start when the temperature reaches the eutectic temperature of the UO_2/ZrO_2 mixture (2800 K), the codes predict neither significant mass relocation nor formation of a molten pool.

After publication of the Phebus FPT0 tests results, one decreases the melting temperature of the UO_2/ZrO_2 mixture. Due to fact that below 2800 K a material interaction between UO_2 and ZrO_2 cannot be physically grounded – this temperature can be considered only as temperature criteria for the relocation of ceramic material.

Based on the experimental results several possibilities were discussed mainly among the developers and in the Bundle Interpretation Circle:

Relocation of solid ceramic material

The ceramic material is relocated in the solid state where the collapse of the rods is caused by thermal stresses - an examination was done by IRSN [62] using ICARE2 code. In lower and cooler bundle regions, metallic components are present and can dissolve the ceramic material. This leads finally to the observed molten pool.

Melt formation due to reduction of the melting temperature

After the relocation of the U-Zr-O melt during the oxidation phase (t ~ 12500 s) metallic bundle components (Zry, Fe, Ag or some amount of U-Zr-O melt) are not completely relocated to lower bundle regions, i.e. a part of these components remains at inner ZrO_2 or outer UO_2 surfaces or stick between the fuel and the cladding, respectively. Due to the presence of those metallic components, the melting temperature of the ceramic material is significantly reduced. After cladding failure, the melt mixture relocates and due to the melting of the material in the lower bundle part - little by little - the molten pool is formed.

Melt formation due to dissolution

During the temperature escalation (see Figure 4), the metallic Zircaloy of the cladding is liquefied and the melt interacts with the UO_2 pellet leading to a partial dissolution of the fuel. After cladding failure, it is assumed that a significant part of the melt above the upper grid sticks in between the pellets and the non-breached cladding of the neighbouring rods, i.e. so-called local molten pool(s) is (are) formed.

The cladding failure itself can be caused either due to simultaneous dissolution of the zirconia until the remaining zirconia cladding lost its mechanical stability, or by mechanical failure due to a local internal pressure build-up in the rod [58]. In this case the dissolution of UO_2 and ZrO_2 by the metallic melt of the local molten pool continues – until the liquidus limit is reached (see above Section 4.3.2).

Formation of local molten pool in the upper zone of bundle was apparently detected in the FPT0 test as described above in section 3.4.1.2. Consideration of the molten pool geometry allows significant improvement of the fuel dissolution modelling.

Indeed, in the intact geometry of the fuel rods a rather limited dissolution of fuel pellets, <10%, can be predicted by various codes (rather than ≈ 35-40% detected in the test [16]. An improvement in the ICARE2 predictions was attained by the application of a parametric model, which restricts dissolution by the solidus limit - rather than the liquidus one [63]; however, such a model significantly overestimates dissolution in the crucible tests.

On the other hand, dissolution of fuel pellets in configuration of the molten pool predicted by the advanced dissolution model [11] (see Section below 3.4.5) is essentially higher and can attain 60% (depending on the molten pool geometry), in a much better

agreement with observations. This is illustrated by comparison of calculations by the same code for the two different melt configurations in Figure 11 (intact geometry) and Figure 12 (molten pool geometry).

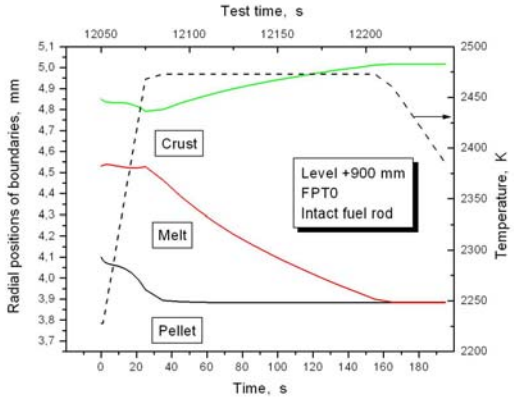

Figure 11: Evolution of oxidized cladding layers in the upper zone (0.9 m) of the FPT0 bundle after Zry melting (for fuel rod intact geometry) - SVECHA code calculations [11]

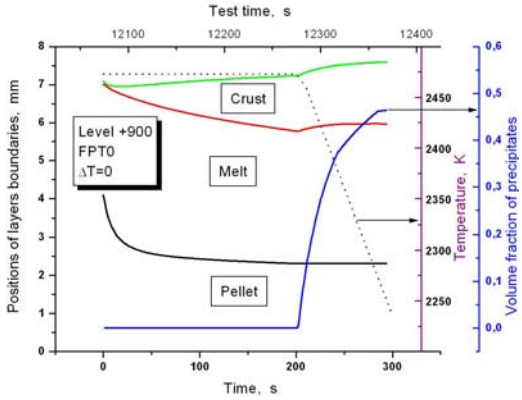

Figure 12: Evolution of oxidized local molten pool layers in the upper zone (0.9 m) of the FPT0 bundle after Zry melting - SVECHA code calculations [11]

At the same time, these figures illustrate the effect of reduction of the melt oxidation in the local molten pool geometry owing to a larger *V/S* (volume to surface) ratio of the molten material. This explains further downward relocation of non-oxidized metallic melt from upper elevations during subsequent stages of the test.

In lower bundle regions, the available metallic Zry and the relocated metallic melt leads to a complete dissolution of the ceramic material, i.e. to the pool formation, during the late stage of the experiment (see Section 3.5 below).

Based on experimental findings in the CORA ([64], [65]) tests and on the interpretation of other tests in [66], the assumption was made [67] that after clad failure only during an initial phase the relocation process is dominated by the relocation of droplets and rivulets, which consist of metallic melt. Their relocation velocity v is around 0.5 m/s. A large amount of melt sticks in between the rods and forms so-called "local molten pools". It was concluded that the massive melt (or "slug") moves down relative slowly (v = 0.001 m/s). The oxygen flux due to the steam atmosphere to those "molten pools" leads to the precipitation of $(U,Zr)O_{2-x}$ particles in the melt which significantly increase melt viscosity and thus reduce relocation velocity (along with a solid crust formed in the steep axial temperature gradient and preventing melt from quick relocation). Consequently, the overlapping of these relocating "molten pools" leads finally to the "large" molten pool detected in the post-test examinations at low elevations.

It is worthwhile to note that the relocation velocity of the oxidation front from elevation 0.7 m to elevation 0.4 m (during ≈ 400 s) detected in FPT0 test, Figure 4, is of the same order of magnitude, ~ 0.001 m/s, as in the CORA tests. This allows an assumption that the same "slug" mechanism is responsible for slow melt relocation also in FPT0 test.

Similarly, to the FPT0 test, formation of local molten pools in the upper zone of bundle has been observed in the QUENCH-02 test [68], see Figure 13, and the QUENCH-03 tests [69]. Keeping in mind that the test temperature did not exceed 2200°C and molten material existed less than 100 seconds in the hottest zone before freezing by reflooding, one can consider these micrographs as "snap-shots" of a real picture of melt configuration shortly

after cladding melting. Therefore, the conclusion about melt agglomeration in local molten pools in-between the fuel rods, was derived from these observations [11].

Melt Formation by melting of ceramic materials

At IRSN an analysis with the porous medium model (see above) – option of the ICARE2 code - was performed where the bundle consists of close-packed 0.01-m-diameter UO_2 spheres filling the bundle; the porosity ratio is about 50 %. The effective heat conductivity of this porous medium is described by the Imura-Yagi correlation or, as an alternative option, by a new heat transfer model, which considers the porous medium as a uster of true cylinders (fuel rods). An external Zircaloy layer was added to the UO_2 debris to account for the Zircaloy-steam reaction where the surface exposed to steam was the same as for cylindrical geometry but up to now no material interactions (dissolution/solidification and other compositional effects) could be simulated. However, the melting and relocation of the UO_2 was simulated by means of a user-defined relocation temperature. By setting the solidus temperature to 2650 K and the liquidus temperature to 2720 K, which in accordance to the liquidus temperature measured at FPT0 corium samples taken the molten pool (see Chapter 1.5) satisfactory results with respect to the bundle degradation were obtained. The reason is that steeper radial temperature gradients and higher bundle temperatures were calculated compared to the standard ICARE2 calculation applying the model based on the representative concept of a rod-like geometry. However, in the latter the treatment of significant geometry changes caused by fuel swelling – not evident in FPT0 - or by severe bundle degradation and their influence on the heat transfer appears not adequate.

The porous medium approach implemented in ATHLET-CD was up-to now only applied for the Phebus particle bed test FPT4 [70].

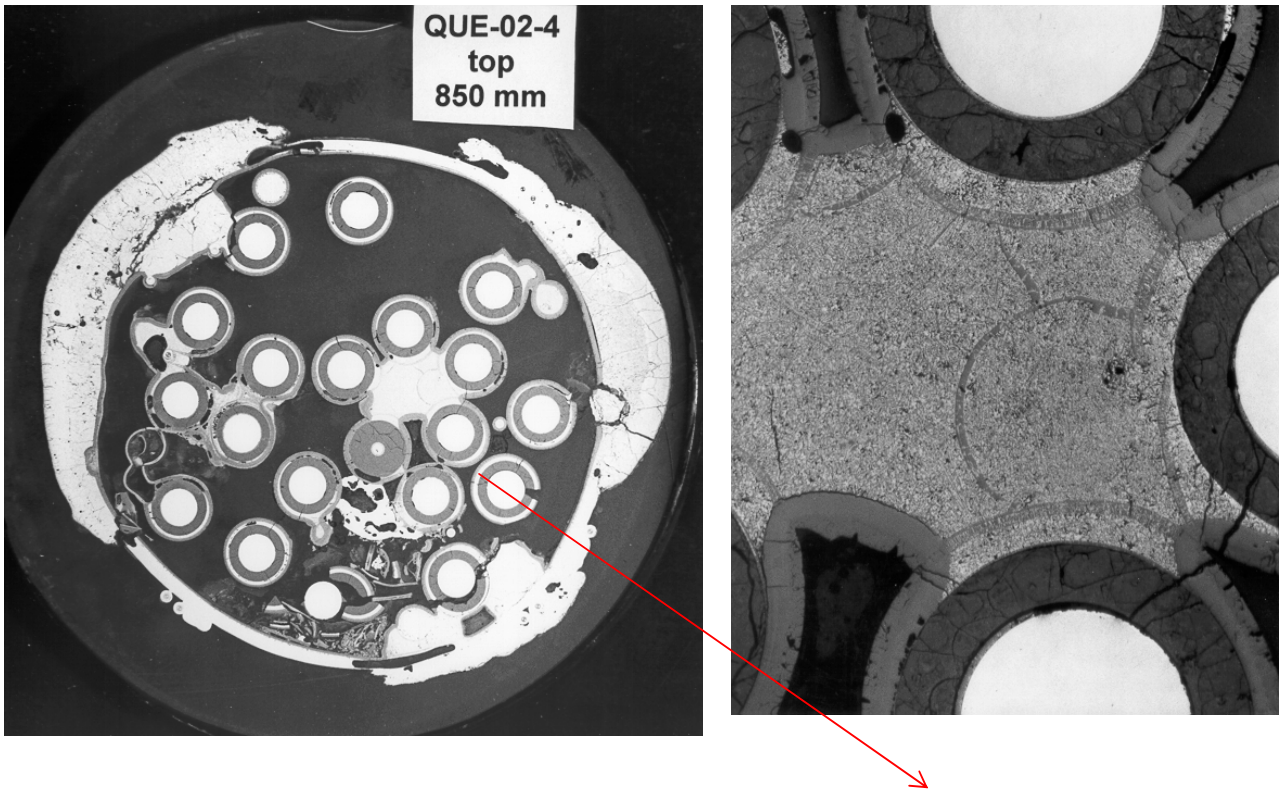

Figure 13: Cross section Q-02-4 of QUENCH-02 test bundle (elevation 0.85 m

Concluding remarks

A previous assessment of the different models or model assumptions respectively will be discussed now using the listed sequence above:

The mechanical failure of the partly damaged fuel rods caused by thermal stresses underlies a certain statistic in time and space. Therefore, the relocations occur instantaneously and they can be observed as an intermittent process between 14350 s and 14730 s in the test. Furthermore, a possible relocation of fully oxidized material during the oxidation phase can be also explained. However, the detected fuel dissolution or melting (see above) in the upper part of the bundle seems to contradict this assumption. At the bundle top, the steam should have oxidized the metallic Zry or it should have relocated before significant dissolution occurs - as presumed for the bundle zones below.

The decrease of the melting temperature due to the presence of metallic melts and the assumption of subsequent clad failure give a consistent picture with respect to the discontinuous relocation process. However, it seems questionable that metallic melts remains at higher bundle positions, because due to their low viscosity these melts should relocate during the oxidation phase. If not, these metallic components should have completely oxidized in the steam atmosphere.

The assumption that a significant part of the U-Zr-O does not relocate during the oxidation phase is also consistent with the conclusions drawn from the thermocouple readings. However, it is questionable – as in the previous case - whether a complete oxidation of the melt could be prevented during this relatively long period.

The formation of relatively small molten pools between the rods during the oxidation phase combined with the relocation of droplets and rivulets in the initial phase gives a well agreement concerning the material composition measured at the top of the bundle (see above part c of this Section). However, the assumption that the relocation of the ceramic material occurs continuously with a steady velocity apparently contradicts to the conclusions drawn from the thermocouple readings. The discontinuous relocation process might be explained assuming that the spacer grids act like obstacles. In comparison with the rod-like geometry the surface/volume ratio of the "molten pools" is smaller, therefore the oxidation is more limited (see above Figure 11 and Figure 12). This may prevent a complete oxidation of the melt during the time interval of ca. 2000 s between the first relocation processes and the significant relocation of ceramic material.

The assumption that the melting of UO_2 occurred at the liquidus (eutectic) temperature is a rough approach, because there exist no well-mixed UO_2/ZrO_2 mixture, which could enable a relatively rapid interaction between urania and zirconia. Finally, the diffusion coefficients of Zr and U are lower compared to that of the liquefied metallic components. In [2] it was also discussed that metallic components may lead to significant reduction of the melting of UO_2. Metallic components were locally found in the samples by the microstructure analyses but at such high temperatures (about 2800 K) they should already have been oxidized.

2.4.5 Progress in the Modelling on Dissolution and Melt Oxidation

At present, great efforts are done in the SCA COLOSS to investigate the simultaneous dissolution of UO_2 and ZrO_2 by molten Zircaloy. Separate effect tests are performed at RIAR ([71], [72]) and the analytical work is done at IBRAE [73] – both organisations were

subcontractors of JRC. Additionally the modelling work on U-Zr-O oxidation [8], [9], [11], [73] was done at JRC in close co-operation with IBRAE modellers and FZK experimentalists.

As it was pointed out in the previous chapter, the simultaneous dissolution of UO_2 and ZrO_2 by molten Zircaloy occurs in rod-like geometry and it could lead to cladding failure. Furthermore, this process can be dominant in formation of the molten pool.

The oxidation of metallic melt is important, because oxidation limits the dissolution process. Furthermore due to the formation of participates the viscosity of the melt increases and influences the relocation process. If complete oxidation occurs, the material solidifies. During quenching of a partially molten bundle ([74], [75], [76]) or a reactor core ([77], [78]), the oxidation of melt produced a significant amount of hydrogen. It should be noted, that GRS examined the relevance of hydrogen production due to melt oxidation for Phebus FP [79]. It was found that this produced mass of hydrogen was very small compared with that produced by cladding oxidation. This finding makes questionable the conclusion from COLOSS that the oxidation of relocating or relocated melt is a potentially large contributor.

In the COLOSS project, the main objective was to study these processes experimentally by separate effects tests as well as analytically in order to reach an accurate simulation of the processes themselves. The newly developed U-Zr-O oxidation model was applied for the interpretation of the integral tests QUENCH–02 [68] and CORA–W2 [80], respectively. Recently it was utilized for stand-alone calculations with respect to PHEBUS FP tests [11]. IRSN developed also the so-called "MAGMA oxidation model" derived from the JRC/IBRAE modelling work on oxidation [8], [9], [10], [11]. The MAGMA oxidation model was implemented in ICARE/CATHARE code; it is based on the so-called "MAGMA components" representing molten mixtures [81]. In this report only a short overview of the activities are given and the main results obtained up to now are discussed.

2.4.5.1 Simultaneous dissolution of UO_2 and ZrO_2 by molten Zircaloy

The RIAR tests are carried out using a tungsten resistance furnace filled with argon ([71], [72]). The sample consists of a UO_2 crucible, a central rod of stabilized ZrO_2 and a Zry charge placed in the gap between crucible wall and central rod. An Y_2O_3 disk has been added to prevent interaction between the crucible bottom and the Zry charge. Temperature control of crucible sidewall during experiment is realized by two thermocouples and the melt temperature is controlled by a two-beam pyrometer. The test procedure consists in fast heating of the sample to a specified temperature, holding the sample at this temperature and final cooling. During the tests, the simultaneous dissolution of the crucible wall and central ZrO_2 rod by Zircaloy rich melt takes place (see Figure 14).

Two series of crucible experiments on simultaneous dissolution of UO_2 and ZrO_2 by molten Zry at 2100 and 2200 °C have been carried out successfully. The kinetics of the material interactions in the tests with duration of isothermal annealing at target temperatures from 100 to 600 s, were measured.

The frozen melts in each specimen contained 3 major phases: a dendritic ceramic $(U,Zr)O_{2-x}$ phase with a zoned microstructure, a Zr(O) alloy matrix phase that also occurred as inclusions between the ceramic zones, and a U(O) phase that occurred in low concentrations as inclusions in the ceramic and Zr(O)-matrix phases.

The WDX and phase-area analyses showed no statistically significant variation in the phase compositions or distributions at different locations within each specimen, indicating that the melts were reasonably homogeneous at the test temperature before cooling. This confirms strong convective stirring of the melt in the tests and enhances accuracy of the chemical analysis of the melt mean composition.

The results of melt composition measurement by two different methods of the quantitative image analysis and chemical analysis are in good correspondence. This confirms validity of the quantitative image analysis method, which allows independent determination of dissolution kinetics of each solid material (UO_2 and ZrO_2) during their simultaneous interactions with molten Zry. These data allow development and thorough validation of a new analytical model.

Such a model was developed by IBRAE in co-operation with JRC [82] on the base of the previously developed within CIT Project of the 4th Framework Programme [56] models for separate dissolution of UO_2 and ZrO_2 by molten Zry [49], [51]. The model considers interactions of solid materials with convectively stirred melt during the two stages: saturation and precipitation. The system of equations includes mass balances for three components (U, Zr, O) and flux matches at two solid/melt interfaces. The results of the RIAR tests concerning uranium content of melt and the dissolved volumes of solid UO_2 and ZrO_2 materials were consistently simulated with the new model without tuning of model parameters. Being implemented in the SVECHA code [73], this model was validated on the AEKI tests in more prototypic fuel rod geometry [83]; and it is suitable for implementation in other severe accident codes such as ICARE2.

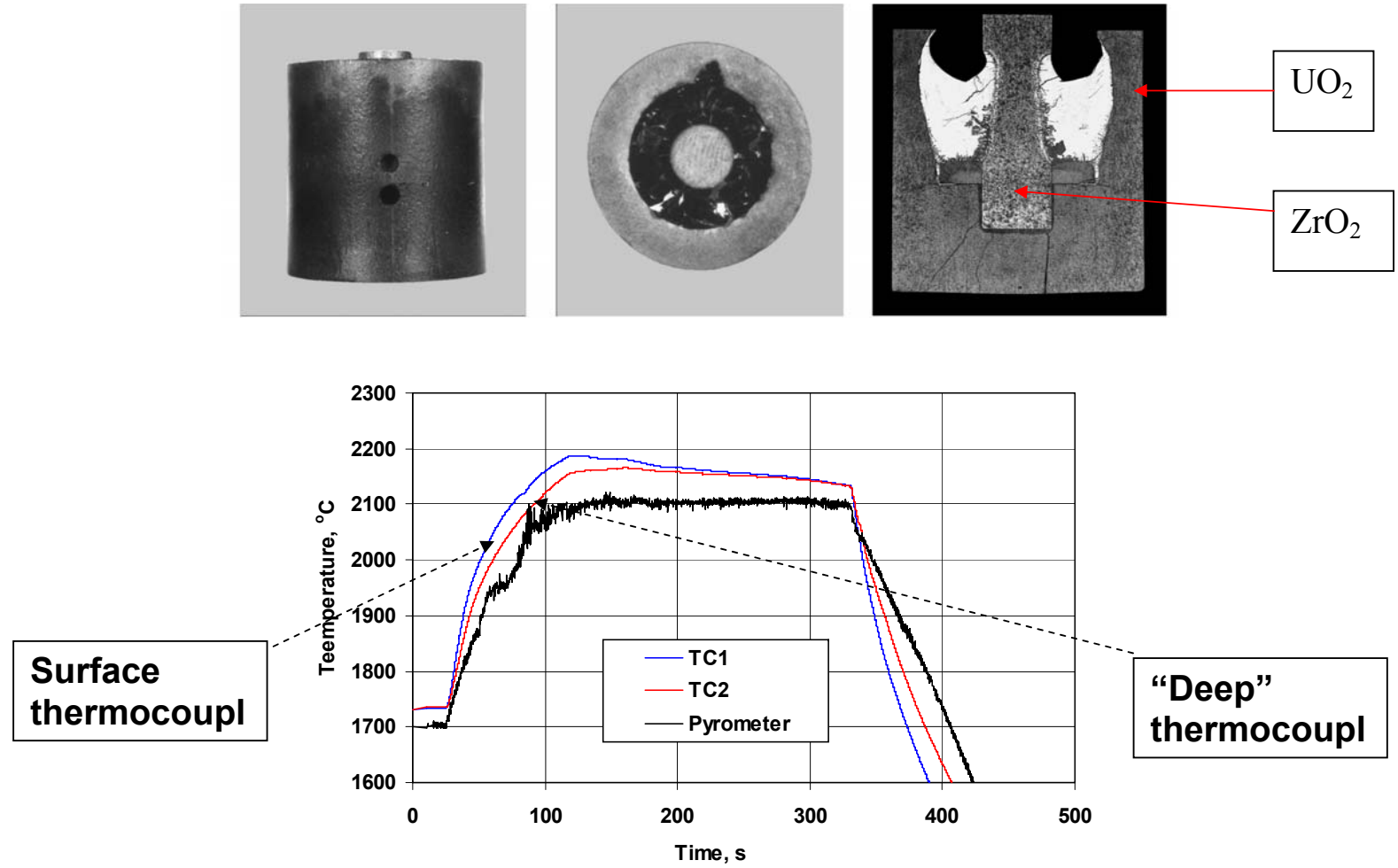

Figure 14: RIAR test with "deep" and surface thermocouples (2nd test series, T=2100 ^{0}C, t=200 s

2.4.5.2 Oxidation of Zr-O and U-Zr-O melts

The new model for Zr-O melt oxidation under conditions of convection stirring was developed by JRC in co-operation with IBRAE ([8], [9], [52], [73]) on the base of detailed analysis of post-test images of solidified Zr-O melts in the QUENCH-02 and 03 tests ([68], [69]). A close similarity with the melt appearance in the ZrO_2 crucible dissolution tests where oxide layer growth was accompanied with precipitation of ceramic particles in the corrosion (oxidation) stage of the tests was revealed. The model explains the formation of ceramic precipitates induced by the temperature difference between solid and liquid materials, and predicts continuous oxidation/precipitation process after attainment of the saturated state of the melt.

Furthermore, the model predicts a linear or close to linear time law for the rate of the ZrO_2 ceramic phase (oxide layer + precipitates) growth during Zr melt oxidation that corresponds to a much faster kinetics of Zr oxidation and hydrogen generation in comparison with the standard (parabolic) rate. Numerical calculations of the model allow quantitative interpretation of the vigorous melt oxidation and ZrO_2 phase precipitation observed in the QUENCH tests, Figure 15. The model was validated against new FZK tests on ZrO_2 crucible interactions with molten Zry with a long-term oxidation (or corrosion) stage ([10], [52]), specially designed for verification of the new model predictions.

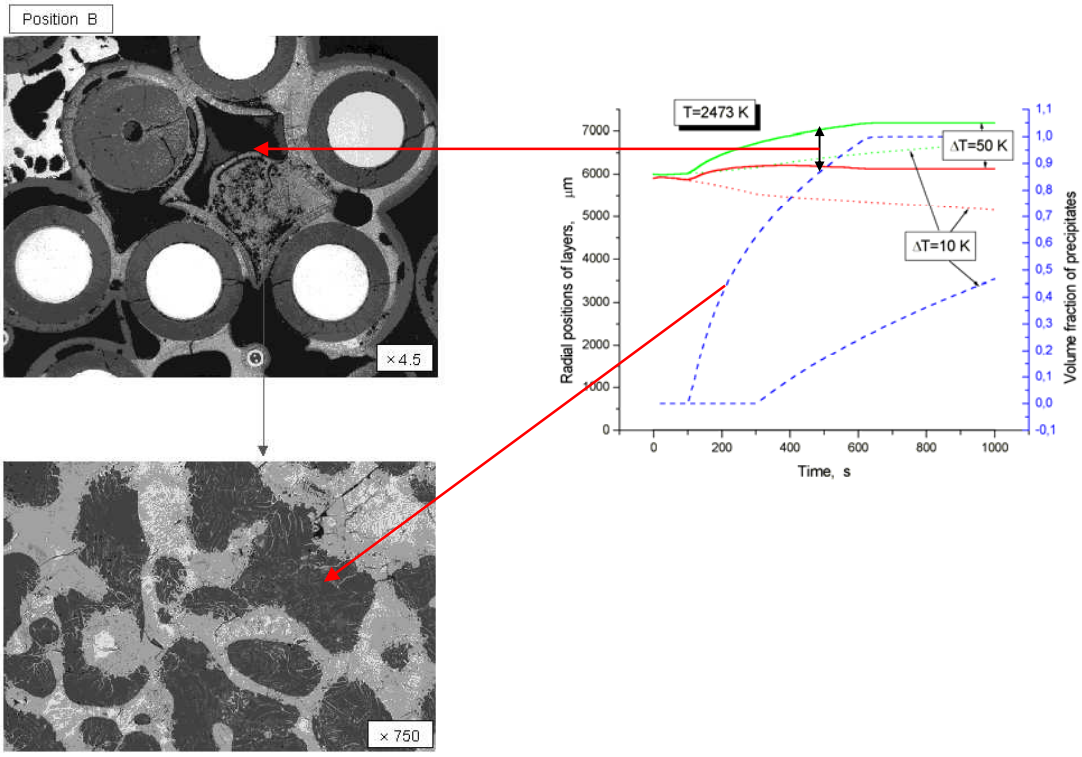

`

Figure 15: Simulation by the new model of molten pool oxidation observed in cross section Q-02-5 at elevation 0.883 m of the QUENCH-02 test bundle (red arrows indicate the oxide phase forming peripheral crust and bulk precipitates) [9].

The new model was further generalized for calculation of the ternary U-Zr-O melt oxidation. The main qualitative conclusion is that the enhanced kinetics of melt oxidation and hydrogen generation under non-equilibrium conditions is characterized and controlled by the temperature gradient between the solid and liquid phases; this was confirmed also for the ternary system. Numerical calculations with this model allowed the quantitative interpretation

of the strong melt oxidation and the $(U,Zr)O_{2-x}$ phase precipitation as these were observed in the CORA tests, Figure 16.

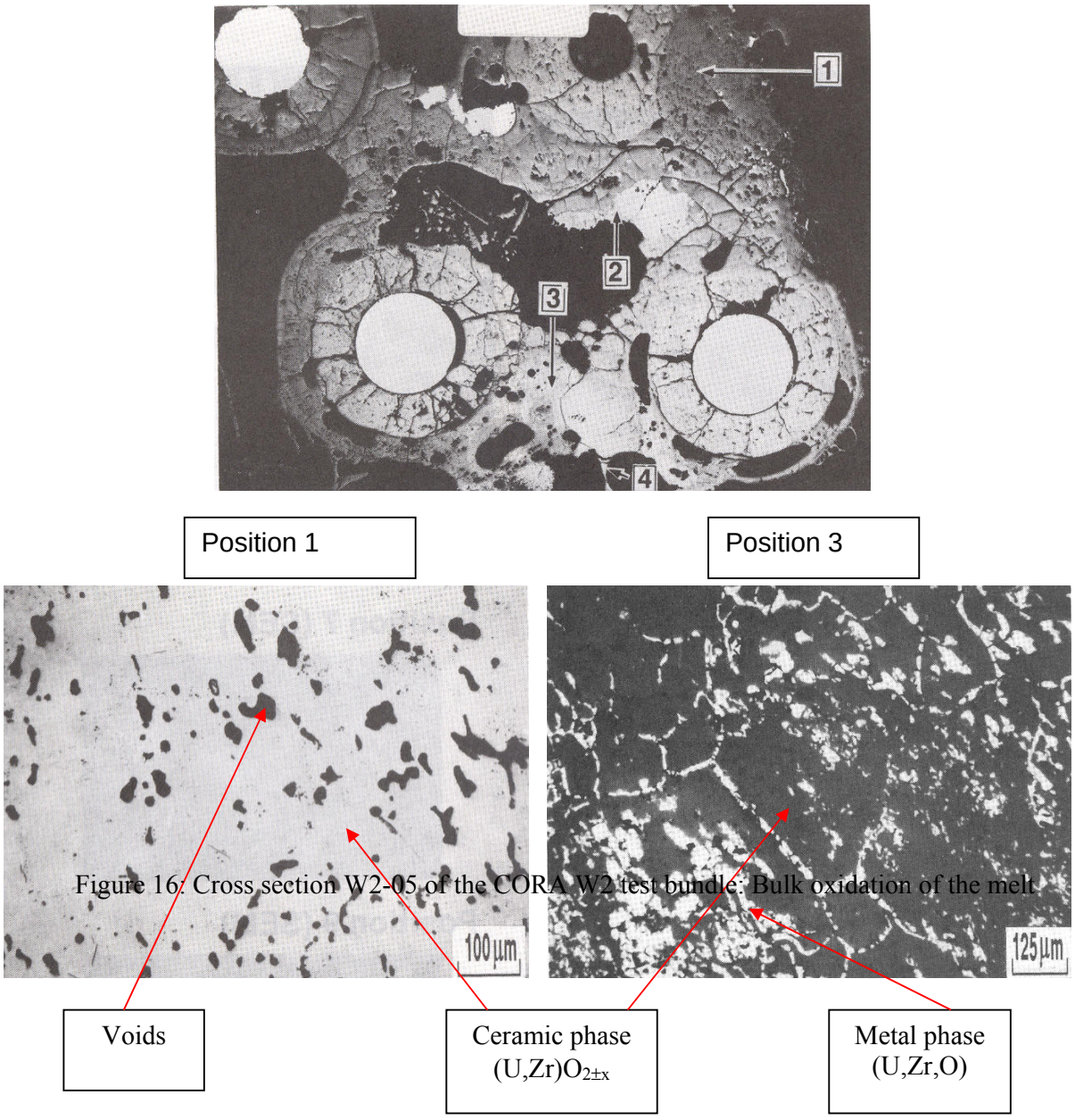

Figure 16: Cross section W2-05 of the CORA W2 test bundle: Bulk oxidation of the melt

2.5 Molten Pool Phase

As mentioned above, the molten pool is probably formed at 15180 s. At this moment, a strong in2.5rease in the gas temperatures in the circuit is detected and soon after a strong increase in the OLAM signal occurred at 15200 s. It can be concluded that the latter is mainly due to the flow rate peak after the flow area reduction due to the molten pool formation.

2.5.1 Experimental Findings

In the molten pool phase, the following events caused by material relocation were detected:

15700 seconds:

Increase of the shroud temperature at 0.4 m and 0.5 m

16000/16200 seconds:

Increase of the shroud temperature at 0.2 m and 0.3 m

17200 seconds:

Decrease of the shroud temperature at 0.8 m
Increase of the shroud temperature at 0.3 m and 0.6 m

17600 seconds:
Decrease of the shroud temperature at 0.6 m
Increase of the shroud temperature at 0.3 m

17800 seconds:

Increase of the shroud temperature at 0.8 m

These events indicate that several local relocation processes occurred correlated with aerosol release in the circuit detected by OLAM.

After the material relocation at 15700 s and at 16000/16200 s the location above the lower grid plate as well as the extent of the molten pool were stabilised. This stable phase existed during the following 1000 s until at 17200 s a material relocation from 0.8 m took place. It can be assumed that this relocated material was initially accumulated upon the upper grid plate located at 0.749 m. Further material was relocated from the upper half of the bundle to the molten pool at 17600 s and 17800 s.

Non-destructive and destructive post-test examinations of the bundle showed that a central zone of the bundle at the elevation of molten pool (between 0.155 m and 0. 255 m) was completely occupied by the ceramic corium. At the periphery a crust structure with thickness ≈ 0.003-0.005 m was formed.

In Figure 17 and Figure 18, the cuts through the molten pool show that the frozen ceramic melt is rather homogeneous. The peripheral corium is less porous with grains

elongated in the radial direction. The atomic composition of the corium determined by EPMA scanning is similar in the central and peripheral zones and approximately corresponds to $(U_{0.51}Zr_{0.48}Fe_{0.03})O_{2\pm x}$ (or on average 60 weight (wt) % of U, 20 wt % of Zr and 20 wt % of O [16]) in a $(U,Zr)O_2$-type lattice. Microanalyses confirmed that the composition of this phase was rather homogeneous in the molten pool zone, axially and radially.

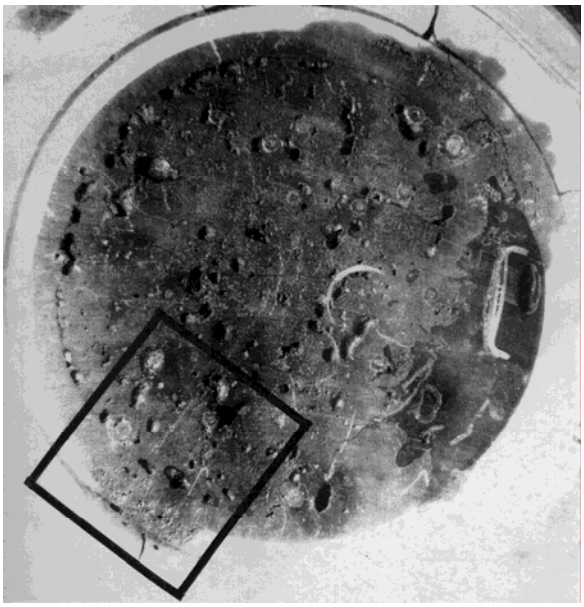

Figure 17: Observation of cut at 0.236 m

Figure 18: Position of line L3 in cut at 0.236 m

There are a number of impurities including iron oxides [84] but the small quantity of iron in the FPT0 bundle (0.7 wt %) limits the iron oxide content of the ceramic melt to the small values measured (0.5 to 1 wt % in the matrix and 2 wt % between grain boundaries).

According to Reference [84], such small amounts of iron oxide would have a negligible influence on the ceramic liquidus temperature and on grain boundary fluidity, even if the solidus temperature at the grain boundary were much reduced. The small effect on fluidity is postulated because the amount of liquid phase in the grain boundary is very small. In contrast to FPT0, some researchers thought that, in the TMI-2 accident, the much higher iron content of the TMI-2 core (4.3 wt %) possibly leads to fluid grain boundaries and sand-like movement in the most part solidified melt [84].

The UO_2-ZrO_2 phase diagram in Figure 19 indicates a minimum melting temperature of about 2800 K whereas the measurements of similar samples from FPT1 corium by indicate a 1.5% lower value of 2760 K [85]. A small reduction of the melting point can be apparently associated with influence of iron and/or with fuel irradiation effect.

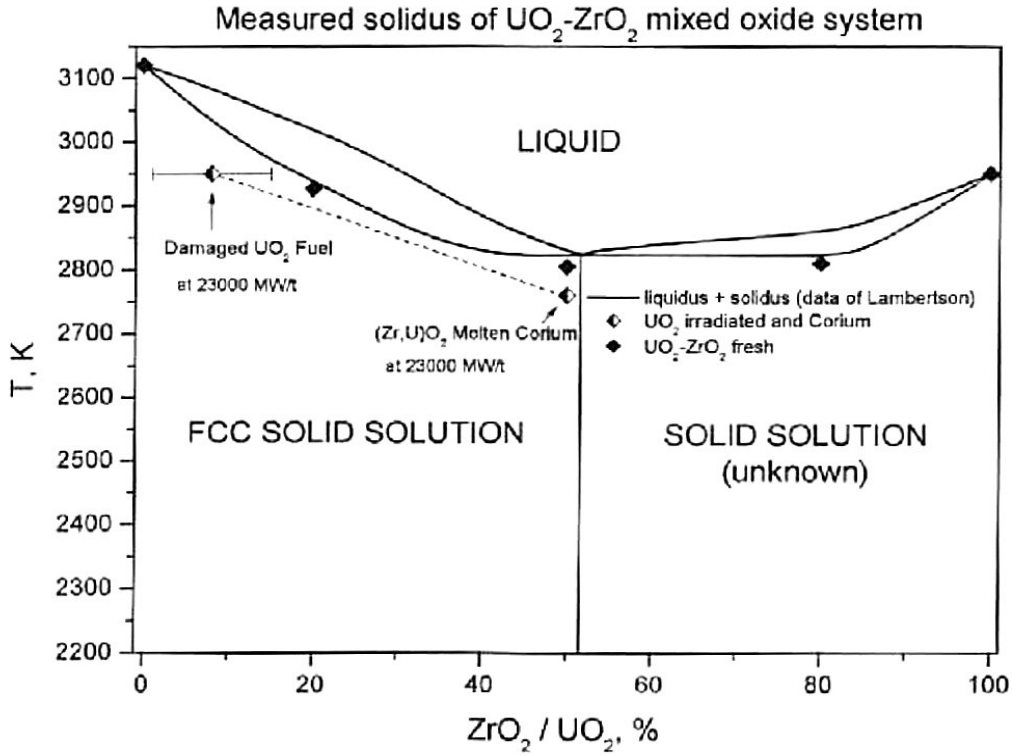

Figure 19: Binary Phase Diagram

At 18080 s the so-called final event occurred at which the shroud temperatures at 0.3 m, 0.4 m and 0.5 m significantly increases and decreases at 0.6 m. The inner shroud temperatures behaviour at 0.2 m, 0.4 m 0.5 m was similar. The aerosol release was enhanced (OLAM) as well as significant release of volatile fission products and control rod material (thermal gradient tube, filters, impactors and gas capsules) was detected as well as the power of the driver core increased by 6%. The post-test gamma scanning showed that below 0.01 m Ag is still present.

The tomographs registered after the tests indicate that a strong interaction between the molten pool and the shroud occurred at bundle elevations of 0.268 m, 0.250 m and 0.243 m. At the 0.172 m and 0.149 m levels, the attack of the shroud by molten corium was significantly less; however, at 0.172 m the hafnium content of the corium determined by ICP-MS was 0.5 %wt.

2.5.2 Status of the molten pool models

Degradation and molten pool formation are not reproduced in calculations considering the «standard» melting point of UO_2 (3110 K). For this reason, the default value of the temperature criterion in the codes for the relocation of core materials is 2800 K, corresponding to liquefaction of the ceramic phase mixture at the eutectic point in the UO_2-ZrO_2 phase diagram. Nevertheless, poor representations of the observed relocation of core debris in the FPT0 test are produced by the codes when this default criterion is used. Much better representations of relocation are obtained in code predictions by artificially reducing the "melting point" of fuel to 2500-2600 K to simulate the effects of non-equilibrium material interactions in the Zr-U-O system. Such a "trick" is needed to obtain an adequate simulation of both: i) the thermal evolutions in the bundle and shroud, ii) and the final degradation state of bundle.

However, these changes in the temperature criterion for the core material liquefaction and relocation are not substantiated with the equilibrium phase diagrams for the system. In

such a situation, a mechanistic consideration of the effect of non-equilibrium material interactions in the Zr-U-O system becomes especially important, since it allows physically grounded interpretation of the FPT0 test observations.

Indeed, additional analysis of the model for Zr-O melt oxidation (discussed above in section 3.4.4.2) shows that dissolution of the oxide layer by the melt under non-equilibrium conditions characterised by the temperature difference between solid and liquid phases, can proceed after attainment of the melt saturation. This model prediction was successfully confirmed by the new FZK tests, in which such dissolution behaviour at a late stage of crucible-melt interactions was investigated ([52], [10]). The important model prediction deduced for the binary Zr-O system concerning enhanced dissolution of the ceramic phase by saturated melts under non-equilibrium conditions can also be extended to the case of UO_2 dissolution. It was anticipated, that dissolution of UO_2 by the melt could be strongly increased under conditions of different temperatures in the fuel pellet and surrounding U-Zr-O melt. In this case, fuel dissolution is not anymore restricted by the melt saturation limit and actively proceeds in the oversaturated melt. This process (along with the melt oxidation by steam), leads to the enhanced over-saturation of the melt and to an increased rate of $(U,Zr)O_{2-x}$ ceramic phase precipitation. Therefore, a relatively quick transformation of UO_2 phase into the mixed $(U,Zr)O_{2-x}$ ceramic phase (owing to dissolution and precipitation) can be predicted by this mechanism.

Currently the model is extended to the general case considering temperature difference between the melt and two solid phases (pellet and peripheral oxide layer surrounding melt) in the course of their non-equilibrium interactions, therefore, it allows self-consistent treatment of UO_2 dissolution and melts oxidation accompanied with growth of the peripheral ceramic layer (crust) and bulk ceramic precipitates [82].

Being applied to the conditions of the FP tests [11] the model allows interpretation of the post-test microstructure observations of the molten pool in the lower zone of the FPT0 bundle. From the model calculations one can deduce that the observed homogeneous corium microstructure can be explained by precipitation of mixed ceramic $(U,Zr)O_{2-x}$ phase which accompanies the growth of the peripheral oxide crust (with a similar to central corium composition). This occurs in the course of enhanced dissolution of fuel rods by (over)saturated melt and simultaneous vigorous melt oxidation in the molten pool at relatively low temperature (2500-2600 K), if non-equilibrium conditions characterised by temperature difference between solid and liquid phases are sustained, Figure 20. The possible reasons for such non-equilibrium conditions in FP tests were analysed. An estimated amount of hydrogen generated during the molten pool stage in the course of such an oxidation/precipitation process is in a reasonable agreement with measurements.

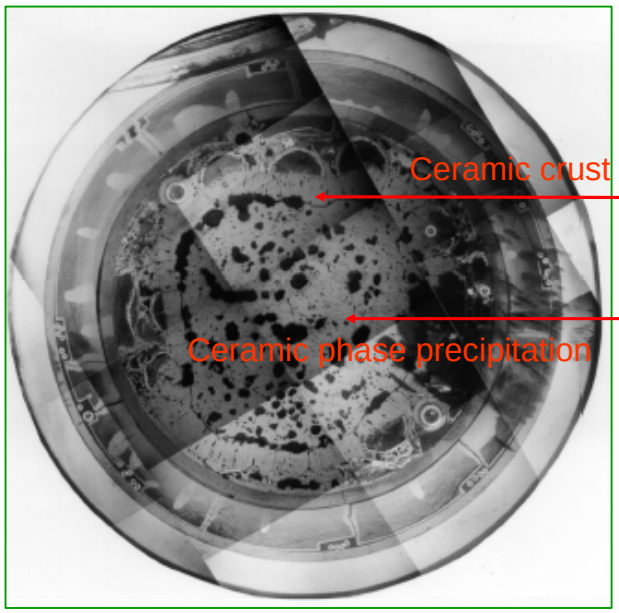

Post-test macrograph of $(U,Zr)O_2$ ceramic corium (molten pool)

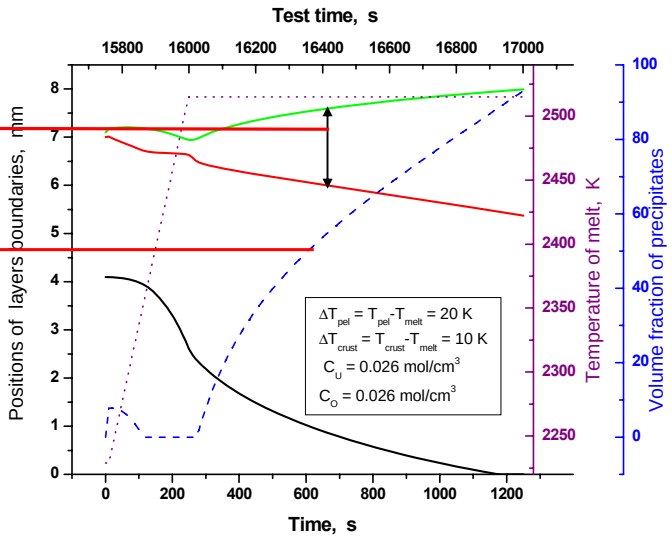

Evolution of molten pool layers during transient

Figure 20: Conversion of large molten pool into ceramic phase at T < 2300°C due to oxidation/dissolution [11].

3 Code Analyses

3.1 Bundle Behaviour

3.1.1 Synthesis of the ATHLET-CD and ICARE2 results

In the following sections, the code simulation results are compared with the measured data. At first, some details concerning the bundle power and on the modelling of the shroud are given because the interplay of the heat source and the main heat sink influences dominantly the thermal bundle behaviour. Then, the most important physical quantities are compared: the bundle temperatures, the mass of produced hydrogen and the axial mass distribution of the degraded bundle.

3.1.1.1 Bundle heating power

During the test, the bundle power cannot be directly measured; it is evaluated as a ratio of the measured reactor power and a coupling factor. The latter is determined from independent measurements at low power levels of the driving reactor, which contains the instrumented intact test bundle. In case of fuel relocation, the calculated with this factor nominal bundle power cannot be regarded as representative because the independent measurements refer to intact bundle geometry and the reactor power is not very sensitive to the mass distribution in the bundle.

It is essential to distinguish the nominal and the effective bundle power. The analysts have defined the nominal bundle power together with its axial distribution and the neutronic shielding coefficients. The effective bundle power is calculated by the codes using the above-mentioned data and the actual axial distribution of fuel in the bundle at each time step.

Figure 21 shows that the nominal bundle powers used in the calculations and in the FPT0 test are identical up to 12000 s of process time. After this moment, the nominal power defined in the calculations is somewhat lower than the nominal power measured during the test. This is justified because after control rod failure and beginning of materials relocations the value of coupling factor is known only with a considerable uncertainty.

The evolution of nominal bundle power in the test is monotonic. Before the beginning of massive fuel relocation, i.e. before 15000 s there are three time intervals (plateaus) when the power is kept constant; these nominal power values are 1.4, 3.3 and 24.2 kW, respectively. The first two plateaus correspond to the calibration phase. During the third plateau, the bundle temperatures are stabilized. Thereafter at 14500 s the power is raised with a rate of 0.3 - 0.4 kW/min leading to massive fuel degradation. The shutdown time of driver core is at 18138 s [16] the nuclear fission power drops from the maximum value of 50.4 kW to zero in several seconds and the heat loss to shroud and the steam inflow cool the degraded bundle in several tens of minutes.

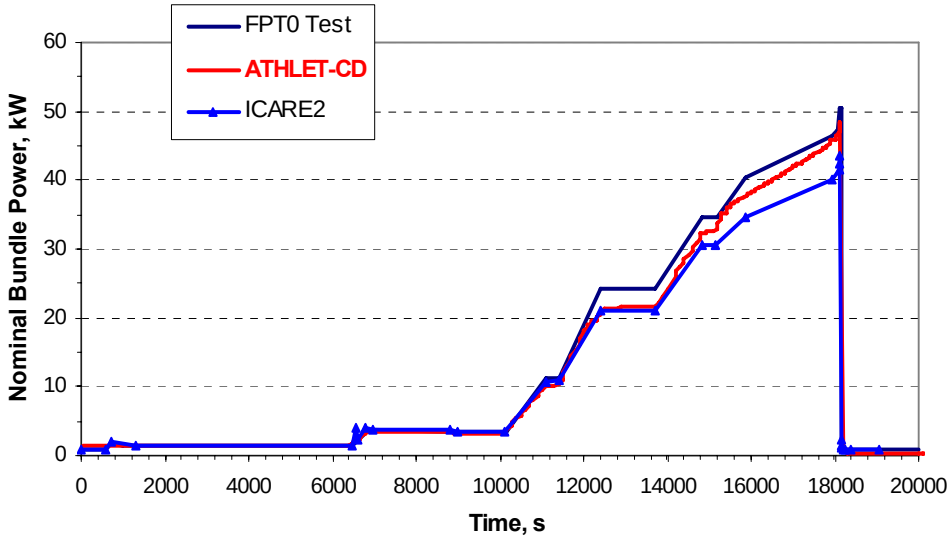

Figure 21: Comparison of nominal bundle powers used in the post-test calculations test by ICARE2 and ATHLET-CD

Figure 22 illustrates the difference between the nominal and effective bundle power used in ATHLET-CD. It can be seen that after 15000 s the massive material relocations to lower bundle elevations, where the power peaking factors are smaller compared to those than in the middle of bundle, lead to a substantial decreasing of the effective power.

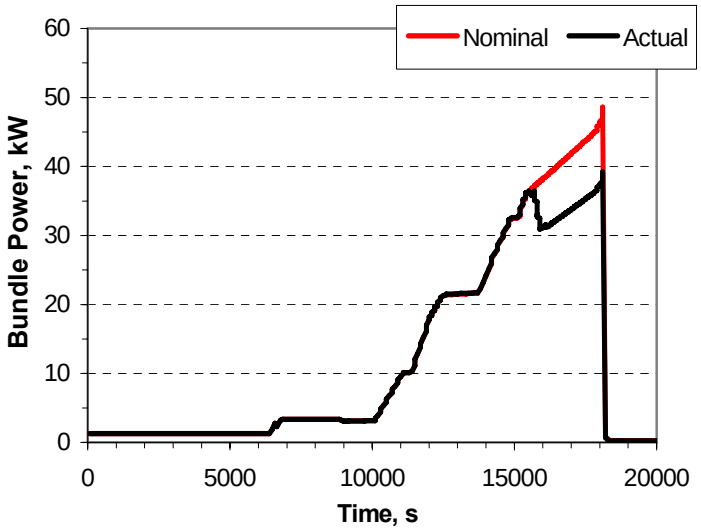

Figure 22: Comparison of nominal and effective bundle powers used in the ATHLET-CD post-test calculation

3.1.1.2 Oxidation power and heat loss to gas

Additionally to the nuclear heating power, the oxidation of Zircaloy cladding by steam - being a strongly exothermic chemical reaction - also contributes to the heating of bundle. Figure 23 shows that the time evolutions of the oxidation power calculated by the ICARE2 and ATHLET-CD codes are, in principle, identical. There are two oxidation periods, one between 12000 s and 12500 s and the other between 14000 s and 17000 s, respectively. Before 12000 s, the intact bundle was pre-oxidized and between 12500 s and 14000 s, the oxidation rate is very low. During the first oxidation period the contribution of the total oxidation power to the bundle power is significant (compare Figure 21 and Figure 23, left plot). It should noticed, that

the maximum oxidation power calculated with ICARE2 is higher by about a factor of two compared to ATHLET-CD result (50 kW versus 26 kW).

The right plot in Figure 23 shows the calculated heat loss to gas, i.e. the heat transferred by convective heat exchange to the gas, which flows through the bundle. The time evolution of this heat loss depends mainly on the steam mass flow rate at the bundle inlet (see Figure 24) and gas temperature distribution. The latter is approximately proportional to the bundle power profile.

During the first oxidation period, the heat loss to gas calculated with ICARE2 is significantly lower than that obtained with ATHLET-CD. This means that the gas removes less heat from the bundle and the cladding temperatures can be somewhat higher than in the ATHLET-CD calculation. Furthermore, the higher cladding temperatures in the ICARE2 calculation may explain the significant higher oxidation power compared to that obtained in the ATHLET-CD calculation (see Figure 23, left plot).

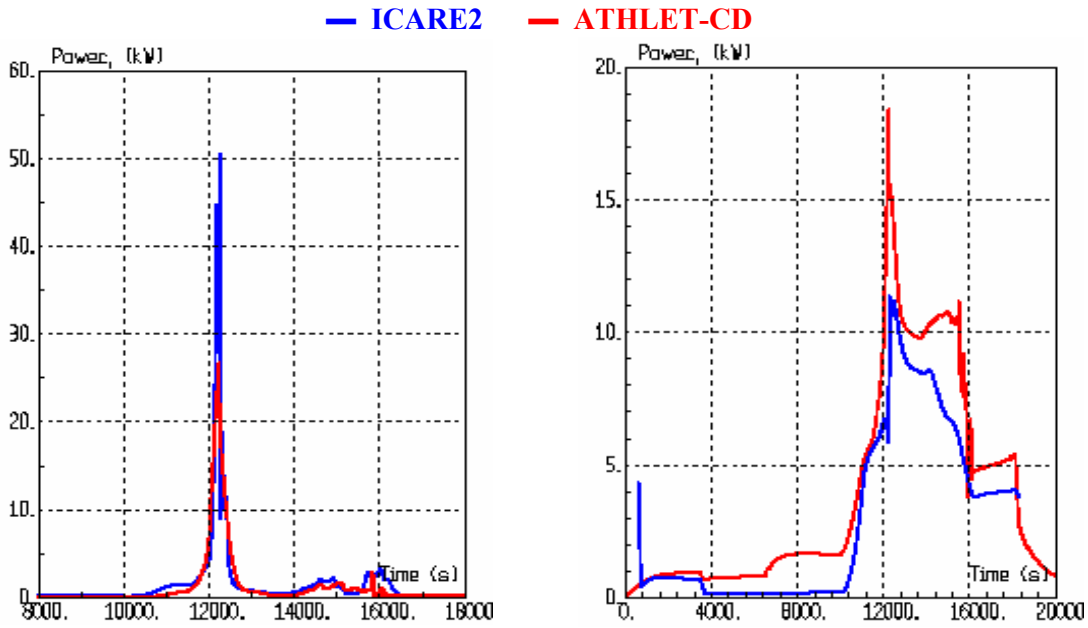

Oxidation power Heat loss to gas

Figure 23: Calculated oxidation power and heat loss to gas as a function of time

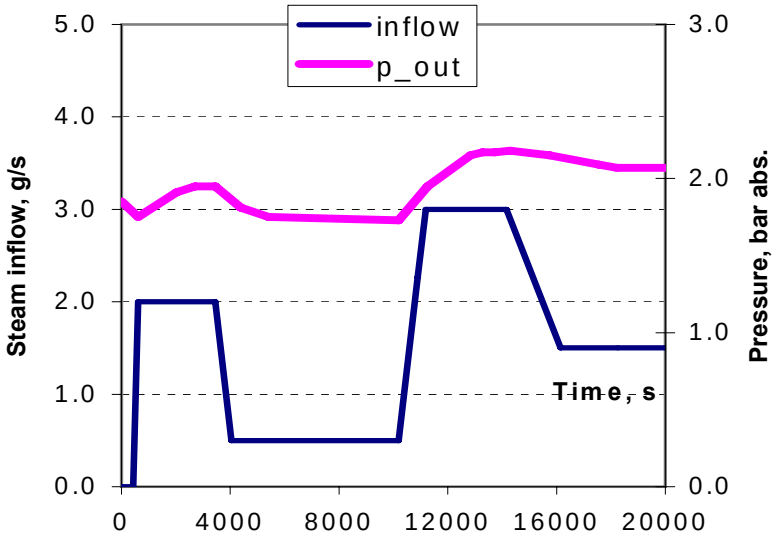

Figure 24: Steam flow injected at the bundle inlet and the system pressure as a function of time.

3.1.1.3 Shroud modelling

After the calibration period and especially during massive bundle degradation, up to 90 % of bundle power is lost through the most external surface of multi-layered shroud to pressurized water flow circulating in the cooling loop. The peculiarity of shroud is that there are two narrow, steam-filled gaps between the inner and outer zirconia layers, and between the outer zirconia layer and pressure tube, see Figure 25b. The modelling of the gap behaviour fairly affects the shroud temperatures and heat losses.

Overall, the ICARE2 and ATHLET-CD codes represent the shroud with the same geometry and material properties, however, the heat transfer through these gaps are modelled in a different ways. In ATHLET-CD, heat transfer coefficients as a function of time are used whereas in ICARE2 temperature-dependent heat conductivities are applied.

To compare these two approaches, the heat transfer coefficients of ATHLET-CD calculation were converted to effective heat conductivities as a function of temperature by using the temporal dependence of gap width and the average gas temperature in the gap, which was assumed equal to the averaged temperatures of the two cylindrical shroud layers surrounding the gaps.

Furthermore, for additional comparison, the thermal radiation between two parallel plates with infinitely large area and small temperature difference between them was calculated as $\alpha_r = 4\varepsilon\sigma T^3$. Here α_r is the radiative heat transfer coefficient, W/(m^2·K), ε is the thermal emission coefficient of the surface of solid phase (grey-body), dimensionless; and σ is the Stefan-Boltzmann constant, $5.67 \cdot 10^{-8}$ W/(m^2·K^4); $T+dT$ and T are the plate temperatures, K.

Figure 25a shows that below 1000 K, the effective heat conductivity is about the same in the ICARE2 and ATHLET-CD calculations whereas above 1000 K in ATHLET-CD a value about 30 % higher was used compared to ICARE2. It can also be seen that between 1000 K and 1500 K the effective heat conductivity of ICARE2 correspond to heat transfer by thermal radiation through the narrow steam filled-gaps.

Figure 26 shows that after 10000 s, i.e. after the calibration period the calculated width of the inner and outer steam-filled gap remarkably decreases as the bundle heats up. ICARE2 and ATHLET-CD calculate about the same evolution of gap width, generally, in this period the gap width is inversely proportional to the temperature of neighbouring shroud layers. In the ICARE2 calculation, the outer shroud gap closed at about 16000 s; it was modelled by temperature–independent effective heat conductivity. In the ATHLET-CD calculation, the gap closure did not happen.

In FPT0, after 13000 s, during the bundle degradation phase the thermal gradient in the outer shroud reaches high values (up to – 220 K/m) and the presence of shroud gaps is necessary to prevent the build-up of thermo-mechanical stresses, which could destroy the shroud. Both calculations show that, after shutdown in the cool-down period, the gaps gradually take back their original width.

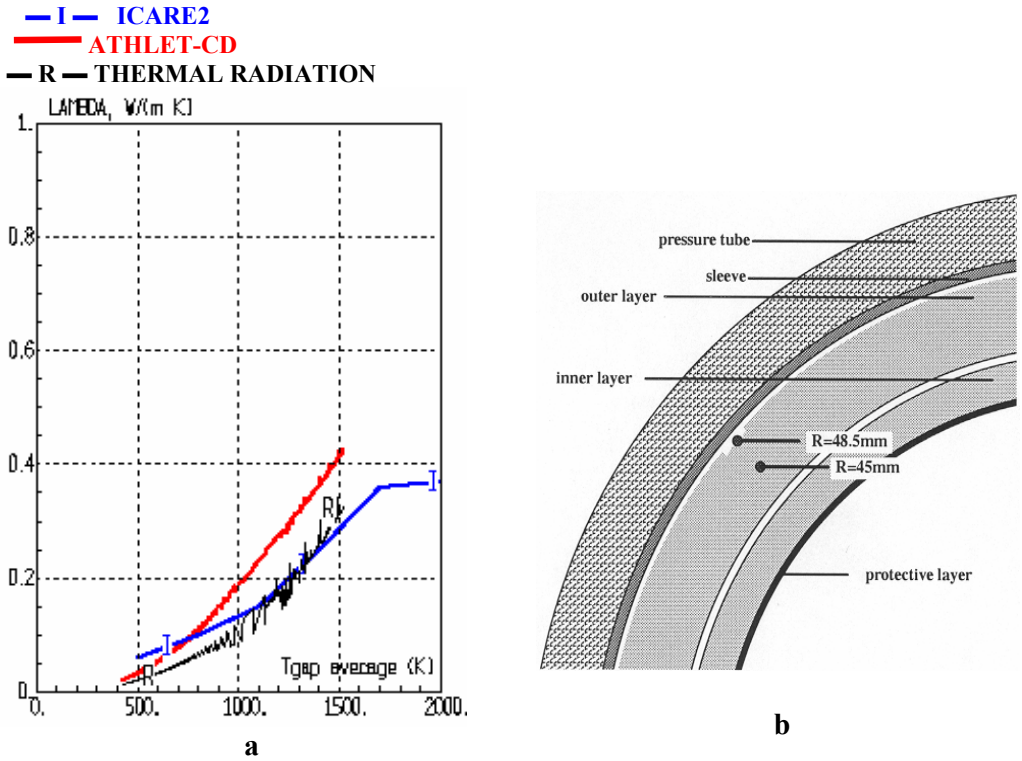

Figure 25: (a) Effective heat conductivities as a function of temperature. (b) Horizontal cut of the cylindrical shroud

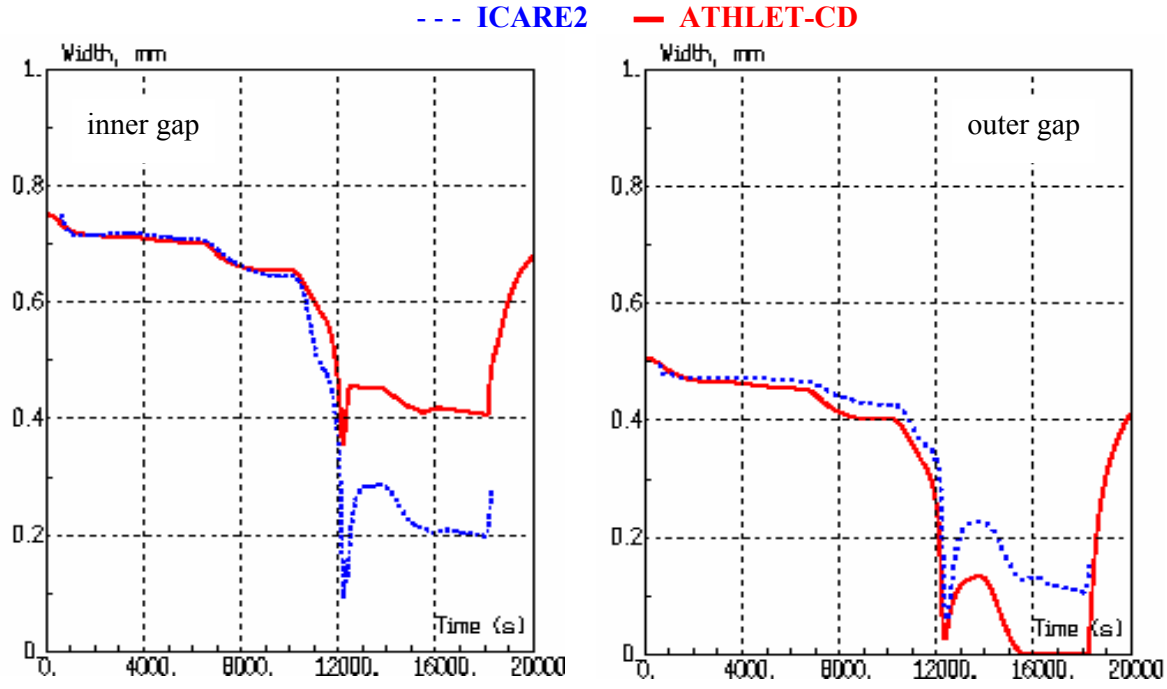

Figure 26: The calculated width of the steam-filled gaps in the shroud as a function of time at axial elevation of 0.8 m

3.1.1.4 Bundle temperatures

In Figure 27 and Figure 28, the measured and calculated bundle temperatures at various axial elevations as a function of time are compared. The agreement with the FPT0 test results is good. Generally, the evolution of temperatures follows the shape of the total (nuclear and oxidation) bundle power. In the calibration period (between 0 s and 10000 s), the temperatures increase during power ramps and stabilize during the power plateaus. At 10000 s, the stabilized fuel temperature is between 1000 K and 1200 K depending on bundle elevation.

At higher elevations at 0.7 m and to 0.8 m both codes predicts the temperature escalation at about 12000 s. This rapid temperature increase at these elevations lasts about 60 s and the peak fuel temperature is about 2700 K (see Figure 27, upper plots). Shortly after the temperature escalation in the upper bundle regions, at the lower elevations 0.3 m and 0.4 m the temperature escalation occurs but with a lower heat-up rate of about 1 K/s and a lower peak fuel temperature at about 2000 K.

ATHLET-CD calculation predicts the first early fuel relocation of metallic melt at the elevation of 0.7 m at 12333 s whereas in the test it occurs at 12050 s. The total relocated mass of metallic melt in the first oxidation period is 0.225 kg.

At 13380 s begins the last power ramp leading to massive fuel degradation. At about 15000 s, the fuel temperature reaches about 2600 K until shutdown time (18138 s). In this period, some thermocouples fail and the massive relocation of degraded fuel rod material occurs. Compared to the test results the massive fuel relocation is delayed in the ATHLET-CD, in the calculation it occurs at 15400 s and the mass of the axial zone at 0.5 and 0.6 m moves downwards. At some elevations, the fuel rod material is completely relocated. In the ATHLET-CD calculations, a complete disappearance of the mass of a component in a given mesh is indicated with a temperature drop to 273 K. During this last heat-up period, most part of the metallic components in the bundle are already oxidized - only near the bottom the bundle is still intact and the oxidation contributes slightly to the bundle power.

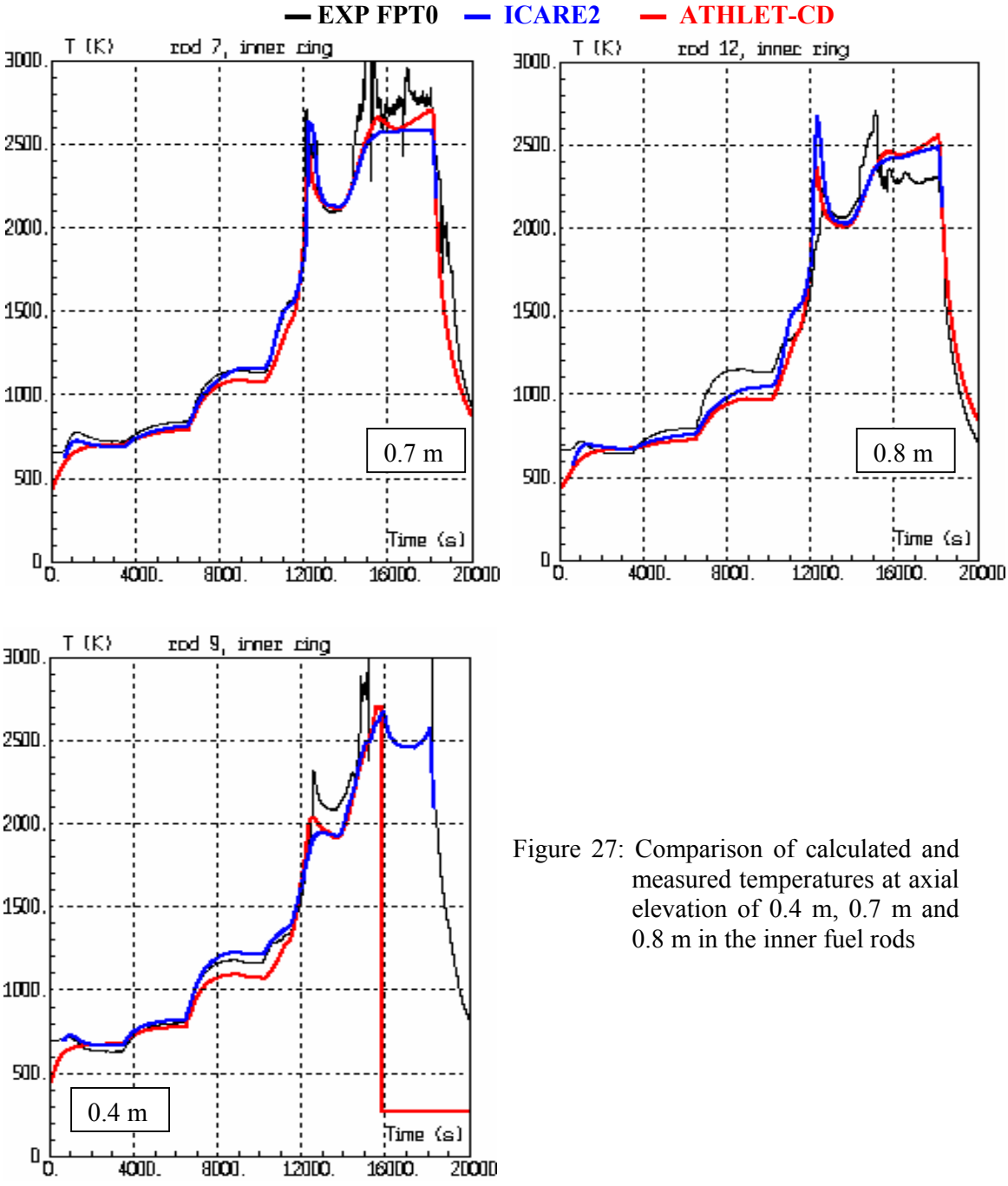

Figure 27: Comparison of calculated and measured temperatures at axial elevation of 0.4 m, 0.7 m and 0.8 m in the inner fuel rods

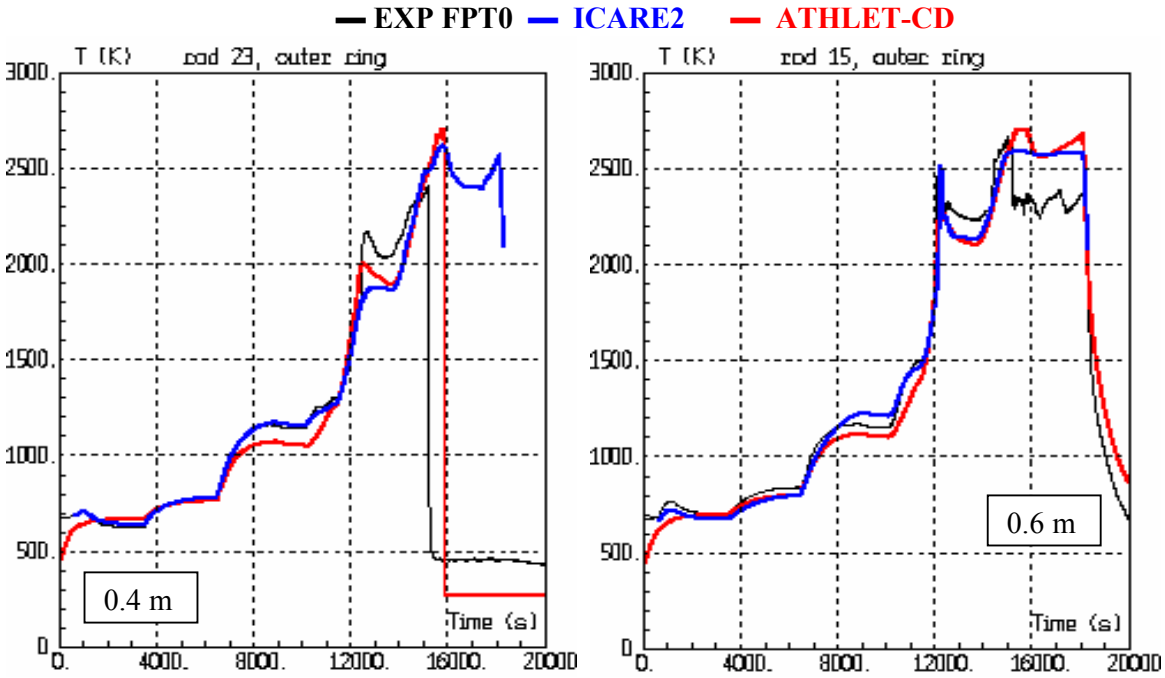

Figure 28: Comparison of calculated and measured temperatures at axial elevation of 0.4 m and 0.6 m in the outer fuel rods

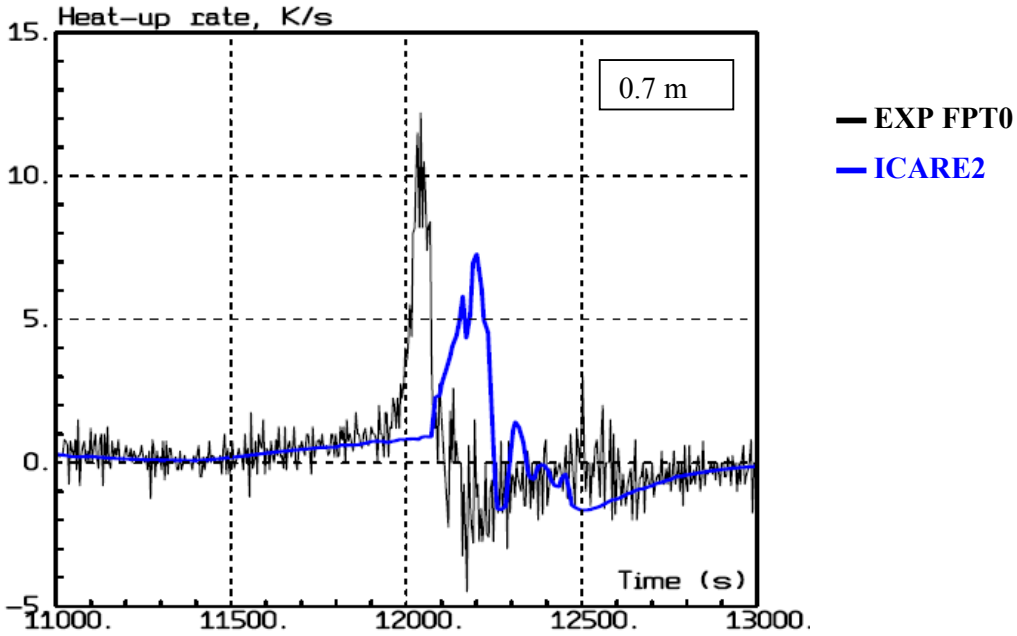

Figure 29: Heat-up rate of the fuel at axial elevation of 0.7 m in the first oxidation period

At about 12000 s in the test at the elevation of 0.7 m, the heat-up rate increases from 1 K/s to 12 K/s (upper limit), see Figure 29. At this moment, the fuel temperature is about 1800 K. This rapid heat-up is owing to oxidation runaway and lasts about 60 seconds and the fuel temperature attains about 2700 K. After that time, the heat-up rate became even negative because the metallic Zircaloy of the cladding is oxidized at this elevation or partly relocated downwards dissolved in the U-Zr-O melt. In the ICARE2 calculation, the maximum heat-up rate is significantly lower than the measured one and delayed by 200 s. The strong temperature

increase is caused by a phase transition at about 1800 K when the tetragonal-to-cubic transition in zirconia occurs [48], which increases of oxygen diffusion through this oxide scale. As already mention in Chapter 1.3.2, a new correlation was recommended, which takes into account this effect more exactly than Urbanic-Heidrick correlation used in ICARE2.

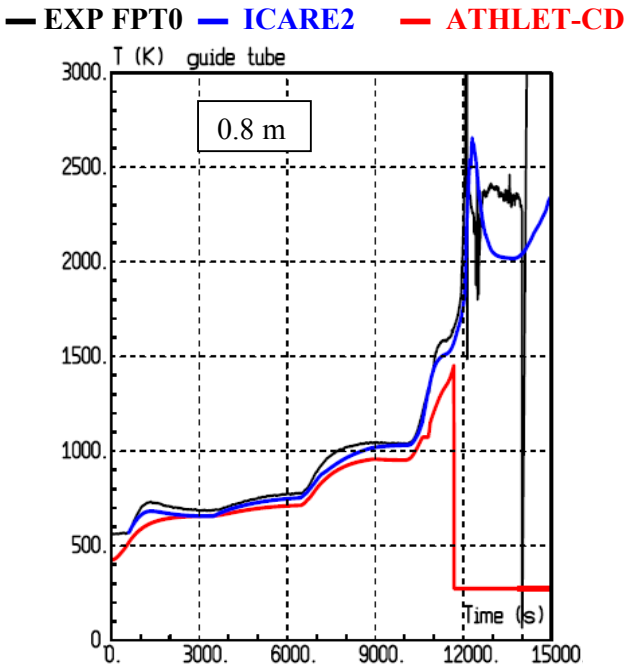

Figure 30: Comparison of calculated and measured temperatures of the guide tube of AIC absorber rod at axial elevation of 0.8 m

In the test, the first failure of a thermocouple attached on the guide tube occurs at the axial elevation of 0.8 m and at 12065 s during the temperature escalation, i.e. shortly after the onset of the temperature escalation at 12000 s. The first failure of guide tube in the ICARE2 calculation was at 11902 s at the elevation of 0.7 m. In the ATHLET-CD, calculation the first absorber melt formed above 0.7 m relocates at 11680 s (see Figure 30).

At the end of transient, the relocated AIC mass is about 0.5 kg in both calculations and in the FPT0 test as well. This corresponds to 85 % of the initial absorber material, which is relocated from the axial zone between 0.15 and 1.0 m.

The re-solidified mass of control rod material predicted by ATHET-CD at the end of the transient is 0.7 kg and it consists of 0.5 kg of AIC absorber, 0.12 kg of stainless steel and 0.091 kg of Zircaloy of the guide tube. Obviously, the relocation model does not take into account the evaporated mass. Therefore, a direct comparison of the mass profile of the control rod components with the measured data could not be made. This is also valid for the ICARE2 calculation, because the predicted relocated absorber mass is 0.5 kg. In the test, the total release of absorber materials from bundle is about 12 %, 9 % and 47 % of the initial bundle inventory (i.b.i.) for silver, indium and cadmium, respectively.

3.1.1.5 Hydrogen production

Figure 31 and Figure 32 compare the measured in FPT0 test and calculated by ICARE2 and ATHLET-CD hydrogen production rates in the first and second oxidation period, respectively. In the first oxidation period (between 12000 s and 12250 s), the kinetics is reproduced relatively well but with a delay of about 100 s. The maximum production rate is about 0.2 g/s or 0.1 moles H_2 per second while the steam mass flow rate at the bundle inlet (bottom) is 3.0 g/s (see Figure 24). In the calculations, more than 95 % of the produced hydrogen is due to Zircaloy oxidation, i.e. the steam is not completely consumed by the oxidation. During the whole transient, the steam mass flow rate is at least 1.2 g/s at bundle outlet and it is even higher inside the bundle. Partial steam starvation occurs; the minimum amount of steam in the gas flow is never less than 40 mol percents.

During the second oxidation period (between 14000 s and 18120 s), the maximum hydrogen production rate is about 0.02 g/s, i.e., it is lower by one order of magnitude compared to the first period. This is because most part of the bundle already oxidized during the first period; un-oxidized materials are only at the bundle bottom in form of intact fuel rod segments and not completely oxidized corium. Both in the FPT0 test and in the ICARE2 and ATHLET-CD calculations, the kinetics of H_2 production is significantly influenced by material relocation occurring intermittently in the lower part of bundle in this period.

For the total mass of hydrogen produced in the FPT0 test, ICARE2 and ATHLET-CD calculated 119 g and 108 g, respectively, whereas the measured value was 125 g. Figure 33 shows that the calculated hydrogen mass is underestimated by about 10-20 g in the first oxidation period lasting up to 14000 s. Later, in the second oxidation period the mass is overestimated by about 3.0-6.0 g. The calculated total hydrogen is well predicted taken into account the uncertainty (± 10 g) of the measurement. However, the underestimation of produced hydrogen mass in the first oxidation period suggests that the modelling of Zircaloy oxidation could be refined.

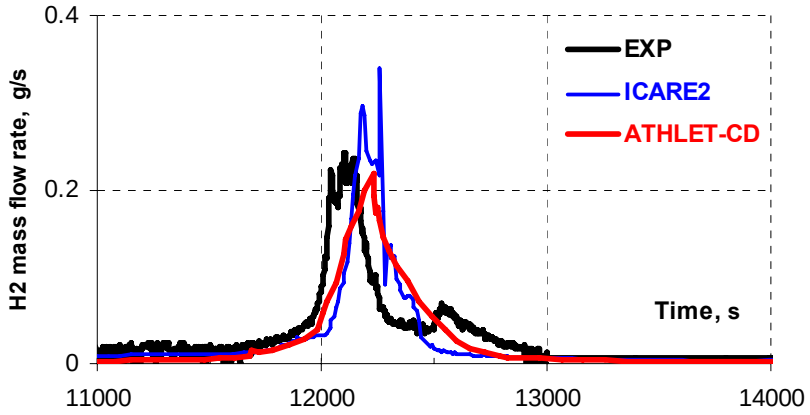

Figure 31: Comparison of the calculated and measured hydrogen production rates during the first oxidation period

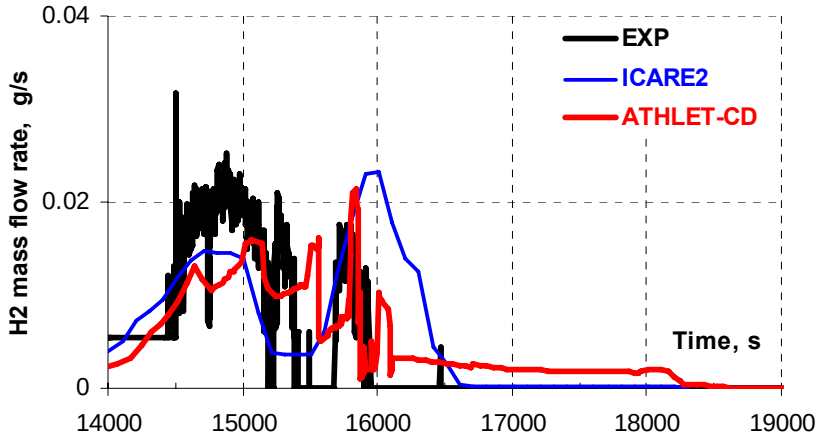

Figure 32: Comparison of the calculated and measured hydrogen generation rates during the second oxidation period

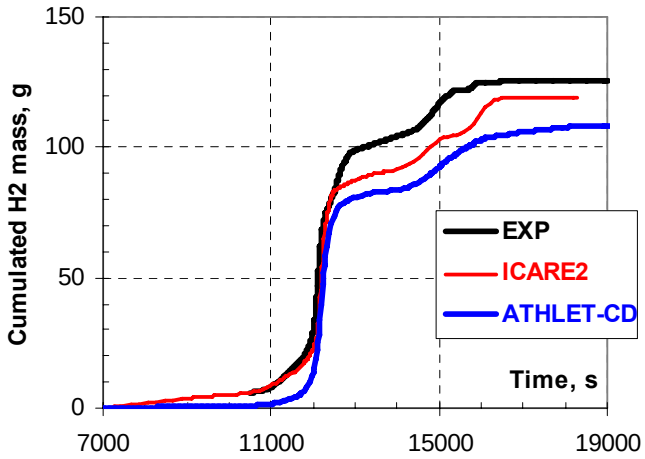

Figure 33: Total mass of produced hydrogen as a function of time.

3.1.1.6 Axial mass distribution

The material distribution in axial direction is characterized by the linear mass, which is the ratio of mass located in a given elevation zone and the axial length of this zone. After the test, it is measured by X-ray transmission tomography.

The final fuel mass distributions in the bundle are shown in Figure 34. It takes into account all kinds of materials in the bundle; the shroud materials are excluded. The horizontal dashed line represents the linear mass of intact active fuel, which initially is constant (10.4 kg/m) along the bundle. The vertical dotted lines show the position of spacer grids in the intact bundle according to FPT0 Data Book [43].

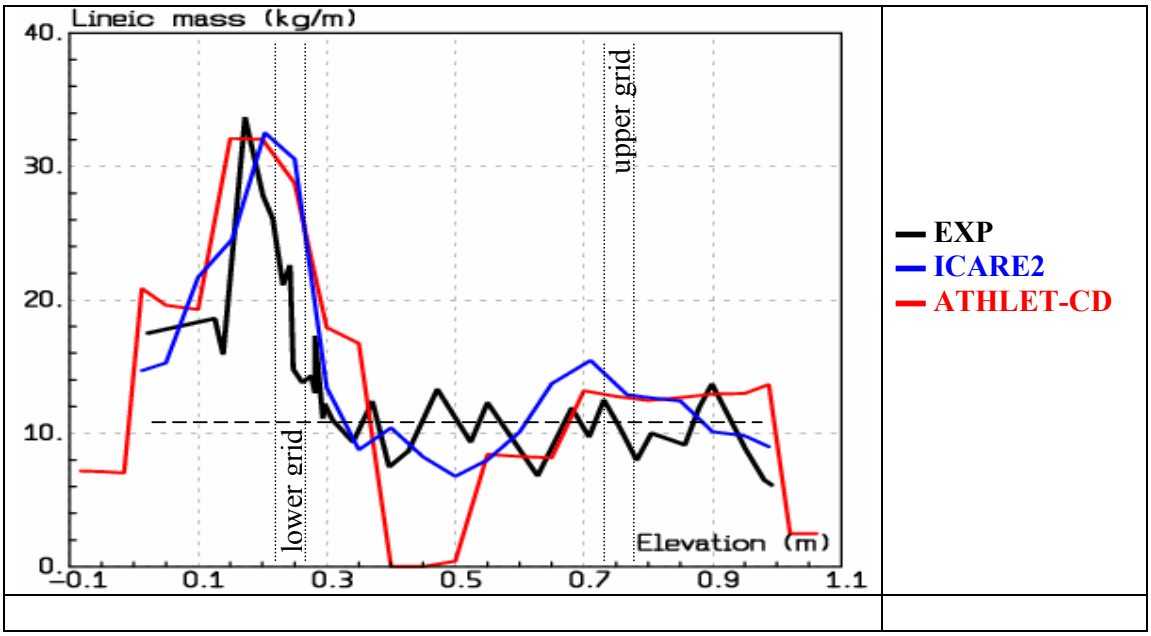

Figure 34: Comparison of final axial mass distributions

It can be seen that these materials, after relocating from above 0.40 m, are accumulated in the axial zone of 0.05-0.40 m. The ATHLET-CD and the ICARE2 calculations predicted that, between 0.30 and 0.40 m, the linear mass sharply increases and the upper boundary of accumulation zone is at 0.35 m and 0.30 m was, respectively. The comparison with the measured data show, that the sharp increase of the linear mass is shifted by 0.05 m to a lower location and the upper boundary of accumulation zone is at 0.30 m. The difference might be explained with the final event, which cannot be simulated with actual code versions.

The measurement showed that just above the accumulation zone (above 0.255 m) the bundle is partially empty; in the centre there is a small cavity (about 0.06 m height, 0.04 m diameter) surrounded by corium; the latter is located close to the shroud. Because ATHLET-CD predicts that all material between 0.4 m and 0.5 m is relocated downwards, a significant larger volume of the cavity is calculated (height 0.10 m, 0.074 m in diameter).

For the maximum value of linear mass (about 32 kg/m at 0.2 m) both codes calculated about the same value as in the experiment. This linear mass corresponds to a substantial (about 75%) blockage of the bundle cross-section by molten/re-solidified materials and eventually intact fuel rod remnants.

Using the initial and final total mass profile measured in the test and those calculated by the codes, the relocated mass was evaluated applying the same methodology described in [86]. The obtained values are the following: 2.4 kg (FPT0 test), 2.9 kg (ICARE2) and 3.8 kg (ATHLET-CD). It should be noted, that the measured mass profile (see Figure 34) was corrected by multiplying it by a constant (=1.13) in order to fulfil the overall mass balance, because otherwise the mass increase due to oxidation is not taken into account.

The greater relocated mass in the ATHLET-CD calculation compared to the measured one is attributed to the large cavity between 0.4 m to 0.5 m (see Figure 34). The calculated mass of molten ceramic materials (UO_2 and ZrO_2) is 2.4 kg and 3.1 kg in ICARE2 and ATHLET-CD, respectively. Considering that in the codes, the modelling of the ceramic melt formation is different as well as the complex interplay of the models is realised in a different way, these values still indicate a fair agreement.

3.2 Release of fission products and structure materials

3.2.1 Experimental Findings

Three different main periods of release were identified for most of the FP (see Figure 35) associated with fuel liquefaction and relocation:

- during the oxidation of the Zircaloy fuel claddings corresponding to early fuel melting, high fuel temperature (up to 2670 K) and high temperature ramps (between 5 up to 9 K/s above 1773 K [16]), high hydrogen release (the molar ratio H_2/H_2O was up to 80%),
- during the relocation phase
- during the shutdown (final event)

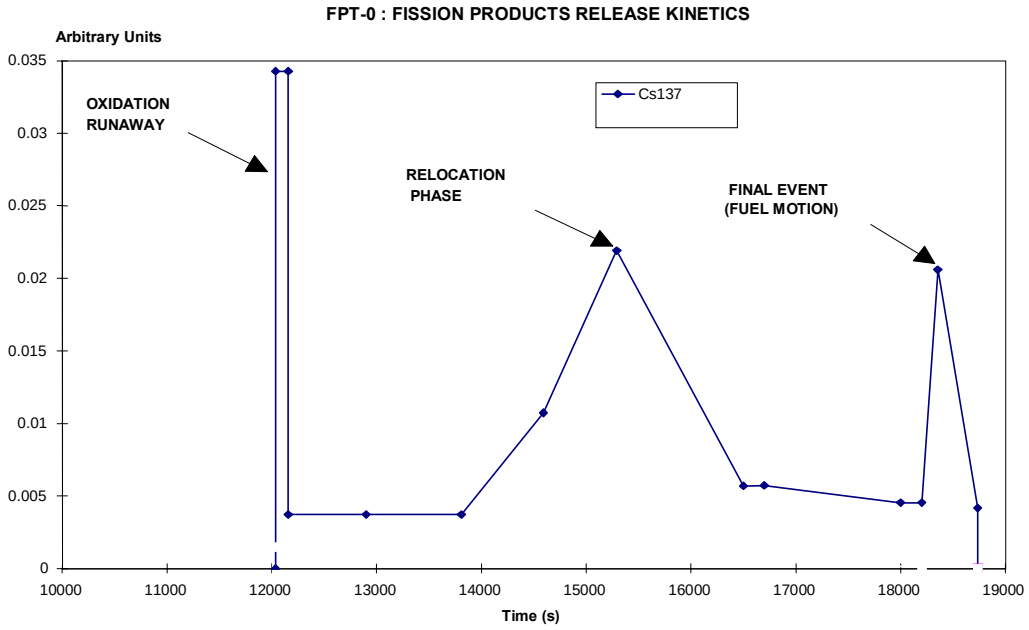

Figure 35: Cs flows transported through the primary circuit during the high temperature transient (degradation phase)

Three different categories of release were obtained, depending on the global release measured at the end of the experiment:
Rather high release volatile FP (Cs, I, Te, Mo, Sb, fission gases)
Rather low release (<3%) (Ba, La, Ru, Eu, Sr)
Very low release FP (Ce, Zr, U and actinides)

3.2.2 Results of the calculations

3.2.2.1 ATHLET-CD

In
Table 2 for some elements the measured data on FP release are compared with those obtained with ATHLET-CD. Both the measurement and ATHLET-CD calculation show that the high volatiles I, Cs and Te are almost completely released from the trace-irradiated fuel.

The calculation underestimates the release of the low volatile uranium by a factor of two. Relatively large differences between the calculated and measured data exist with respect to the release of control rod materials (up to a factor of 6). The uncertainties in the measurement are also large (up to a factor of 2) especially in FTP0 but the ATHET-CD results on FPT1 [14] confirmed that model improvements for the control rod material release due to evaporation were necessary. Some improvements were already presented in connection with a FPT2 analysis [39].

Table 2: Total release of some elements as calculated by ATHLET-CD and measured in the test

Source	Element	Initial bundle inventory (i.b.i.) g	Release, wt. % of i.b.i.	
			Calc. ATHLET-CD	Exp. FPT0
Fission product	I	0.03597	93.	100.
	Cs	0.1438	95.	84.
	Te	0.04734	97.	100.
Fuel	U	10533.	0.07	0.13
Control rod	Ag	476.8	2.	12.0
	In	89.4	2.	9.
	Cd	29.8	20.	47.

Figure 36 shows the release rate of elemental caesium as a function of time. It can be seen that the calculated release rate is in qualitative agreement with that of the measured one. The agreement might be better, if in the calculation the deposition of caesium (mainly as $CsMoO_4$) [87] between point B (bundle) and C before the steam generator (about 11 m apart from bundle exit) is taken into account.

The Cs-release kinetics approximately follows the temporal dependence of average bundle temperature (see Figure 27 and Figure 28) and it is predicted relatively well (see Figure 36). During the first oxidation period, the release rate is high for a short time. In the test and in the calculation as well, a significant Cs release occurred during the last heat-up phase between 14000 s and 17000 s. The release practically ceases at about 17000 s because no more caesium remained in the high temperature part of bundle. The calculation shows, that at 17000 s 90% of Cs is already released. In the test, the slump of molten pool ("final event") caused a sudden,

short increase in the Cs-release rate after shutdown. As already mentioned, this relocation cannot be simulated by the commonly used codes.

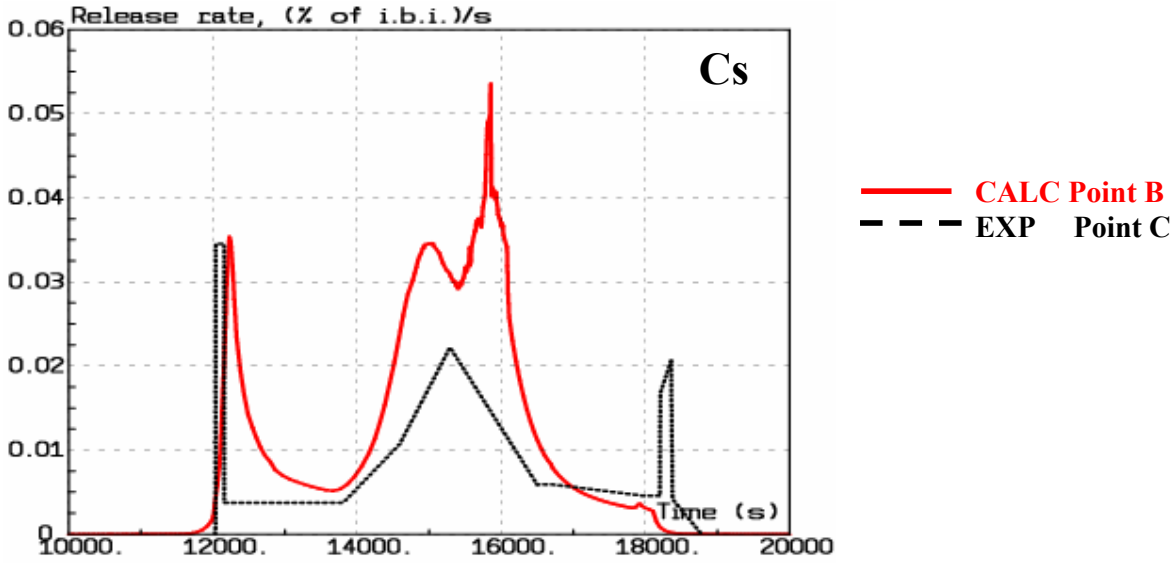

Figure 36: The release rate of elemental caesium at bundle exit calculated by ATHLET-CD and its measured flow rate at point C of circuit in the FPT0 test.

Figure 37 shows the calculated release rate of low volatile uranium as a function of time. During the first oxidation period, between 12000 s and 14000 s, the release rate is relatively small and most of the uranium is released towards the end of the degradation phase characterized by the largest power ramp and the highest bundle temperatures, respectively. The release of the high volatiles practically stops at about17000 s, while the release of low-volatile uranium increases until 18138 s (shutdown).

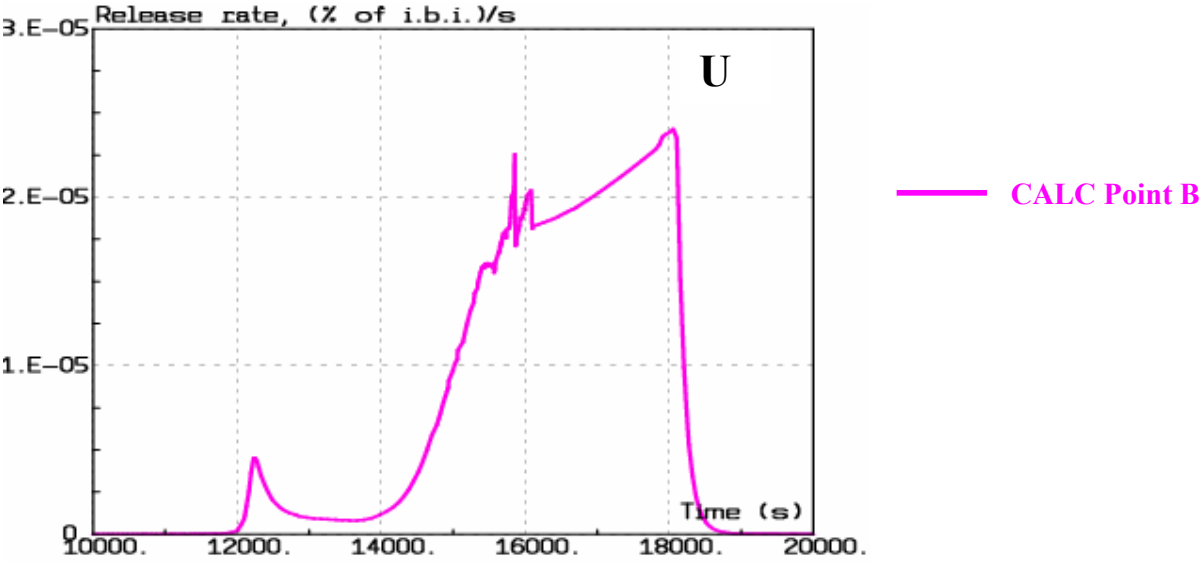

Figure 37: The release rate of elemental uranium at bundle exit calculated by ATHLET-CD for the FPT0 test

3.2.2.2 ICARE/ELSA and XMPR

One objective of the PHEBUS FP international research program is to provide data on core degradation and fission product release from the degrading fuel during severe accidents. FPT0 was the first experiment performed with a trace-irradiated fuel. The bundle degradation achieved during the experimental transient was significant as about 50% of the total fuel mass was liquefied. The associated volatile FP release was high, accounting for more than 80% of their initial bundle inventory. The semi volatile release was rather low (<3%), especially the release of Ba was lower than expected taken into account the results of separate effect tests [88].

The interpretation of the experimental FP releases during the FPT0 was mainly based on three different types of calculations. Calculations in stand-alone modes were performed using semi-empirical ELSA 1.1 rev1 [6] and mechanistic MFPR 1.1 rev2 [7]. Coupled calculations were also performed using the best-estimate bundle degradation calculations of ICARE V2 mod 2.3 combined with ELSA 1.1. A simplified model was used to calculate the release of Ag, In and Cd from the control rod.

In semi-empirical code such as ELSA, the modelling depends on each kind of FP. Indeed, for each category one different limiting phenomenon governing the release was taken into account. The limiting parameters considered were successively the fuel intra-granular diffusion for volatile FP since the fuel inter-granular porosities were supposed opened the evaporation and mass transfer into the opened porosities for semi-volatile and the fuel vaporisation at high temperatures for very low volatile FP. Only very few chemical effects are taken into account in ELSA.

The coupled ICARE-ELSA code, with the subsequent thermo-chemical calculations by using the GEMINI2 code, permits to take into account the degradation phenomena and to separate the release contribution of the intact fuel from molten pool [89]. We note that the calculations of the specific release associated with the molten materials as they relocate should be one of the improvements included in the upcoming version of the code.

In mechanistic codes such as MFPR, a complete description of gas behaviour inside and outside the fuel grain was taken into account. Atomic diffusion of the gas inside the grain, bubble nucleation, mobility and velocity of these bubbles in the intra and inter granular region are modelled. For each FP, a specific diffusion coefficient in the lattice of the fuel grain is taken into account. Chemical effects are also more extensively considered for most of the FP of interest.

Finally, the control rod behaviour was modelled by assuming that at the time of the rod rupture, which is quite well calculated by ICARE2, the mass transfer of the alloy to the outside surface of the rod was rather small and it mainly occurs through small cracks [90]. These small cracks would be caused by the eutectic interactions between the stainless steel clad and the Zircaloy guide tube of the control rod occurring at rather low temperatures. The mass transfer of Ag-In-Cd only became significant when the temperature reached the stainless steel clad melting point, because the increased dissolution of Zircaloy by molten stainless steel leads to the failure of the guide tube.

ELSA semi empirical code allowed quantifying the impact of the main users' parameters governing the release such as the diffusion length of the volatile fission products specifically and the steam access accounting for the fuel oxidation state. Taking into account a length of diffusion greater than the grain radius (accounting for the trace irradiated fuel used in FPT0), ELSA reproduces quite well the experimental release for volatile FP in terms of global fraction,

except for Te, but generally underestimated the releases of these fission products during the oxidation phase (see). This underestimation was mainly assigned to the simple Booth model unable to calculate the burst release of FP retained in the grain boundaries but could also be due to an inaccurate description of the dependence of the FP diffusion coefficient with fuel deviation stoichiometry following possible low temperature irradiation effects. Meanwhile, the release of semi volatile such as Ba and Ru was always lower than expected; and in all calculations, the release was overestimated because no chemical interactions are included in ELSA [91].

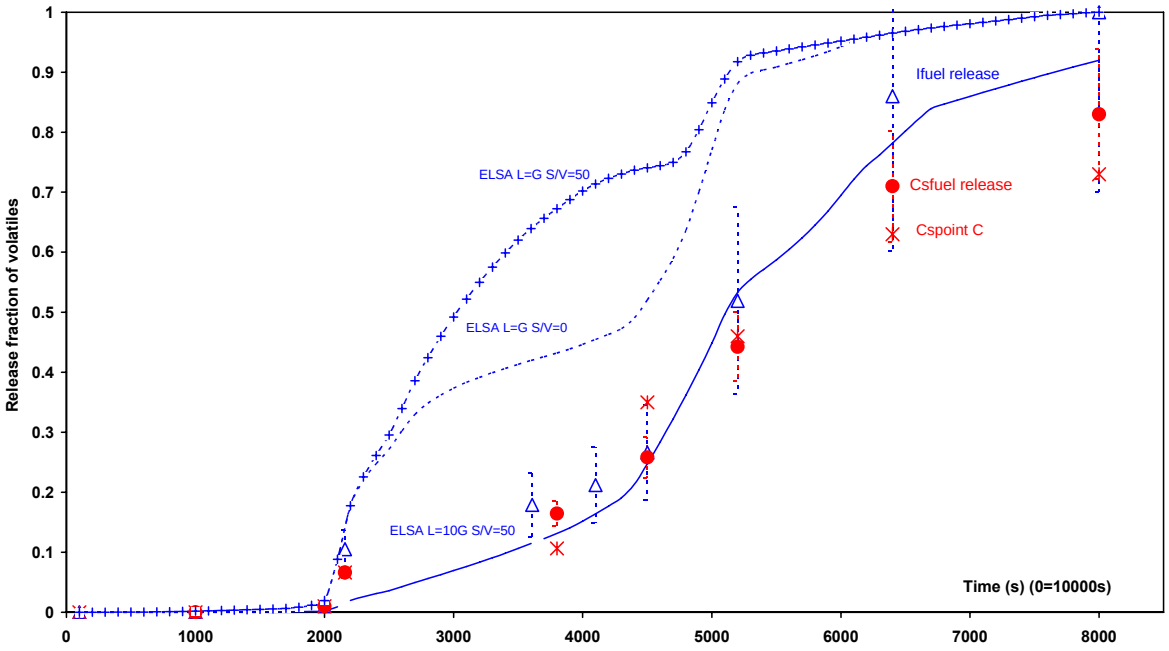

Figure 38: Iodine and Caesium kinetics release calculated by ELSA in a standalone mode as a function of length of diffusion (L) and steam fuel access (S/V): comparison with experimental data. For L=G the diffusion length is related to the fuel grain radius1.

The combined ICARE2-ELSA calculations (Figure 39 for some volatiles) describe quite accurately the molten pool in terms of chemical elementary composition. The results of these calculations were post-processed, and GEMINI2 tool associated with TDBCR981 database was used at each time step of the calculations in order to calculate the release from the molten pool. It was thus evidenced that only very low release was issued from the molten pool itself. As observed experimentally, the FP release measured during the molten pool phase was mainly due to the remaining part of intact fuel in the lower zones of the bundle where the molten materials flew down and relocated. The release in those bundle regions in which the molten pool is formed is rather low probably partly because of the reduction of the available surface for FP release.

1 In this graph, the calculated release of volatiles is compared to experimental data of Cs and I. For Cs two different curves are displayed corresponding respectively to the release kinetics of Cs as measured in the hot leg of the experimental circuit (Cs point C) and to the calculated release of Cs from bundle taking into account its deposited amount in the upper plenum, vertical line and horizontal line upstream the point C. For I, some additional data were calculated by taking into account the integral fraction of iodine measured in the containment.

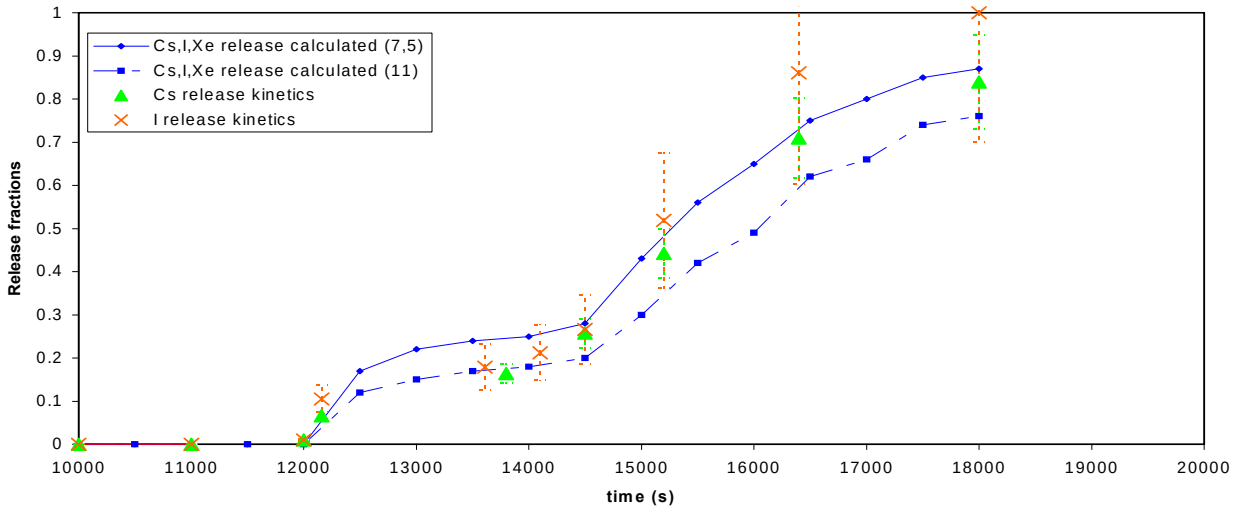

Figure 39: Comparison of calculated release fractions of volatile elements (ICARE2mod2.3 – ELSA1.1 for diffusion lengths L = 7.5 and L=11 microns and with S/V = 500) with experimental data.

The version of MFPR code used for the FPT0 calculations presented in this document permitted to evidence the importance of an accurate and mechanistic description of the FP gas behaviour inside the fuel (see

Figure 40). Indeed, the most recent version used includes several improvements concerning mainly intragranular processes (atom resolution factor, bubble nucleation factor, gas atom diffusivity, bubble mobility and velocity). In fact, MFPR can calculate a burst release of volatile fission products during the escalation phase. These new results are partly due to a decrease of the gas bubble nucleation factor, which induces an enhancement of intragranular bubble mobility.

Compared to ELSA, MFPR allows calculating the distribution of Fission Products (FPs) in the fuel, namely over the solid solution, the ternary compounds, and the ceramic/metallic phases. The partitioning of FPs between these different phases in the fuel was quite extensively studied and described by Kleykamp[2] [92]. Although the description of FPs location in MFPR is not so accurate, this helps to understand better the complex chemistry of FPs in the fuel and the release mechanisms associated.

The MFPR calculations evidenced that it is also of prime importance to determine accurately the location of each FP in the different chemical phases as a function of the composition of the atmosphere surrounding the fuel pellet because this directly controls the significance of the release phenomena. Indeed, the FP release is mainly governed by the intra- and inter-granular bubble behaviour (noble gases) and by the dependence of the diffusion coefficient on the stoichiometry of fuel pellet (I, Cs, Te, Xe). However, it also depends on the multiphase, multi-component equilibria proposed in MFPR for all FPs (except Xe), or in other words, on the thermodynamic stability of the predicted chemical compounds and on the partial activity of each FP in a given chemical phase.

2 Rare earths are nearly completely miscible in the UO_2 matrix under oxide forms at least for low burn-up fuel. Ba in the monoxide form is only very weakly miscible in UO_2 and forms separate ternary compounds like barium uranates, barium zirconates and/or barium molybdates, compounds which could be stable up to 2400-2600°C. For Cs the main stable possible compounds are caesium iodide, caesium uranates and/or caesium molybdates whereas the location of I supposed to be mainly as CsI phase is uncertain. The behaviour of Mo is complex because it could be both in dissolved for as atomic or oxide form or in metallic and ternary separated phases. Finally, the behaviour of Te is not well known and it could be partitioned between a dioxide form dissolved in the fuel, a metallic form and/or as a constituent of multi-component fuel-fission product.

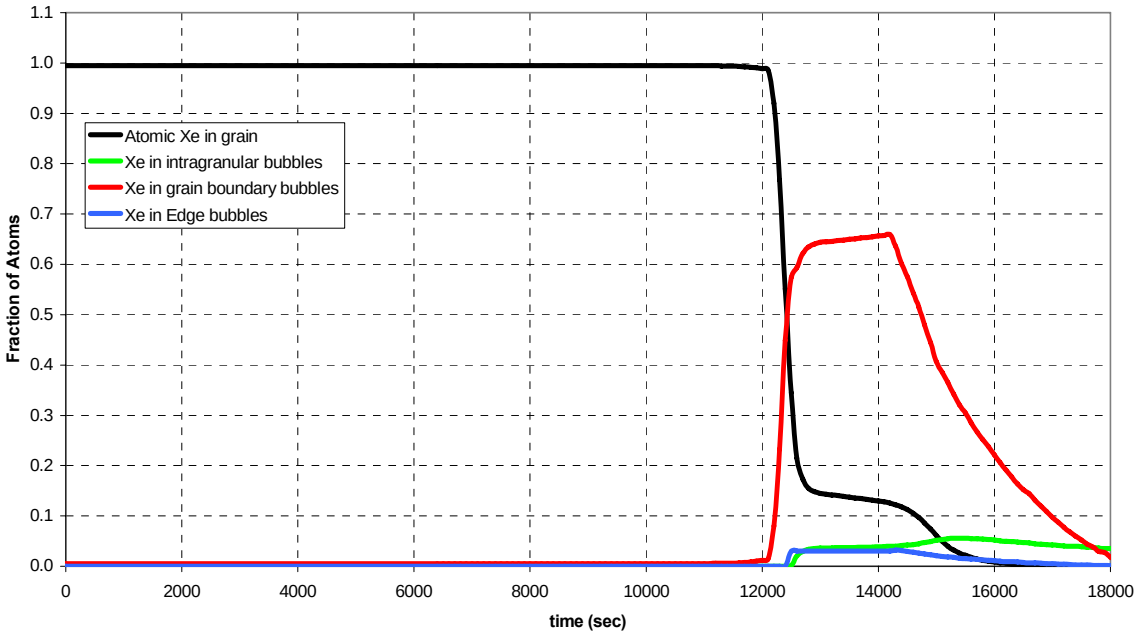

Figure 40: Xe atom distribution in FPT-0 calculated with MFPR V1.1rev2

Compared to the previous version of the code used to interpret FPT0, this new version allowed to reproduce quite well the integral release of volatile FP (except Sb very highly underestimated) both in terms of integral released fraction and in terms of release kinetics (see Figure 41) without considering any extensive early fuel melting. Indeed, the metallic melt formation and its influence on fission products release as well as the release from relocated melt are not taken into account in this calculation.

MFPR calculates the burst release associated with the temperature escalation due to the Zircaloy oxidation thanks to an accurate description of the fission gas bubbles under non-equilibrium conditions whereas fuel swelling is not taken into account. Nevertheless, it was not excluded that part of the release occurring during the escalation phase might be due to a possible early and partial fuel liquefaction caused by Zr-UO_2 interaction ([93, [95]). It is worth noting that a rather good agreement between the measured and calculated release was obtained with MFPR calculations despite the fact that the chemistry of some elements (such as Cs and Mo) is rather complex. Regarding MFPR, Cs is in the grey phase but under various forms (uranates, zirconates, molybdates). Part of these compounds becomes unstable during the temperature escalation and the remaining part is destroyed during the heat-up phase or later during the molten pool phase. This description is thus very dependent on the high temperature stability prediction of these compounds. Mo behaviour is varying depending on the phase where it is located (metallic phase, solid solution phase, grey phase).

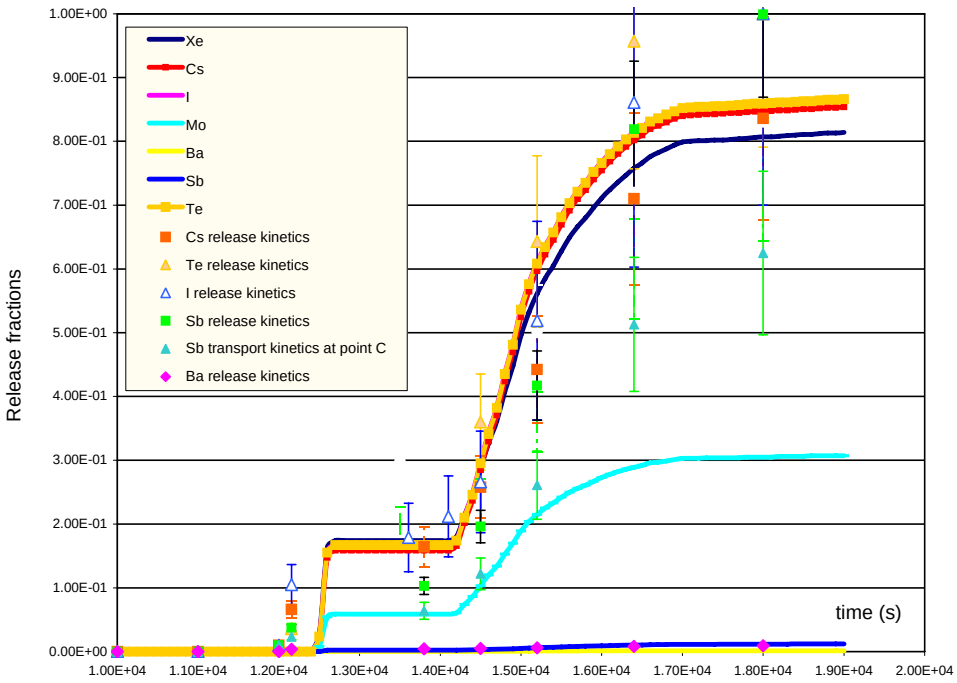

Figure 41: Release fractions calculated by MFPR1.1rev2 for FPT-0 (injected flow 10^{-3} m^3/s) and comparison to experimental data3

The release of semi volatile FP is very low and it is highly underestimated by the actual code version. This is probably related for Ba to the initial conditions of calculations considering a constant steam injection during the overall transient and thus increasing the stability of ternary compounds of Ba [96]. The calculations could be improved in the upcoming version of MFPR, which will permit to take into account the variation of composition and flow rate of the inlet gas injected. For Ru, the validity of the thermodynamic database related to Ru gaseous oxides (especially RuO_3) was suspected.

In FPT0, at the time of the control rod failure, the mass transfer of the Ag-In-Cd alloy to the external surface of control rod was probably low because of small size ruptures associated with eutectic interactions between the stainless steel clad encompassing the Ag-In-Cd and the Zircaloy guide tube surrounding this clad. At that time, mainly Cd vapour was released due to its increased pressure inside the control rod. This early burst of Cd vapour release was measured in FPT0; it is in agreement with the small-scale experiments [97], however it is not predicted by the model, which only calculates the vaporisation of the transferred alloy to the outer surface of the control rod. After stainless steel melting, the mass transfer of Ag-In-Cd alloy become significant and its relocation is rather quick. During the remaining part of the experiment, the release is thus associated with vaporisation of the alloy transferred. The release can thus be approximately calculated by simple temperature correlations.

The Ag release is quite well reproduced by the model both in terms of global fraction and in terms of kinetics. Meanwhile the calculated release of In is highly overestimated (see Figure 42) The low release of In observed in FPT0 could be assigned to the formation of In compounds of highest oxidation (like In_2O_3) state which are known to be less volatile.

The calculation of fuel deviation stoichiometry is of prime importance for volatile FP because their atomic diffusion inside the fuel grain is directly related to the oxygen potential of the fuel. Both ELSA and MFPR overestimated the fuel deviation stoichiometry compared to experimental values issued from post-mortem analyses of the molten materials. The main difficulty of modelling the fuel oxidation is due to the unknown and changing fuel morphology and steam access to fuel during the transient.

3 For FPT0 no experimental data were available concerning Mo release. For Sb, the experimental data corresponding to Sb mass transported through the hot leg of the experimental circuit were displayed together with the Sb release kinetics curve from bundle estimated by taking into account a deposited amount of Sb (in respect with its released value) equivalent to the deposited amount of Te (Sb release kinetics).

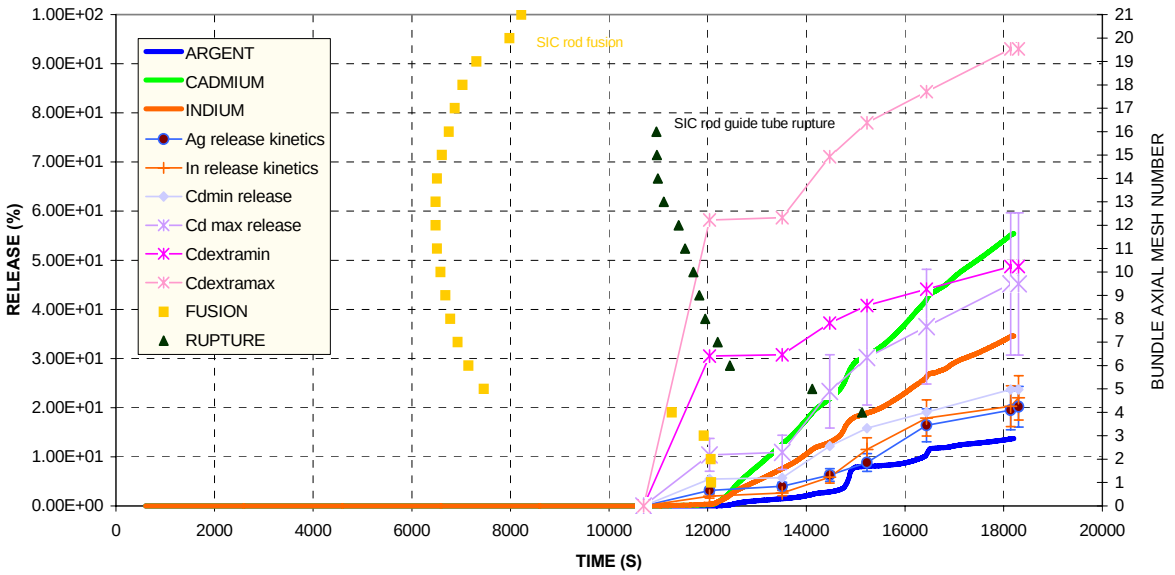

High temperature ramps might induce a significant release mechanism of fission gas. Indeed, the quick escalation of temperature would favour the formation of small fission gas bubbles of high internal pressure. The mobility of these gas bubbles inside the fuel grain would thus be enhanced. In addition, the release of these fission gases but also of others FP, which have moved out of the grains, could be enhanced by a possible rapid and long-range interconnection of the inter-granular porosities. The impact of high temperature ramps on the gas bubbles behaviour still needs to be analysed in order to improve the prediction of FP release by MFPR during the high temperature transient occurring in PHEBUS experiments during the Zircaloy oxidation phase.

The location of FP in the different possible phases of the fuel (solid UO_2 solution, ternary compounds, ceramic and metallic phases) also influences their release. It is thus important to model for each period of the transient (i.e. depending on the oxygen potential and on the temperature of the fuel) the possible chemical interactions between each element. In fact, the simply derived vapour pressure correlations included in ELSA cannot reproduce the release of some elements such as Ba. The low experimental release of Ba is indeed assigned to its specific chemical interactions with Fe and Zr. On the other hand, MFPR would predict more accurately the release of most of the FP except those (as Ru) for which the validity of the thermodynamic database is questionable, if the right composition of the inlet gas injection could be adjusted along the transient. This should be one of the main improvements of the upcoming version of the code.

Figure 42: Silver-Indium-Cadmium releases calculated with low transfer assumption[4]

[4] In this graph, several assumptions were proposed to recalculate the Cadmium bundle release from the experimental data. Indeed, during the FPT0 test the burst release of cadmium, which can begin since the rupture of the control rod at 10700 s, was probably missed as the first sampling was performed during the Zircaloy oxidation phase at roughly 12000 seconds. During the period 10700-12000 seconds, the Cadmium release rate for which any measurements are available can be assumed to increase linearly with time up to the value measured at 12000 seconds. Another source of uncertainties concerning the Cd release from the bundle is due to its deposited amount in the steam generator. Indeed, as Iodine, Cadmium was mainly transported in a vapour form through the hot leg of the experimental circuit. Calculation of the Cd release from the bundle can thus only be calculated from the data

of Cd transport kinetics measured in the cold leg corrected by the deposited amount in the steam generator. Compared to the release fraction of cadmium this deposited amount was estimated to 59.5% in FPT0 and 22.8% in FPT1. Probably, the value issued from post-test analyses of some steam generator segments was significantly overestimated in FPT0 and so the corresponding released value (Cdextramax). Meanwhile assuming a deposited amount of about 23% of the release Cd fraction leads probably to an underestimation of the Cd bundle release, as the amount of Cd transported in the cold leg during the FPT0 test was significantly lower than in the FPT1 test. The four different curves for Cd bundle release were thus corresponding to:

Cdminrelease/ Cdmax release: considering that the Cd release only began during the Zircaloy oxidation phase and considering two different values for Cd deposited amount in the steam generator (Cdmin corresponding to the minimum deposited value).

Cdextramin/Cdextramax: considering that the Cd release already began at the control rod rupture with also two different values for stem generator deposited amount

Cdminrelease/ Cdmax release: considering that the Cd release only began during the Zircaloy oxidation phase and considering two different values for Cd deposited amount in the steam generator (Cdmin corresponding to the minimum deposited value).

Cdextramin/Cdextramax: considering that the Cd release already began at the control rod rupture with also two different values for stem generator deposited amount

4 Discussion and Conclusions

More than ten years after the first test FPT0 of the PHEBUS FP programme, the actual status in the understanding of the dominant bundle processes was presented. Hereby, mainly the results reported in the Bundle Interpretation Circles obtained from extensive and detailed analyses using specific models and commonly used severe accident codes or selected modules, respectively, were discussed.

Considering the code predictions on the temperature escalation in the bundle due to clad oxidation and the combined hydrogen production, one can conclude that the Zircaloy oxidation is satisfactory simulated by means of empirical correlations. This is the case although the analyses with ATHLET-CD indicated that Prater-Courtright is the best choice whereas for ICARE2 developed at IRSN, the analysts recommended the Urbanic-Heidrick correlation. Taking into account the most precise measured data of different small-scale experiments on clad oxidations a new oxidation correlation was derived and recommended to the code developers ([98], [99]). After implementation in the mechanistic codes mentioned above, the analysts reported [41], that there occurred an overshooting in the temperatures mainly towards the end of the temperature escalations. It is difficult to assess these results, because also in the mechanistic codes there are differences in the modeling of each single process as well as in the realization of the interplay of the models.

As an example, the code analyses showed, that using the different oxidation correlations recommended by the analysts, ICARE2 predicts that the maxima of the total heat release due to oxidation is at a about factor 2 higher compared to ATHLET-CD although the used Prater-Courtright correlation would lead under the same temperature-transient to higher oxidation rates. However, in ICARE2, the heat-loss to the gas at maximum oxidation is lower approximately about the same factor. Consequently, the uncertainties of the overall code modeling as well as the fact that in the separate effect tests the temperature is very well defined? compared to the bundle temperature distribution in integral tests. This can explain the differences in the results of the calculations with respect to the oxidation. Generally, the calculated temperatures have to be used to determine the heat release due to oxidation. However, as also shown in frame of a benchmark study with ATHLET-CD, ICARE2 and MELCOR by using the same boundary conditions, very similar results were obtained for the thermal bundle behavior and the produced hydrogen mass production [86]. Therefore, one can conclude, the clad oxidation can be adequately simulated using the correlations recommended by the analysts. From theoretical point of view, it would appear advantageous to find a consensus for a unique choice of the oxidation correlation taking into account the most advanced correlation derived from data of the separate effect tests [88]. However, an enormous effort would be necessary, because at first not only the modelling and the coding of the oxidation correlation together with the formulation of the combined heat release have to be compared, but also the modelling of other heat sinks or sources have to be re-analyzed in detail.

Compared to the modelling of the cladding behaviour of fuel rods - including the burst release of small amounts of fission products due to stress-induced failure - the modelling of the control behaviour according to [78] was assessed as insufficient, however, despite the great efforts made in the modelling during the last years further improvements still seem to be necessary. In both mechanistic codes ATHLET-CD and ICARE2/ELSA the modelling of the release of control rod components from the molten alloy is based on the formulation of the evaporation process whereas in the past an empirical correlation derived from a specific test series was used. In ICARE2/ELSA, by means of a parameter, the experimental results for the burst as well as for the release during and after control rod failure could be reproduced and were re-checked on FPT1 data. It should be noted, that the measured release kinetics is connected with relatively large uncertainties but more important is, that in the present status of

the modelling an extrapolation to reactor conditions is more than questionable. Less expenditure might be necessary to simulate more mechanistically the burst release connected with internal pressure built-up compared to the modelling of the control rod material release after failure of the guide tube. Hereby, the history of the melt relocation, i.e. the actual temperature and surface area has to be calculated, but also the chemical reactions, i.e. mainly oxidation by steam, have to be taken into account. The control rod failure is mostly simulated by using a temperature criterion therefore the timing of the control relocation could be well reproduced. However, it seems to be more adequate to use models considering the material interaction between the guide tube and control rod cladding even if the results do not significantly differ from those obtained by an adequate setting of the temperature criteria.

Concerning the fuel rod degradation, one can differ between the early fuel relocation and massive fuel relocation at higher temperatures, which lead to the formation of the molten pool. The latter was the most surprising result in FPT0 [2], because one does not expect the formation of such large molten mass below the eutectic temperature of the UO_2/ZrO_2- system, i.e. below 2800 K, which is the default value of the temperature criterion for the relocation of core materials in severe accident codes.

The early melting occurred in the FPT0 test due to the relatively moderate heat-up rate during the temperature escalations after reaching the melting point of the α-Zircaloy (2248 K), i.e. when there is sufficient time for a complete phase transformation of the β- (melting point: 2033 K) to α-Zircaloy. Then, the metallic U-Zr-O melt is formed due the dissolution of the urania by molten Zircaloy, and after cladding failure, the melt can relocate downwards to lower bundle positions. In the mechanistic modelling of SVECHA code, the evaluation of the oxide scale under interaction with molten Zircaloy depends on the oxide scale and metal phase thickness, oxygen content in molten Zircaloy and the oxygen flux at the cladding surface. The code predicts the failure of the oxide shell at high elevations already during temperature escalation just after metal α-Zr(O) melting (≈ 12050 s), leading to formation of local molten pools above the upper space grid of the FPT0 bundle.

In the commonly used severe accident codes, the clad failure is simulated by means of criteria dependent on the local temperature and the thickness of the zirconia layer at the outer rod surface. By an adequate choice of the parameters, the onset of the early melt relocation can be also relatively well simulated. Using the diffusion model of Kim-Olander [53], ATHET-CD predicts that 0.225 kg of metallic melt was relocated during the oxidation phase.

By artificially reducing the "melting temperature" of the fuel to 2500-2600 K the effects of non-equilibrium material interactions in the Zr-U-O system can be roughly simulated with the codes. It was shown that the dissolution of UO_2 by the melt strongly increased under conditions when the temperature of the pellet temperature is by several degrees higher than the temperature of the U-Zr-O melt. In this case, the fuel dissolution is not anymore restricted by the saturation limit of oxygen in the melt and the fuel dissolution actively proceeds in the oversaturated melt. This process (along with the melt oxidation by steam), leads to the enhanced over-saturation of the melt and to an increased rate of $(U,Zr)O_{2-x}$ ceramic phase precipitation. Therefore, a relatively quick transformation of UO_2 phase into the mixed $(U,Zr)O_{2-x}$ ceramic phase (owing to dissolution and precipitation) is predicted by this mechanism which leads to the formation of the molten pool [13]. Other hypotheses, e.g. the reduction of the melting temperature can be justified due to the presence of other than zirconium metallic component or that bundle temperatures above 2800 K are reached – as predicted by the porous medium model approach – can not completely excluded. However, as observed in the FPT4 test [100] the approach to the eutectic temperature in the pure mixture of ceramic phases (without metallic melt) will hardly result in homogeneous eutectic melting of the mixture and in its subsequent homogeneous solidification on cool-down as observed in the bundle tests. Although the fuel dissolution is not adequately simulated, the predicted relocated

mass 2.9 kg (ICARE2) and 3.8 kg (ATHLET-CD) appear acceptable considering the spread of the results of the code-to-code benchmark study [86].

Concerning the volatile fission products, the analysis and interpretation of FPT0 experimental release results suffers from uncertainties mainly not only related to the fuel oxidation state and to the high temperature escalation during the Zircaloy oxidation phase. The accurate estimation of the fuel oxidation is difficult mainly because of uncertainties concerning the actual volume and composition of the gas phase having access to the fuel but also because of the complicated description of the deviation from stoichiometry in the fuel. On the other hand, the high temperature escalation that occurred during the FPT0 test could be responsible for a significant enhancement of the volatile fission product release. The effect of this high temperature escalation, probably inducing specific behaviour of fission gas bubbles is not yet completely understood and described. Some improvements are already included or will be included very soon in the new version of the codes. This concerns the calculation of volatile fission product release from early fuel melting in ICARE2/ELSA and a modified description of the gas bubble behaviour in the last MFPR 1.2 version. In particular, in this new version the grain boundary diffusion of gas atoms to edges would be possible before interlinking of inter-granular bubbles, which would favour an early release of fission gases. In addition, models considering thermal resolution, grain boundary sweeping and dislocation effects will be included. The description of the gas phase will be also more accurate which will permit to describe better the chemistry of some fission products such as Cs and Ba. Other future work to improve the modelling of the volatile fission products will mainly deal with the ELSA code. In this code, the oversimplified approximation of initial uniform repartition of the fission product in the fuel grain, the chemical combination of some elements and the formulation of the diffusion coefficients should in particular be improved.

Concerning the semi-volatile fission products, the main uncertainties are related to the interactions of these products with structural materials. These interactions are not correctly modelled in the codes. Another source of error comes from the uncertainty regarding to the thermodynamical stability of some ternary compounds formed in the fuel and to the accurate description of the partition of each fission product between the different possible phases (metallic phase, ternary compounds, solid solution, and CsI phase). In that sense, the modelling in MFPR is more adequate to describe the release of semi-volatile fission product. This modelling should still be improved by mainly focusing on the stability of Cs ternary compounds and the behaviour of Mo, Sb and Ba in the fuel matrix.

5 References

[1] Mailliat, A., Jones, A.: Final Test Protocol for the Phebus-FP test FPT0, Note Technique Phebus PF IP/93/180, Note Technique SEMAR 93/03, SAWG/93.110, 1993

[2] Shepherd, I. et al: Intermediate Analysis report of the Phebus FP test FPT-0: Bundle Degradation and Release (The Ability of codes to Reproduce Core Behaviour in FPT-0), TG343, SAWG97/010, Ispra, 6th October, 1998

[3] Gonzales, R. , Chatelard, P. and Jacq, F. ICARE2 – a computer program for severe core damage analysis in LWRs, Note Technique SEMAR 93/33, Institut de Protection et de Sûreté Nucléaire, France (1993)

[4] Jacq, F. et al.: ICARE2 – V3mod1: A computer program for severe core damage Analyses in LWRs, 2001

[5] Trambauer, K., Bals, C., Schubert, J. D., Austregesilo, H.: ATHLET-CD Mod 2.0 - Cycle A User's Manual, Gesellschaft für Anlagen- und Reaktorsicherheit (GRS) mbH, Germany, GRS-P-4, Vol. 1. (2004)

[6] Manenc, H., Kissane, M., Giordano, P.: ESCADRE mod 1.2 – ELSA code version 1.1 revision 1: Fission Product release from the reactor core, N.T. SEMAR 98, 1997

[7] Berdyshev, A. V., Ozrin, V.D Shestak, Tarasov V.E., Veshchunov, M.S.: MFPR module version 1.3 – User manual, Nuclear Safety Institute (IBRAE), Russian Academy of Science, NSI-SARR-129-02, February 2002

[8] Veshchunov, M. S.: U-O-Zr oxidation model, JRC Technical Note P.02.35, September 2001

[9] Veshchunov, M. S., Berdyshev, A. V.: Final Report on U-Zr-O Melt Oxidation Model, JRC Technical Note No. P. 02. 84, SAM-COLOSS-P039, Petten, August 2002

[10] Veshchunov, M. S., Mueller, K., Berdyshev, A.V.: Molten Corium Oxidation Model, Nuclear Engineering and Design, Volume 235, Issue 22, November 2005

[11] Veshchunov, M.S.: Analysis of Melt Physico-Chemical Interactions in PHEBUS FP tests, JRC Technical Note No. P.03.120, SAWG No. 2003/3, Petten, July 2003

[12] Veshchunov, M. S., Boldyrev, A. V., Palagin, A.V., Mueller, K.: Analyses of the Phebus FPT0 and FPT1 Tests using extended Models for Molten Pool Formation - Interim Report, EUR 21843 EN, SAWG 2005/04, November 2005

[13] Veshchunov, M. S., Boldyrev, A.V., Mueller, K.: Analyses of the Phebus FPT0 and FPT1 Tests using extended Models for Molten Pool Formation - Final Report, EUR 22207 EN, SAWG 2006/01, May 2006

[14] B. Clement and T. Haste: "ISP-46 PHEBUS FPT1: Integral Experiment on Reactor Severe Accidents", Comparison Report, NEA/CSNI/R(2004)18 (2004)

[15] Hanniet N., Gaillot S., Berthet B., Repetto G., Garnier G., Phebus PF - FPT0 - Preliminary Report, IPSN Technical Note NT 9/94, 1994

[16] Hanniet-Girault, N., Repetto, G.: FPT0 Final Report, Final Version, December 1998

[17] von der Hardt P., Jones A.V., Lecomte C., Tattegrain A., Nuclear Safety Research: The Phebus FP Severe Accident Experimental Programme, Nuclear Safety 35(2), 1994

[18] Clement, B., Hanniet-Girault, N., Repetto, G., Jacquemain, D., Jones A. V., Kissane M., von der Hardt, P.: LWR severe accident simulation: synthesis of the results and interpretation of the first PHEBUS FP experiment FPT0, Nuclear Engineering and Design Volume 226, Issue 1, 2003

[19] Krischer W.: Minutes of the 1st Meeting of the Bundle Degradation Interpretation Circle, SAWG 94 - 056/0, January 1995

[20] Krischer W.: Minutes of the 2nd Meeting of the Bundle Degradation Interpretation Circle, SAWG 95 - 018/1, May 1995

[21] Krischer W.: Minutes of the 4th Meeting of the Bundle Degradation Interpretation Circle, SAWG 95 - 031/1, 1995

[22] Shepherd I, Vandegehuchte M., Minutes of the 5th Meeting of the Bundle Interpretation Circle, SAWG 95 - 046/1, October 1995

[23] Shepherd I.: Minutes of the 6th Meeting of the Bundle Interpretation Circle, SAWG 96 - 011/1, 1996

[24] Shepherd I.: Minutes of the 7th Meeting of the Bundle Interpretation Circle, SAWG 96 - 023/1 1996

[25] Haste T. J.: Minutes of the 8th meeting of the Bundle Interpretation Circle, JRC Technical Note No.I.97-02/1 SAWG 97-02/1, 1997

[26] Haste T. J.: Minutes of the 9th meeting of the Bundle Interpretation Circle, Technical Note No. I.97.183, 1997

[27] Haste T. J.: Minutes of the 10th meeting of the Bundle Interpretation Circle, Technical, 1998

[28] Haste T. J.: Minutes of the 11th meeting of the Bundle Interpretation Circle, Technical Note No. I.98.260, SAWG 98-009/1, December 1998

[29] Haste T. J., Mason, P.: Minutes of the 12th meeting of the Bundle Interpretation Circle, Technical Note No. I.99.98, SAWG 99-006/1, May 1999

[30] Haste T. J.: Minutes of the 13th meeting of the Bundle Interpretation Circle, Technical Note No. I.00.06, SAWG 00-001/1, January 2000

[31] Haste T. J.: Minutes of the 14th meeting of the Bundle Interpretation Circle, Technical Note No. I.00.66, SAWG 00-005/1, May 2000

[32] Mueller, K.: Minutes of the 15th Bundle Interpretation Circle, Aix-en-Provence, October 4, 2000, Technical Note I.01.19, February 2001

[33] Krausmann, E.: Minutes of the 16th Bundle Interpretation Circle, Belgirate, March 15, 2001, Technical Note I.01.54, May 2001

[34] Krausmann, E.: Minutes of the 17th Bundle Interpretation Circle, Aix-en-Provence, November 29, 2001, Technical Note P.02.29, March 2002

[35] Krausmann, E.: Minutes of the 18th Bundle Interpretation Circle, Petten, Netherlands, March 21, 2002, Special Publication P02.107, August 2002

[36] Toth, B.: Minutes of the 19th Meeting of the Phebus FP Bundle Interpretation Circle (Aix-en-Provence, October 17, 2002), JRC Technical Note TN.P.03.55, March 2003

[37] Toth, B.: Proceedings of the 20th meeting of the Phebus-FP Bundle Interpretation Circle (Bergen, March 27, 2003), JRC Technical Note TN.P.03.151, October 2003

[38] Toth, B.: Proceedings of the 21st Meeting of the Phebus FP Bundle Interpretation Circle (Aix-en-Provence, October 29, 2003), JRC Technical Note TN.P.04.47, March 2004

[39] Toth, B.: Proceedings of the 22nd Meeting of the Phebus FP Bundle Interpretation Circle (Bergen, April 2004), JRC Technical Note TN.P.04.110, September 2004

[40] Toth, B.: Proceedings of the 23rd Meeting of the Phebus FP Bundle Interpretation Circle (Aix-en-Provence, November 04, 2004), JRC Technical Note TN.P.04.155, December 2004

[41] Toth, B.: Proceedings of the 24th Meeting of the Phebus FP Bundle Interpretation Circle (Bergen, April 28, 2005), JRC Technical Note P2005/223, December 2005

[42] Toth, B.: Proceedings of the 25th Meeting of the Phebus FP Bundle Interpretation Circle (Aix-en-Provence, 19 October 2005), JRC Technical Note P2006/025, April 2006

[43] Scheurer, H.: Phebus FP Data Book FPT0. PH-PF IS/92/48 (unpublished report, 16 February 1994 revision), 1994

[44] Plumecocq, W., Guillard, G.: ASTEC V1.2 code. ELSA module: fission product and structural element release from intact and degraded core, Note Technique SEMIC-2005-162, May 2005

[45] Hofmann, P., Markiewicz, M.: Chemical Behaviour of (Ag-In-Cd) absorber Rods in Severe LWR accident, KfK Report 4670, 1990

[46] Otomo, T., Nagase, F., Uetsuka, H.: Metallographic Examination and EPWA analysis of Ag-In-Cd Control Alloy annealed at high temperatures, Data Report No. 1, JAERI, 1988

[47] Taylor, P.: Calculations of the volatility of control elements in various atmospheres at 1200 to 2500 K, Technical Note IPS/DRS/SEMAR 98/160

[48] Schanz, G.: Recommendations and supporting information on the choice of zirconium oxidation models in severe accident codes, Report FZKA-6827, Karlsruhe, Germany, 2003

[49] Hofmann, P., Stuckert, J., Miassoedov, A., Veshchunov, M. S., Berdyshev, A. V., Boldyrev, A. V.: ZrO_2 Dissolution by Molten Zircaloy and Cladding Oxide Shell Failure. New Experimental Results and Modelling, - Report FZKA 6383, INV-CIT(98)-P026, Karlsruhe, Germany, 1999

[50] Tolman, E. L., et al.: TMI-2 Core Acquisition Summary Report, EG&G Idaho, E66-TMI-7757, 1996

[51] Hayward, P. J., Hofmann, P., Stuckert, J., Veshchunov, M. S., Berdyshev, A.V.: UO_2 Dissolution by Molten Zircaloy. New Experimental Results and Modelling. Report FZKA 6379, INV-CIT(99)-P029, Karlsruhe, Germany, 1999

[52] Veshchunov, M. S., Stuckert, J., Berdyshev, A. V.: Modelling of Zr-O and U-Zr-O Melts Oxidation and New Crucible tests, - Report FZKA 6792, SAM-COLOSS-P040, Karlsruhe, Germany, December 2002

[53] Kim, H. T., Olander, D. R.: Dissolution of uranium dioxide by molten Zircaloy (convection-controlled reaction), Journal of Nuclear Materials, p. 154, 1988

[54] Hofmann, P., Uetsuka, H., Wilhelm, A. N., Garcia, E. A.: Dissolution of solid UO_2 by molten Zircaloy and its modelling, Int. Symp. on severe accidents in nuclear power plants, Sorrento, Italy, March 1988

[55] Hayward, P. J., George, I. M.: Dissolution of UO2 in molten Zircaloy-4, Part 1 and 2, Journal of Nuclear Materials, 208, p. 35-52, 1994

[56] Adroguer, B., et al.: Corium interactions and thermochemistry (CIT), FISA 99, EU Research in Reactor Safety, Luxembourg, 29 November –1 December 1999

[57] Hofmann, P., Hagen, S., Schanz, G., Skokan, A.: Chemical Interactions of reactor core materials up to very high temperatures, Kernforschungszentrum Karlsruhe, KFK 4485, Jan. 1989

[58] Veshchunov, M. S., Berdyshev A. V.: Modeling of chemical interactions of fuel rod materials at high temperatures. Part 1: Simultaneous dissolution of UO2 and ZrO2 by molten Zircaloy in an oxidizing atmosphere, Journal of Nuclear Materials 252, p. 98-109, 1997

[59] Bruder, M., Hocke, K.-D., Kronenberg, J., Müller, K., Paller, A., Schlenkrich, C.: KESS-III/MOD2.0 Dokumentation, Institut für Kernenergie und Energiesysteme, Universität Stuttgart, IKE -TF –12, April 1995

[60] Allison, C. M., et. al: SCDAP/RELAP/MOD3 Code manual, NUREG/CR-5273, EG&G Idaho

[61] Darcy, H.: Les Fontaines Publique de la Ville de Dijon, Dalmont, Paris 1856

[62] Haste T. J.: Minutes of the 11th meeting of the Bundle Interpretation Circle: "FPT1 Post-test Analysis using ICARE2 V3mod0 Code - Fuel Pellets Slumping Scenario" presented by Mercedes Ortega Bernardo, Technical Note No. I.98.260, SAWG 98-009/1, December 1998

[63] Repetto, G.: Analysis of the FPT-0, FPT-1 and FPT-2 experiments with the ICARE/CATHARE code, 5th Technical Seminar on the Phebus FP Program, Aix-en-Provence, June 24-26, 2003

[64] Hofmann, P., Hagen, S., Noack, V., Schanz, G., Schumacher, G., Sepold, L.: Kerntechnik 59, p. 197, 1994

[65] Hagen, S., Hofmann, P., Noack, V., Schanz, G., Schumacher, G., Sepold, L.: Test Results of Experiment CORA W1, Report KfK 5212, 1994

[66] Noack, V., Hagen, S., Hofmann, P., Schanz, G., Sepold, L.: Material distribution in LWR-type Bundles Tested under Severe Accident Conditions, Nuclear Technology, 117, p.158-170, 1997

[67] Veshchunov, M. S., Palagin, A. V.: Modelling of chemical interactions of fuel rod materials at high temperatures. Part 2: Investigation of downward relocation of molten materials, Journal of Nuclear Materials 252, p.110-120, 1997

[68] Hofmann, P., Horn, L., Leiling, W., Piel, D., Schmidt, L., Sepold, L., Steinbrück, M.: QUENCH-02. Test Data Report, PSF3303, 1998

[69] Hofmann, P., Homann, C., Horn, L., Leiling, W., Miassoedov. A., Piel, D., Schmidt, L., Sepold, L., Steinbrück M.: QUENCH-03. Test Data Report, PSF3316, 1999

[70] A.C. Grégoire, Ph. Chapelot, G. Grégoire: FPT4 Final Report, Institut de Radioprotection et de Sûreté Nucléaire (IRSN), Cadarache, France, April 2004

[71] Müller, K. Goryachev, A.V., Smirnov, V. P., Svyatkin, A. M., Stuckert, J., Veshchunov, M. S., Berdyshev A. V.: Simultaneous Dissolution of UO_2 and ZrO_2 by Molten Zircaloy. New Experiments and Modelling, Report FZKA 6947, SAM-COLOSS-P074, Karlsruhe, Germany, January 2004

[72] Smirnov, P., Syatkin, A. M.: WP2.1 Simultaneous Dissolution of UO_2 and ZrO_2 by molten Zry - Final Report, SAM-COLOSS-P047, 2003.

[73] Veshchunov, M. S., Berdyshev, A. V., Boldyrev, A. V: ICARE/COLOSS-IBRAE, Intermediate Report, Task 1: Modelling of the simultaneous dissolution of UO2 and ZrO2 by molten Zircaloy, Task 2: Validation of the SVECHA model against AEKI single rod tests (fuel rod degradation and clad failure tests), NSI–SARR–150–03, February 2003

[74] Herring, W., Homann, C., Lamy, J. S., Miassoedov, A., Schanz, G., Sepold, L.: Comparison and Interpretation Report of the OECD International Standard Problem No. 45 Exercise (QUENCH-06), FZKA 6722, April 2002

[75] Krausmann, E.: Minutes of the 17th Bundle Interpretation Circle, Aix-en-Provence, November 29, 2001: "Main results of Boron Carbide Experiments" presented by Miassoedov, A. (FZK, Germany), Technical Note P.02.29, 2001

[76] Steinbrück, M. (Editor): 7th International Quench Workshop, Germany, Forschungszentrum Karlsruhe, Internal Report, January 2002

[77] Golden, W. D.: Summary of the Three Mile Island Unit 2 Analysis Exercise, Nuclear Technology, Vol. 87, 1989

[78] Shepherd, I. M. et al.: Investigation of ore Degradation (COBE) - Final Report, EUR 18982 EN, 1999

[79] Krausmann, E.: Minutes of the 18th Bundle Interpretation Circle, Petten, Netherlands, March 21, 2002: "Phebus pre-test and post-test calculations to FPT2 and FPT3 with new candling model of ATHLET-CD presented by Trambauer, K. (GRS, Germany), Technical Note in preparation, 2002

[80] Hagen, S., Hofmann, P., Noack, V., Schanz, G., Schumacher, G., Sepold, L.: Test results of experiment CORA W2, KfK 5212, 1994

[81] Adroguer, B., Chatelard, P., Van Dorsselaere, J. P., Duriez, C., Cocuaud, N., Bellenfant, L., Bottomley, D., Vrtilkova V., Mueller, K. et al.: Core loss during a severe accident (COLOSS), Nuclear Engineering and Design, Volume 235, Issues 2-4, February 2005

[82] Veshchunov, M.S., Berdyshev A.V.: JRC/COLOSS-IBRAE, Final Report, Development of a model for the simultaneous dissolution of UO_2 and ZrO_2 by molten Zr, NSI–SARR–151–03, March 2003

[83] Adroguer, B., Chatelard, P., Dorsselaere, J.P., Duriez, C., Cocuaud, N., Bellenfant, L., Bottomley, L., Vritlkova, V., Mueller, K. et al.: Core loss during a severe accident (COLOSS). Nuclear Engineering and Design, Volume 221, Issues 1-3, April 2003

[84] Hobbins, R., Osetek, D. Louie, D.: Phebus FPT0 Synthesis Report, 1995

[85] Ronchi, C., Sheindlin, M., Int. J. Thermophys., 23 (2002) 293

[86] Toth, B., Birchley, J., Hozumi, W., Jamond, C., Trambauer, K., Mueller, K.: Pre -Test Calculations of the FPT3 Experiment Using the MELCOR, ATHLET-CD Computer Codes (Comparative Study), EUR 21555 EN, SAWG 2005/01, August 2005

[87] Bujan, A., Mueller, K., Zeyen, R: "Circuit Analyses of the PHEBUS FPT0 and FPT1 Tests Using the Fission Product Transport Code SOPHAEROS", EC JRC Report EUR 21847 (2005)

[88] Ducros, G., Malgouyres, P., Kissane, M., Boulaud, D., Durin, M: Fission Product release and fuel behaviour under severe accidental conditions: Synthesis of the VERCORS 1-5 experimental program, International Topic Meeting on Light Water Reactor Fuel Performance, Park City, Utah, 10-13 p 1110, April 2000

[89] Manenc, H., Mason, P.: Analysis of Fission Product release from intact fuel and the molten pool in FPT0, N.T. SEMAR 20, 2000

[90] Dubourg, R., Lemoine, F.: Modelling of Silver-Indium Cadmium rod release, N.T. SEMAR 127, 1999

[91] Dubourg, R., Taylor, P.: A qualitative comparison of barium behaviour in the PHEBUS FPT0 experiment and analytical experiments, J. Nucl. Mat. 294 32-38, 2001

[92] Kleykamp, H.: The chemical state of fission products in oxide fuel, J. Nucl. Mat. 131, 221-246, 1985

[93] Dubourg, H. Manenc and N. Davidovitch Interim synthesis of interpretation of the Fission Product release in the Phebus FPT0 experiment N.T. SEMAR 65, PHEBUS/IP 01/499, 2001

[94] Bourdon, S.: Phebus FPT0-FPT1: Preliminary synthesis of the experiment analyses using ICARE 2 code, N.T. SEMAR 137, PHEBUS/IP 98/409, 1998

[95] Dubourg, R., Faure-Geors, H., Nicaise, G., Barrachin, M.: "Fission product release in the first two PHEBUS tests FPT0 and FPT1", Nuclear Engineering and Design, Volume 235, 2005

[96] Taylor, P.: Volatility of Barium in the system Ba-U-O, N.T. SEMAR 06, 1999

[97] Petti, D. A.: Silver-Indium-Cadmium rod behaviour in severe reactor accidents, Nuclear Technology 84, 128-151, 1989

[98] Schanz, G., Adroguer, B., Volchek, A.: Advanced treatment of zircaloy cladding high-temperature oxidation in severe accident code calculations, Part I. Experimental database and basic modelling, Nuclear Engineering and Design, Volume 232, 2004

[99] Volchek, A., Zvonare, Yu., Schanz, G.: Advanced treatment of Zircaloy cladding high-temperature oxidation in severe accident code calculations, Part II. Best-fitted parabolic correlations, Nuclear Engineering and Design, Volume 232, 2005

[100] Grégoire, A.C., Chapelot, Ph., Grégoire, G.: FPT4 Final Report, Institut de Radioprotection et de Sûreté Nucléaire (IRSN), Cadarache, France, April 2004

European Commission

EUR 23222 EN – DG Joint Research Centre, Institute for Energy
Luxembourg: Office for Official Publications of the European Communities
2007 – 71 pp. – 21 x 29.7 cm
EUR - Scientific and Technical Research series - ISSN 1018-5593

Abstract

In this paper, the actual status of understanding of the dominant bundle degradation processes is presented. Here, mainly the results reported in the last years in the Bundle Interpretation Circles organised by JRC/IE and IRSN (Institut de Radioprotection et de Surete Nucleaire, Cadarache) are summarised. For the extensive and detailed computational analyses the commonly used severe accident codes such as ICARE, MELCOR, SCDAP/RELAP and ATHLET-CD are used. For the analysis of fission product release from the FPT0 bundle, specific codes such as SVECHA and XMPR were used as well.

How to obtain EU publications

Our priced publications are available from EU Bookshop (http://bookshop.europa.eu), where you can place an order with the sales agent of your choice.

The Publications Office has a worldwide network of sales agents. You can obtain their contact details by sending a fax to (352) 29 29-42758.

The mission of the JRC is to provide customer-driven scientific and technical support for the conception, development, implementation and monitoring of EU policies. As a service of the European Commission, the JRC functions as a reference centre of science and technology for the Union. Close to the policy-making process, it serves the common interest of the Member States, while being independent of special interests, whether private or national.